Photoproduction of Scalar Mesons Using the CEBAF Large Acceptance Spectrometer (CLAS)

A dissertation presented to

the faculty of

the College of Arts and Sciences of Ohio University

In partial fulfillment

of the requirements of the degree

Doctor of Philosophy

Shloka K. Chandavar

August 2015

This dissertation titled

Photoproduction of Scalar Mesons Using the CEBAF Large Acceptance Spectrometer (CLAS)

by

SHLOKA K. CHANDAVAR

has been approved for

the Physics and Astronomy Department

and the College of Arts and Sciences by

Kenneth Hicks

Professor of Physics

Robert Frank

Dean of the College of Arts and Sciences

ABSTRACT

CHANDAVAR, SHLOKA K., Ph.D., August 2015, Physics

Photoproduction of Scalar Mesons Using the CEBAF Large Acceptance Spectrometer (CLAS) (166 pp.)

Director of Dissertation: Kenneth Hicks

The search for glueballs has been ongoing for several decades. The lightest glueball has been predicted by quenched lattice QCD to have mass in the range of $1.0-1.7$ GeV and $J^{PC}=0^{++}$. The mixing of glueball states with neighbouring meson states complicates their identification and hence several experiments have been carried out over the years to study the glueball candidates. By analyzing the decay channels and production mechanisms of these candidates, their glueball content can theoretically be determined. In reality, a lot of confusion still exists about the status of these glueball candidates.

The $f_0(1500)$ is one of several contenders for the lightest glueball, which has been extensively studied in several different kinds of experiments. However, there exists no photoproduction data on this particle. In the analysis presented in this dissertation, the presence of the $f_0(1500)$ in the $K^0_S K^0_S$ channel is investigated in photoproduction using the CEBAF Large Acceptance Spectrometer (CLAS) at the Thomas Jefferson National Accelerator Facility, also called Jefferson Lab (JLab). This is done by studying the reaction, $\gamma p \to f_J p \to K^0_S K^0_S p \to 2(\pi^+\pi^-)p$ using data from the g12 experiment. A clear peak is seen at 1500 MeV in the background subtracted data. This is enhanced if the momentum transfer is restricted to be less than 1 GeV^2. Comparing with simulations, it is seen that this peak is associated with t channel production mechanism. The $f_2'(1525)$ has a mass of 1525 MeV and a width of 73 MeV, and hence there is a possibility of it contributing to the peak observed in our data. A moments analysis seems to suggest some presence of a D wave, however, the low acceptance at forward and backward angles prohibits a definitive conclusion.

To my parents, Krishna and Sheetala Chandavar

ACKNOWLEDGMENTS

I have had the good fortune of always being surrounded by beautiful people.

My advisor, Dr. Ken Hicks has been the most wonderful mentor that I could have had. Though I gave him enough reasons to, he never once lost his temper or his patience. He supported me at all times, even when I was at my most inconsistent. He is a great teacher and he pushed me to ask more questions, to not be afraid to talk to the experts and to not shy away from asking for help. However busy he is, he always makes time for his students, and I was regularly impressed by the amount of effort he puts in to ensure our success. His ability to see the best in any situation and in a person, is what has got me this far. Words are quite small things, really, to be able to convey my respect, admiration and gratitude towards him. Thank you, Dr. Hicks. I can never forget your kindness towards me.

I spent only two years of my grad school life in Athens, but the friendships I made there afforded me memories for a lifetime. I remember the many long days and nights in the first year of grad school, of poring over book after book and trying to finish up homework and TA duties. That first year would have been ten-fold more difficult without my batch mates who made everything fun. We spent countless hours together, doing homework, discussing physics, and just hanging out. Thank you Ramana Thota, Youngshin Byun, Yinyun Li, Mahmoud Asmar, Norman Palma, Yuting Li, Meng Shi, Zhiyuan Fan, Heath Kersell, Nowo Riveli, Anthony Ramirez, Dilupama Divaratne, Parisa Roustazadeh, Harsha Attanayake, Nicole Free, John Scheibe. I had such a great time!

Ramana deserves a special mention. We worked together, hung out together, talked for hours on end. He was one of the reasons I had such happy two years in Athens. I called upon him whenever I was in need, and, without giving it a second thought, he was always there. Thank you, Ramana, for having been my ‘true friend’.

Thank you to the seniors in the physics department at OU, who were so welcoming

and helpful: Divya Swaminathan, Manasvita Joshi, Swati Ramanathan, Abhijit Chinchore, Binay Prasai, Tejinder Kaur, Greg Peterson.

I would also like to thank the exceptional professors at OU, who gave a different dimension to learning. Thank you Dr. Madappa Prakash, Dr. Carl Brune and Dr. Shamila Jayasuriya for agreeing to be a part of my dissertation committee.

Thank you Sushmita Gopu for the multitude of times when I've been angry or frustrated and ranted to you. Or the same (or more) number of times when I called you to just be silly. Being friends with you is so easy, so comfortable, so effortless. You get me.

Thank you Amritha Kalyani for being such a great roommate and friend and making 624 CH a home.

Dustin Keller taught me the basics of all things C(LAS). When I was a novice and knew nothing about the CLAS software or how things worked at JLab, he played a significant part in getting me started. His expertise with computing and his doggedness in solving a problem came to my rescue innumerable times. I must have gone to his office and bugged him about this and that problem only about ten thousand times. Thank you, Dustin for your contribution to my knowledge bank and to my dissertation.

The foundation for all the physics that I have been able to work on has been laid by many many people in the CLAS collaboration. It would be impossible to list all of them, but I am very thankful for their invention of the wheel, so to speak. I would like to particularly thank Dr. Dennis Weygand for the several discussions about partial wave analysis, and for the huge amount of time and effort he put into my project. I would like to extend my sincere thanks to Dr. Stepan Stepanyan, Dr. Carlos Salgado, and Dr. Eugene Pasyuk, who patiently listened to and answered my queries. While working on PCAL I learnt a lot about hardware from Hakob Voskanyan and Gegham Asryan, and had a good time with fellow workmates Aji Daniel, Wei Tang, Yeranuhi Ghandilyan and Ani Simonyan. I would also like to thank my colleagues, Johann Goetz, Diane Schott, Michael Kunkel,

Craig Bookwalter, Mukesh Saini, Michael Paolone for the tremendous work they put into the g12 experiment, especially Johann and Diane for putting up with my ever growing list of questions.

A huge thank you to my friends here at Newport News who made my stay here so pleasant: Amrendra Narayan, Nuruzzaman, Aji, Leena Daniel, Rakitha Beminiwattha, Budhhini Waidyawansa, Swedhana Vishwanathan, Sainath Babu, Kalyan Allada, Al Amin Kabir and Rosni Islam. Nur was always just a desk away, I only ever had to look over my shoulder if I needed something or wanted to talk, and I always knew I could count on him for anything. Amrendra has this superpower by which he just knows how a person is feeling, even without being in the same vicinity as them or talking to them. Though I have taken him for granted several times, he was there for me unconditionally and I will always remember that.

Thank you Sunil Dubey, for pushing me to apply for M.Sc., all those years ago, for all the support that you always extended towards me, and for being such a good friend. You always thought I should be out there, conquering the world or something. I owe a large part of being here to you.

Piary and Ajmal Sobhan are, as my mom calls them, my foster parents. They gave me a home and they gave me love, they treated me as their own daughter. They say the world is changing for the worse, they say the world is becoming a darker place. According to me, the world is bright and shining as long as it has people like them.

Thank you Pradeep Cheriyan, for your love, and for the dream of something beautiful. You have changed my life in more ways than you know.

Thanks to my kid brother, Pranav Chandavar, who is not a kid anymore and has grown up to be quite the cool guy. He has graduated from someone I used to fight with all the time, to a friend whom I love to joke around with.

Thank you to my Ayu and Ammama: Muktabai Chandaver and Sudha Upponi. My

beautiful, wonderful, amazing, the most loving, truly kind-hearted grandmothers. I cannot come up with enough superlative adjectives to describe them. They are my role models of how to be as a human being. I am proud to be their granddaughter.

Last, and most important, I want to thank my parents, who made life so easy and made it seem like anything was possible. I often take them for granted, because they are always there, never demanding anything, never forcing anything upon me, always supportive of whatever I do. Without seeming to do anything, they made sure I never had to be anyone other than who I wanted to be. Amma and Pappa, even though I don't say it, I love you both so much and consider myself so lucky to have been born to you.

TABLE OF CONTENTS

Page

LIST OF TABLES

Table Page

LIST OF FIGURES

1 INTRODUCTION

1.1 Discovery of Elementary Particles

The first elementary particle to be discovered was the electron. J.J. Thompson, who discovered it in 1897, tried to explain the electrically neutral atom by proposing a plum pudding model where the electrons are surrounded by a sea of positive charge. However, Rutherford's scattering experiment showed that the positive charge was not spread out throughout the atom, as Thompson had thought, but concentrated at the center, as was most of its mass. The hydrogen nucleus was named proton by Rutherford and it was assumed that the heavier nuclei would be bound states of two or more protons. It was seen, however, that the weights of the next heavier nuclei were not proportional to their charge. The resolution of this problem came with the discovery of the neutron by Chadwick in 1932. It was thus surmised that the atom consists of a heavy core of positively charged protons and negatively charged neutrons with the electrons revolving around this nucleus, much like the planets revolving around the sun.

This brought about the question of how the nucleus stayed together. The repulsion caused by the close confinement of particles of the same electric should rip the nucleus apart. The fact that this did not occur meant that the protons and neutrons were acted upon by a force much stronger than the electromagnetic force. This force was named the strong force. Since this force was not felt in everyday life, it was concluded that its range was extremely short, of the order of the size of the nucleus, ~10^{-15} m (1 fm). Drawing an analogy from electrodynamics, in which the field was known to be propagated by quantized particles called photons, Yukawa proposed that the strong force be mediated by a particle whose mass was almost 300 times that of the electron. It was called the meson to indicate that it was middle weight. (Similarly, electrons were called leptons, meaning light-weight and neutrons and protons were referred to as baryons, meaning heavy-weight.) This meson

was discovered in cosmic rays, and named pion (π). Its charged counterparts, the π^+ and the π^-, were observed in other experiments. Another particle discovered from cosmic rays, the muon (μ), was seen to decay from the pion. Though much heavier than the electron, it was found to have similar properties and hence belonged in the lepton category [116].

Several more particles were discovered: the K, η, ω, the ρ were included in the meson family and the Σ, the Ξ, and the Δ were part of the baryon family. The number of hadrons (baryons and mesons) had grown to such a degree that it was necessary to group them.

In nuclear physics, the proton and neutron are deemed equal in strong interactions because apart from their charge, they have similar properties. They have almost the same mass and strength of interaction and hence they can be treated as projections of the same particle. Borrowing the mathematics of spin, they are assigned a property called isospin, $I = 1/2$. The projection of I along the z-axis, I_Z , is $+\frac{1}{2}$ for the proton and $-\frac{1}{2}$ for the neutron. Many of the newer particles had a puzzling quality: they were produced readily, but had a surprisingly long life time. For example, the Σ^- is readily produced via the strong reaction $\pi^- + p^+ \rightarrow \Sigma^- + K^+$, but its decay into $n + \pi^-$ is weak. This was a contrast to a normal strong decay, *e.g.*, $\Lambda \rightarrow n + \pi$. This was taken to mean that there was another additive quantum number, strangeness, that could be used to define these particles and each hadron was assigned an integer value of strangeness, S [133]. Murray Gell-Mann's Eightfold Way was able to fit the hadrons according to group theory based on their quantum numbers. For example, the lightest mesons, all of which have spin 0 and negative parity, were fit into the pseudoscalar nonet (this is based on SU(3) symmetry) as shown in Figure 1.1 and the lightest baryons with spin $\frac{1}{2}$ and positive parity were fit into an octet (Figure 1.2).

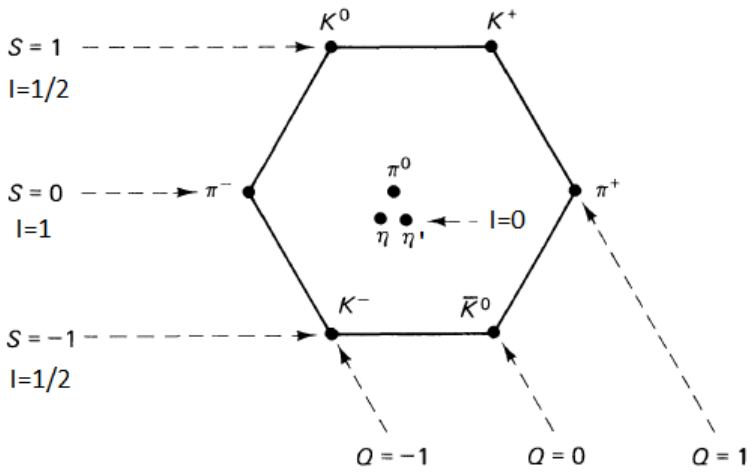

Figure 1.1: The pseudoscalar meson nonet [116]

1.2 Quark Model

The Eightfold way was able to successfully group all the known hadrons. In order to explain this structure, Gell-Mann proposed the quark model in which hadrons are made up of smaller particles called quarks. According to this model, baryons consist of three quarks (qqq) , and mesons are composed of one quark and one antiquark ($q\bar{q}$). There are 6 'flavours' of quarks: up, down, strange, charm, bottom, top (u, d, s, c, b, t). The early nonets and decuplets were based on combinations of the three lightest quarks. On probing the internal structure of hadrons with high energy experiments, it was understood that quarks are fermions, *i.e.*, spin 1/2 particles. The additive quantum numbers of quarks are tabulated in Table 1.1.

The quark model had a couple of dilemmas. Being fermions, quarks should obey Pauli's exclusion principle. However, all 3 quarks in a baryon can have the same flavour and the same spin projection (*e.g.*, in the Δ^{++}), thus seemingly violating this principle. Also, even though the existence of quarks was proved by scattering experiments, no one had been able to observe a quark outside a baryon. To explain the above two situations, it is hypothesized that quarks have a new kind of charge, called colour. There are 3 colours

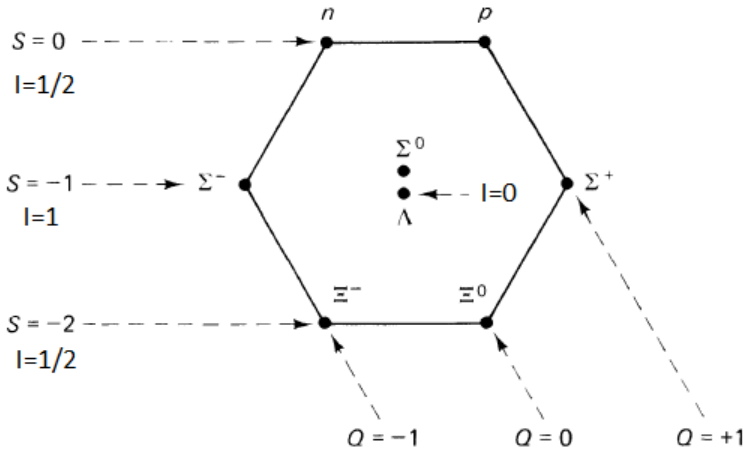

Figure 1.2: The lightest baryon octet [116]

representing this charge: red, green and blue. Anti-quarks, therefore, are anti-red, anti-green or anti-blue. The term colour has nothing to do with actual colour, it is just a label that physicists came up with at the time. The statement of this colour hypothesis is that all naturally-occurring particles should be colourless, or rather, colour singlets, in terms of SU(3) symmetry. That is, a particle should have either a colour and an anti-colour of the same type, ($\mathfrak{b}\bar{\mathfrak{b}}$, $\mathfrak{g}\bar{\mathfrak{g}}$, $\mathfrak{r}\bar{\mathfrak{r}}$); or it should have all three colours in the same amount, *i.e.,* three quarks each with a different colour ($\mathfrak{rgb}$). Using these additional quantum numbers, the theory 'solves' both the exclusion principle quandary and the non-observation of independent quarks.

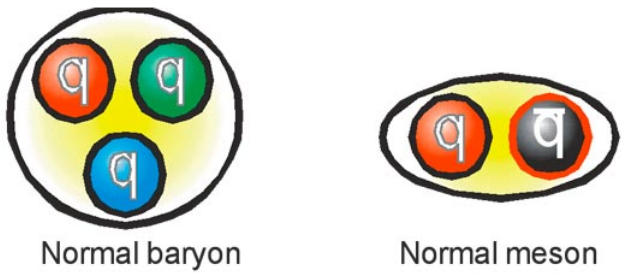

Figure 1.3: Representation of hadrons with coloured quarks [131]

Table 1.1: Additive quantum numbers of quarks [130]

	d	u	s	c	b	t
Q - electric charge	$-1/3$	$+2/3$	$-1/3$	$+2/3$	$-1/3$	$+2/3$
I - isospin	$1/2$	$1/2$	0	0	0	0
I_Z - isospin Z-component	$-1/2$	$+1/2$	0	0	0	0
S - strangeness	0	0	-1	0	0	0
C - charm	0	0	0	$+1$	0	0
B - bottomness	0	0	0	0	-1	0
T - topness	0	0	0	0	0	$+1$

1.3 Meson Nonets

According to the Quark Model, mesons are particles composed of a quark and an anti-quark. Since quarks have spin $1/2$, the intrinsic spin, S, of the quark-antiquark pair can add up to either 0 or 1. The relative orbital angular momentum between them, L, can be any non-negative integer, thus the total spin of the meson is

$$\vec{J} = \vec{L} + \vec{S} \tag{1.1}$$

The Dirac equation specifies that the quark and antiquark should have opposite intrinsic parities and hence the intrinsic parity of a meson is -1. The angular momentum of the pair contributes a factor of $(-1)^L$ due to space inversion $\theta \to \pi - \theta$, $\phi \to \pi + \phi$ in the angular wavefunction [133]. Hence the total parity of the meson is

$$P = (-1)^{L+1} \tag{1.2}$$

C-parity or charge conjugation is a property of neutral mesons that are their own antiparticles, *i.e.,* the π. The interchanging of $q \leftrightarrow \bar{q}$ gives a minus sign, since quarks are

fermions. Furthermore, interchanging the spin projections introduces a factor of $(-1)^{S+1}$ (this is due to spin symmetry), and like before, space inversion gives a factor of $(-1)^L$ [133]. Thus, the C-parity of a meson is given by

$$C = (-1)^{L+S} \tag{1.3}$$

The three lightest quarks, u, d, and s and their respective anti-quarks can form 9 combinations for every allowed J^{PC} value, 8 representing a flavour octet and one, the flavour singlet. This group of 9 combinations is called a flavour nonet. There can be more than one nonet with the same J^{PC} (due to different ways in which the spin and orbital angular momentum can combine to form total spin J), but they normally fall in very different mass ranges. As can be seen from Table 1.2, some J^{PC} values are not present (like 0^{--}, 0^{+-}, 1^{-+} etc.) as they are not allowed by the simple quark model. Mesons with these quantum numbers are called exotic mesons. Experimentally, exotic mesons have not been established.

1.4 Gluons and Glueballs

With the acceptance of the quark model, it was now seen that the pion, originally thought to be the mediator of the strong force was actually just one of the many mesons. The nucleons were no longer the elementary particles, and so, on a fundamental level, the strong force acts on quarks and its mediator is called the gluon. The gluon exists in one of the octet states. The possibility of a colour-singlet gluon (having zero colour charge) would mean that it would be as easily seen as the photon. Also, since as a singlet, it could be directly exchanged between hadrons (which are colour singlets) instead of only quarks, their long-range interaction via the strong force would be possible. Since this is not observed, we must conclude that gluons are confined within hadrons [116].

Table 1.2: The quantum numbers of the meson nonets [130]

L	S	J^{PC}	$I=1$	$I=1/2$	$I=0$	$I=0$
			$u\bar{d}$, $\frac{1}{\sqrt{2}}(d\bar{d}-u\bar{u})$, $\bar{u}d$	$d\bar{s}$, $u\bar{s}$, $s\bar{u}$, $s\bar{d}$	f'	f
0	0	0^{-+}	π	K	$\eta(547)$	$\eta'(958)$
	1	1^{--}	$\rho(770)$	$K^*(892)$	$\phi(1020)$	$\omega(782)$
1	0	1^{+-}	$b_1(1235)$	K_{1B}	h_1	$h_1(1170)$
	1	0^{++}	$a_0(1450)$	$K_0^*(1430)$	$f_0(1710)$	$f_0(1370)$
	1	1^{++}	$a_1(1260)$	K_{1A}	$f_1(1420)$	$f_1(1285)$
	1	2^{++}	$a_2(1320)$	$K_2^*(1430)$	$f_2'(1525)$	$f_2(1270)$
2	0	2^{-+}	$\pi_2(1670)$	$K_2(1770)$	$\eta_2(1870)$	$\eta_2(1645)$
	1	1^{--}	$\rho(1700)$	$K^*(1680)$		$\omega(1650)$
	1	2^{--}		$K_2(1820)$		
	1	3^{--}	$\rho_3(1690)$	$K_3^*(1780)$	$\phi_3(1850)$	$\omega_3(16700$

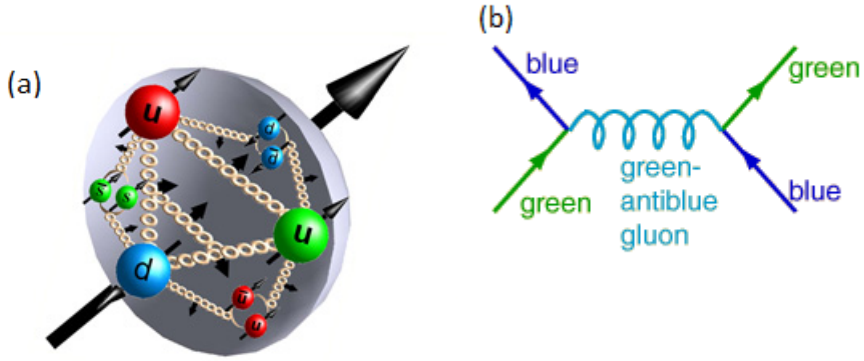

Figure 1.4: (a) Internal structure of a proton [126] : The u and d quarks, each with their own spin are indicated by the arrowheads. Gluons (appearing as “chains") are exchanged between quarks when they exert forces on one another. (b) Gluon-mediated interaction between two quarks [128].

The theory of quantum chromodynamics (QCD) is constructed in analogy with quantum electrodynamics (QED). They have some similarities in that they both act on spin $\frac{1}{2}$ particles and are both mediated by spin 1 gauge bosons. The main difference is that photons do not carry electric charge, whereas gluons carry colour charge. Due to this, they are able to interact with other gluons. Now, in the same way that coloured quarks combine to form colour-singlet hadrons, two or more gluons should be able to combine to form colour-singlet glueballs. Since gluons have spin 1, glueballs should have integer spin, like mesons [132].

Glueball states likely mix with mesons having the same J^{PC} values and this makes the detection of glueballs very complicated. Since glueballs are composed of only gluons, they should be isoscalars ($I = 0$) and flavour-singlets. Thus, the biggest factor in looking for glueballs is finding an extra singlet state near the mass of a known meson nonet [144, 149]. Another factor is decay rate: mesons and glueballs have different decay properties and studying these properties may provide some hint as to the internal structure of this state. One way is calculating the stickiness of the decay. Stickiness is defined as the ratio of the particle width to the two photon width together with a normalization factor. Gluons do not couple to photons since they have no electric charge. The idea of stickiness is that a particle with a high gluon content will have less probability of decaying into a particle with two-photon decays. The higher the stickiness, the higher the gluon content of the original decaying particle [148]. Obviously glueballs should have a high stickiness. Though decay widths have been widely measured, there are still large uncertainties in these measurements. This analysis is rendered very difficult due to the tendency of mixing between glueball and meson states. Glueballs will not be produced in $\gamma\gamma$ fusion reactions due to the zero coupling between photons and gluons. Hence those particles with higher glueball content will have low probability of being produced in these reactions. It is expected that glueballs are flavour blind, *i.e.,* they have equal coupling to mesons of all flavours and, in the case of

the lightest glueball, will have decay amplitude γ^2 according to Table 1.3. The calculation of this amplitude is tabulated in [124]. Hence, measuring various decay branching ratios for candidate glueball states is a leading experimental goal.

Table 1.3: Expected decay amplitudes for a glueball normalized to the rate $\eta\eta'$ [144]

Decay	$\pi\pi$	$K\bar{K}$	$\eta\eta$	$\eta\eta^{'}$	$\eta^{'}\eta^{'}$
γ^2	3	4	1	0	1

Lattice QCD is a non-perturbative means of solving QCD numerically. Approximation techniques known as quenched LQCD calculations are an attempt to reduce the large computational requirement of LQCD [149, 34]. Fig. 1.5 shows recent calculations of the mass spectrum of the glueballs using quenched QCD. From these different calculations, we expect the mass of the scalar meson to lie between about 1 to about 1.7 GeV. The lightest glueball consists of two gluons and has $J^{PC} = 0^{++}$.

1.5 Outline of the thesis:

This thesis mainly focusses on the search for the lightest glueball. Several experiments have been performed by various collaborations with the aim of detecting the $J^{PC} = 0^{++}$ glueball and have yielded confusing results. A brief summary of these experiments and their results is presented in Chapter 2. The data used for our analysis was obtained from the g12 experiment using the CEBAF Large Acceptance Spectrometer (CLAS) at Hall B in Jefferson Lab; an overview of the detector sub-systems of the CLAS detector is given in Chapter 3.

Jefferson Lab, over the last few years, has worked towards an upgade in its electron beam energy from 6 GeV to 12 GeV. Consequently, it was necessary to update the CLAS detector sub-systems to function at this increased energy. In particular, a Preshower

Calorimeter (PCAL) was built to be used in conjunction with the existing electromagnetic calorimeter. Since the author of this thesis spent a significant amount of research time on the assembly and quality control aspects of PCAL, Chapter 4 gives a synopsis about its design and construction, as well as details about the procedures involved in the quality assurance testing of the components of the calorimeter.

Chapters 5 and 6 detail the analysis procedures of the data and simulation. A moments analysis was performed using actual and simulated data, the formalism of which is presented in Chapter 7, and its results in Chapter 8. A discussion of the results will be presented in Chapter 9.

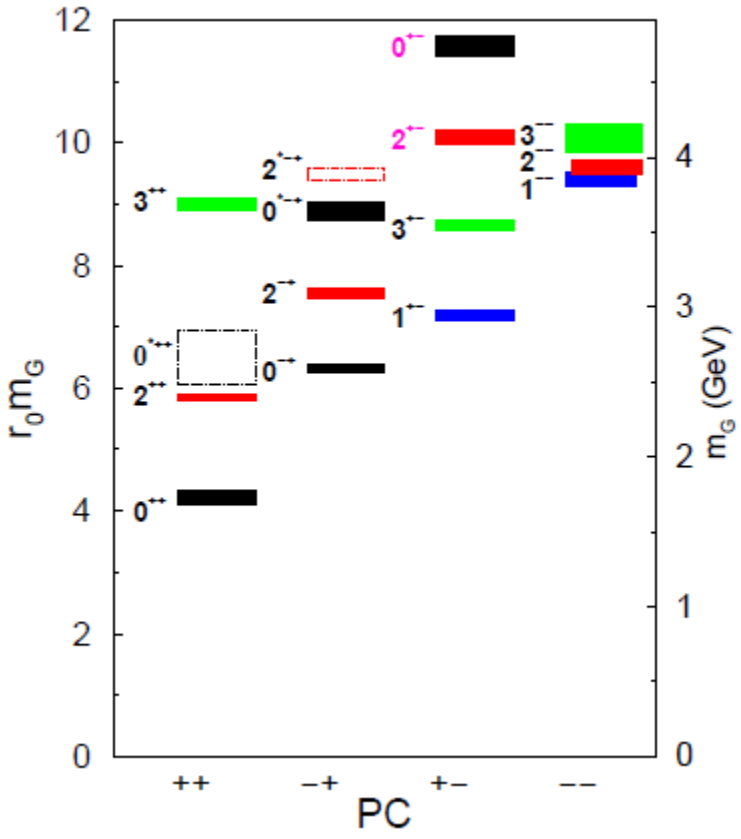

Figure 1.5: Results for the gluonic mass spectrum from quenched LQCD calculations [111].

2 THE SCALAR MESONS

Since the lightest glueball is expected to have $J^{PC} = 0^{++}$, the scalar mesons have been extensively investigated. In spite of this, there is no absolute consensus on the status of several of these scalars. For some, the distinction between resonance and background is difficult because of their large decay widths. The opening of multiple decay channels within short mass intervals can affect the contributions from nearby resonances. The possibility of multi quark and glueball states adds to the speculations. In this chapter, experimental results for scalar mesons will be briefly reviewed as will the interpretations that abound.

Of the scalar mesons, the isoscalars are the mesons of interest in the search for glueballs. Five isoscalar scalars have been identified by experiment: and listed by the Particle Data Group (PDG) : $f_0(500)$, $f_0(980)$, $f_0(1370)$, $f_0(1500)$ and $f_0(1710)$. However, of these, only two can belong to the meson scalar nonet. This excess of scalar states suggests the presence of a glueball, albeit possibly only as a mixture of glueball-meson states.

2.1 Previous Experiments

Over the years, a lot of experiments have focused on the scalar mesons, with confusing results over many years. Some types of processes, so-called, glue rich processes, are deemed to be more conducive to the production of glueballs than others [146, 144]. One of the most promising is radiative decays of quarkonia. Quarkonium is a meson which consists of a quark and its own antiquark, *e.g.,* charmonium $(c\bar{c})$, or J/Ψ, and bottomonium $(b\bar{b})$, or Υ. In particular, the J/Ψ is significant because its mass is below the threshold of the D mesons, composed of charmed quarks, and its decay into lighter mesons is suppressed by the OZI rule (a rule proposed by Okubo, Zweig, and Iizuka to explain the unexpected decay modes of some hadrons). The c and $\bar{c}$ of the J/Ψ can annihilate into a photon and two gluons. These gluons can then interact to form glueballs. Another glue-rich process is central production in which two hadrons pass by each other at high energy with low mo-

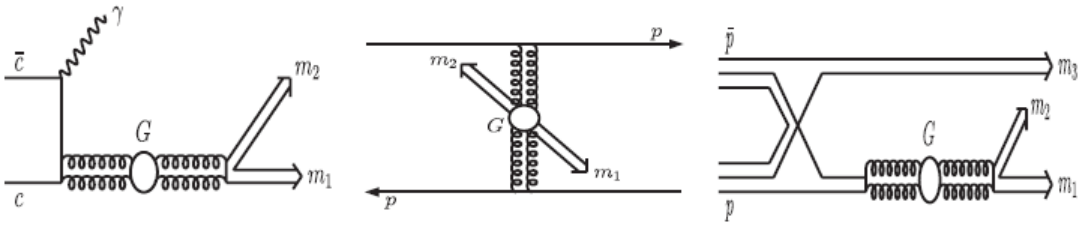

Figure 2.1: Glue-rich processes: Radiative decay of J/Ψ, central production and $p\bar{p}$ annihilation. Image Source: [30]

mentum transfer, facilitating a double Pomeron exchange, and are scattered diffractively in the forward direction. In proton-antiproton annihilation, quark-antiquark pairs annihilate to form gluons, which then may combine to form glueballs. Fig. 2.1 illustrates these processes. Photons, possessing no colour charge, cannot couple to gluons, and hence $\gamma\gamma$ collisions have a very low probability of producing glueballs. A small branching ratio for decay of a meson resonance into $\gamma\gamma$ does not necessarily prove that the said resonance is a glueball because of mixing between states.

Several experiments that have searched for glueball components in scalar meson production are now briefly described, with results given in Section 2.2.

Many central production experiments were carried out at CERN. The WA76 [102] and WA91 [103] experiments made use of the Ω spectrometer to study meson resonances by directing hadron beams toward an H_2 target . The WA102 collaboration combined the efforts of the WA76 and the GAMS experiments, which had run at the Institute for High Energy Physics (IHEP) at Protvino. The setup for the WA102 experiments included the Ω spectrometer and the GAMS-4000 detector. This expanded the scope of both these experiments and made possible the study of a larger mass range of both charged and neutral particles. The results from WA102 will be discussed in Section 2.2.

The LEAR (Low Energy Antiproton Ring) at CERN facilitated numerous $p\bar{p}$ annihilation experiments. The Asterix experiment [94] stopped antiproton beams using a gaseous H_2 target at normal temperature and pressure, whereas the Crystal Barrel experi-

ment [95] studied $\bar{p}$ beams on a liquid hydrogen target. The Obelix experiment [96] was capable of using liquid and gaseous hydrogen targets at differing temperatures and pressures, thus providing a wide range of target densities for studying meson spectroscopy.

Radiative decays of quarkonia are studied in e^+e^- collision experiments. Several experiments using the the BES (Beijing Spectrometer), and the upgraded BES-II and BES-III detectors at the BEPC (Beijing Electron Positron Collider) [97] have been performed to study the radiative decay of the J/Ψ meson. The maximum beam energy was $2E = 4.4$GeV for the BEPC and $2E = 5.0$GeV for the BEPC-II. The CLEO (as well as the upgraded CLEO-c) and CLEO-III detectors [98] at the Cornell Electron-positron Storage Ring (CESR) also investigated the radiative decays of J/Ψ and Υ in e^+e^- interactions near 10 GeV . The KLOE (K LOng Experiment) collaboration at the electron positron collider of DAΦNE (Double Annular Φ Factory for Nice Experiments) in Italy examined the radiative decays of $\phi(1020)$ to $f_0(980)$ [104] and $a_0(980)$, with $2E \backsim 1.02$GeV.

The Large Electron-Positron (LEP) collider at CERN, though mainly constructed for investigating electro-weak physics, was used by the 4-π ALEPH (Apparatus for LEP PHysics) detector [99] and the L3 detector [100] collaborations to publish several results on two-photon widths of glueball candidates.

2.2 Previous Experimental Results and Theoretical Interpretations

The properties of the scalar mesons from various experiments are constantly reviewed by the Particle Data Group (PDG) and the listings from the 2014 version are tabulated in Table 2.1 .

The $f_0(500)$, also called σ, has had a long history, and was previously called $f_0(600)$; it has a very large width: 400-500 MeV making it difficult to model using naive methods. Detailed discussion about the experiments and calculations involving the $f_0(500)$ can be found in reference [51].

Table 2.1: I=0, $J^{PC} = 0^{++}$mesons listed by the Particle Data Group [50]

Name	Mass (MeV/c^2)	Width (MeV/c^2)	Decays
$f_0(500)$ (σ)	$400-500$	$400-700$	$\pi\pi, \gamma\gamma$
$f_0(980)$	990 ± 20	$40-100$	$\pi\pi, K\bar{K}, \gamma\gamma$
$f_0(1370)$	1200 to 1500	$200-500$	$\pi\pi, 4\pi^0, 2\pi^+2\pi^-, \pi^+\pi^-2\pi^0, \rho\rho$
			$\pi(1300)\pi, a_1(1260)\pi, \eta\eta, K\bar{K}, \gamma\gamma$
$f_0(1500)$	1505 ± 6	109 ± 7	$\pi^+\pi^-, 2\pi^0, 4\pi^0, 2\pi^+2\pi^-, \rho\rho$
			$\pi(1300)\pi, a_1(1260)\pi, \eta\eta, \eta\eta', K\bar{K}$
$f_0(1710)$	1720 ± 6	135 ± 8	$K\bar{K}, \eta\eta', \pi\pi, \omega\omega$

The J/Ψ decays are useful for flavour tagging of the unknown resonance, since radiative decays do not affect the flavour structure. For example, if the J/Ψ decays into the $\phi(1020)$, ideally an $s\bar{s}$ structure, and a resonance X, then we can deduce that X also has a much larger $s\bar{s}$ content than $n\bar{n}$, where $n\bar{n}$ is defined by Eq. 2.1.

$$n\bar{n} = \frac{1}{\sqrt{2}}(u\bar{u} + d\bar{d}) \tag{2.1}$$

Based on the presence of the $f_0(980)$ in $J/\Psi \to \phi\pi^+\pi^-$ [64] and its near absence in $J/\Psi \to \omega\pi^+\pi^-$ [63] (refer to Fig. 2.2(a), (c)) indicate a large $s\bar{s}$ component. Radiative decays of the $\phi(1020)$ into $a_0(980)$ and $f_0(980)$ by the SND [58, 59], CMD2 [60] and KLOE [61] suggest the presence of kaon loops within the $a_0(980)$ and $f_0(980)$. This favours the interpretation of a four-quark or molecular $K\bar{K}$ structure. There is no definitive agreement in the understanding of its structure using two-photon width results. It is likely that the $f_0(980)$ and the $a_0(980)$, along with the $f_0(500)$ and $K_0^*(800)$ form a low-mass nonet of primarily four-quark states [66]. Linear and non-linear sigma approaches in chiral perturbation theory, as well as several mixing models infer that there is strong possibility

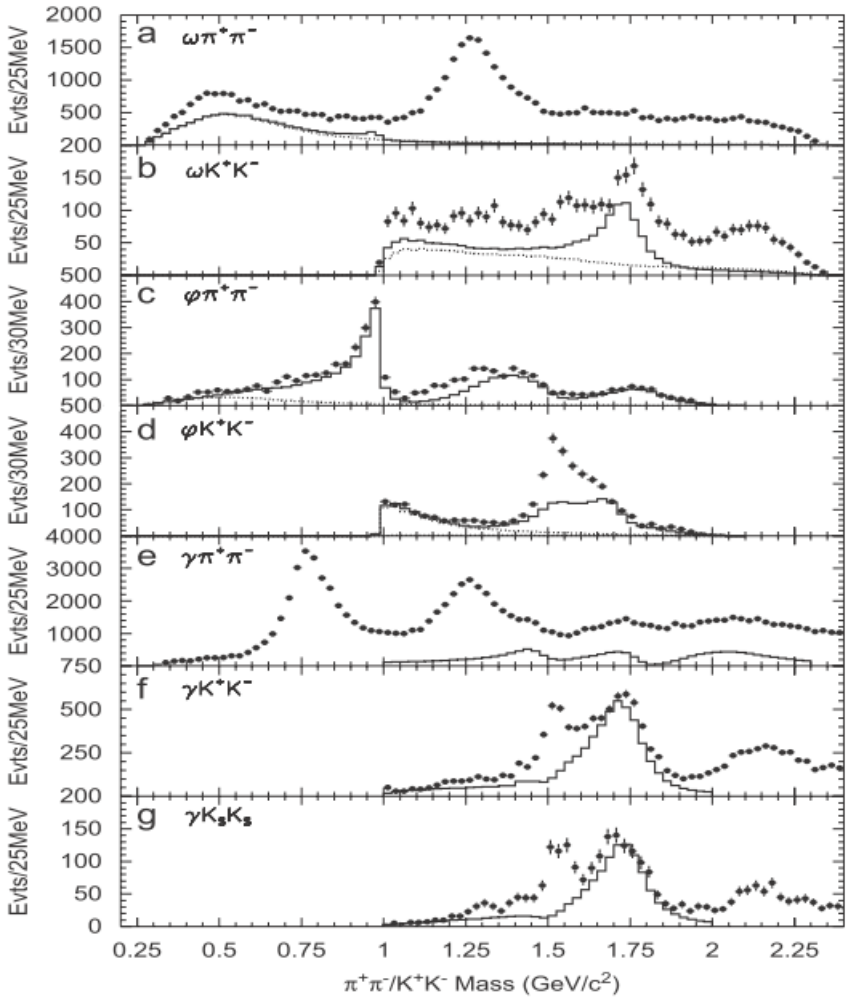

Figure 2.2: The invariant mass distributions of the pseudoscalar meson pairs recoiling against ω, ϕ, J/Ψ decays measured at BESII. The dots with error bars are data,the solid histograms are the scalar contribution from PWA, and the dashed lines in (a) through (c) are contributions of $\sigma(485)$ from the fits,while the dashed line in (d) is the $f_0(980)$. Image Source: [69]

of the $f_0(980)$ being a $K\bar{K}$ molecule, though the structure of the $a_0(980)$ is still unclear (see, for example, [67]). The $f_0(500)$, though possessing a strong non-$q\bar{q}$ structure, has a secondary $q\bar{q}$ structure around 1 GeV. The models based on unitary quarks with coupled $q\bar{q}$ and meson-meson channels interpret the scalars as two nonets, the $\{f_0(980), a_0(980), f_0(500)$ and $K_0^*(800)\}$, and the $\{f_0(1370), f_0(1500)/f_0(1710), a_0(1450)$ and $K_0^*(1430)\}$,

which are two expressions of the same bare states [68], where the former nonet appears consistent with a dominant $qq\bar{q}\bar{q}$ component [46]. A much detailed exposition about the various interpretations can be found in references [51, 144, 146].

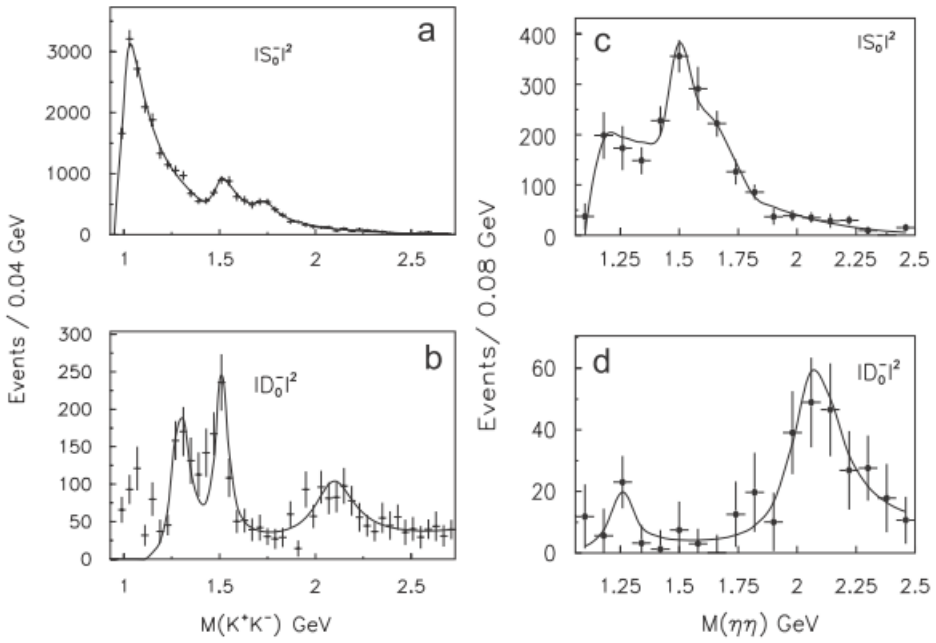

Figure 2.3: K^+K^- S wave (a) and D wave (b) from a coupled channel analysis of WA102 $\pi^+\pi^-$ and K^+K^- data. [42]

There is a significant production of $f_0(1500)$ and $f_0(1710)$ in the radiative decay of J/Ψ to $2\pi^+2\pi^-$ [76]. Results from partial wave analyses of data from the BES experiment are summarized in Fig. 2.2. The radiative decays into $K\bar{K}$ [72, 74](Fig. 2.2 (f), (g)) show that the $f_0(1710)$ favours these channels, though there is not much contribution from the $f_0(1500)$, the resonance around 1500 MeV being the $f_2^{'}(1525)$. Flavour tagging in the vector meson decays (Fig. 2.2 (a),(b),(c),(d)) yields confusing results for the $f_0(1710)$: A peak at 1710 MeV in decays to ωK^+K^- [71] , but none in ϕK^+K^-[64] would suggest an $n\bar{n}$ structure for the $f_0(1710)$. However a similar spectrum for $\phi\pi^+\pi^-$ [64] shows a mild resonant structure at ~1790, but no corresponding peak in $\omega\pi^+\pi^-$decays [63]. The BES collaboration suggested that there may be two possible resonances in the 1700-1800 range.

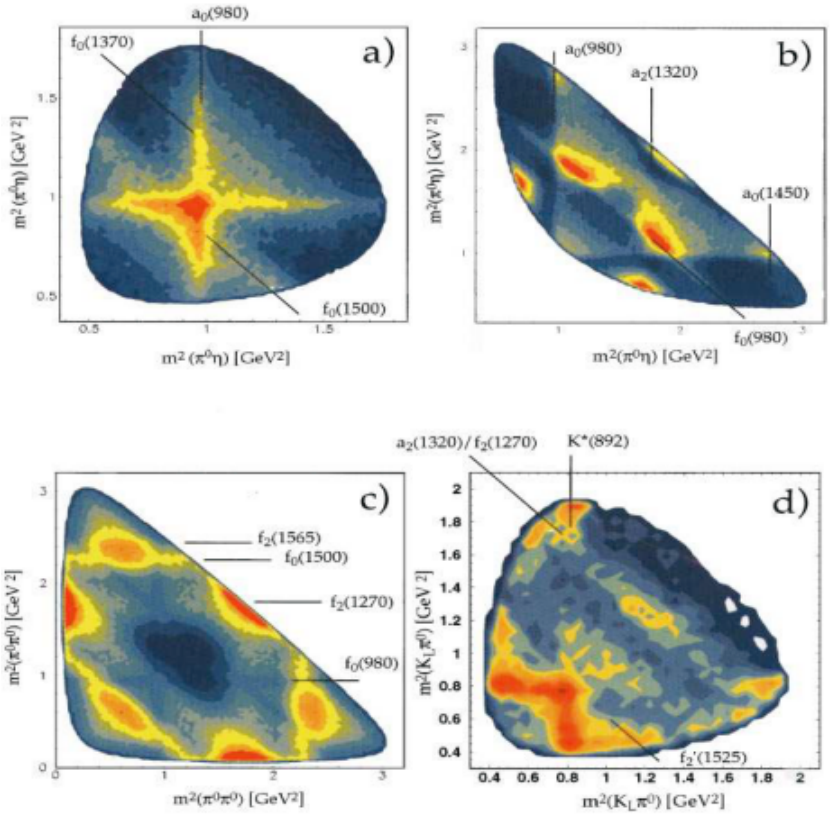

Figure 2.4: Dalitz plots for $p\bar{p}$ annihilation at rest from Crystal Barrel into (a) $\pi^0\eta\eta$ and (b) $3\pi^0$. Image Source: [57]

PWA analyses of central production data from the WA102 experiment [84]-[92] show a strong $f_0(1500)$ signal and a weaker $f_0(1710)$ presence, see Fig. 2.3. The large branching $K\bar{K}$ to $\pi\pi$ ratio of the $f_0(1710)$ indicates an $s\bar{s}$ structure. The same branching ratio for the $f_0(1500)$ is quite small, hence if it is a $q\bar{q}$ state, then it has to have a large $n\bar{n}$ component. The cross sections for the $f_0(980)$, $f_0(1500)$ and $f_0(1710)$ are independent of energy and hence are consistent with double - Pomeron exchange being involved in their production.

Various decay channels were studied using $p\bar{p}$ annihilation experiments from Crystal Barrel [77, 78, 79, 80, 81]. Dalitz plots of these analyses are shown in Fig. 2.4. The $f_0(1500)$ is found to decay to 4π nearly half of the time, and the $f_0(1370)$ is also most likely to decay to 4π. The contribution of these two scalars in the strange sector was very

small. These two results point to an $n\bar{n}$ structure rather than $s\bar{s}$. There was no observed signal for the $f_0(1710)$ in any of the analyses. The Obelix data finds a broad $f_0(1370)$ and a relatively narrow $f_0(1500)$, but no $f_0(1710)$[82, 83]; however the values for the branching ratios do not match those from Crystal Barrel.

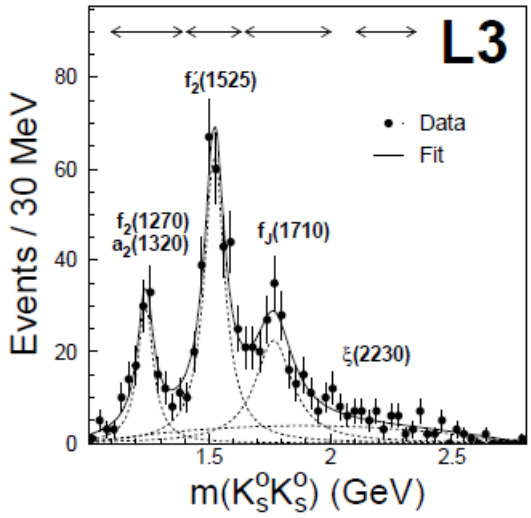

Figure 2.5: Invariant $K_S^0 K_S^0$ mass in $\gamma\gamma$ collisions from L3. The solid line corresponds to a maximum-likelihood fit. The arrows represent the $f_2(1270)/a_2(1320)$, the $f_2'(1525)$, the $f_J(1710)$, and the $\xi(2230)$ mass regions. Image Source: [43]

The L3 experiment at the LEP facility used data from $\gamma\gamma$ fusion to look for scalar mesons [43] The presence of a scalar meson in such an experiment highly reduces the chances of it having a large glueball content. Fitting to the data shows no presence of the $f_0(1500)$. A signal is observed around 1700 MeV, denoted by $f_J(1710)$ in Fig. 2.5, where J stands for the undetermined spin of the resonance. The ALEPH $\gamma\gamma$ fusion experiment at the same facility showed no presence of $f_0(1500)$ or $f_J(1710)$ in the decay to $\pi^+\pi^-$. If the $f_0(1700)$ is a $q\bar{q}$ structure, and if it is the resonance $f_J(1710)$ observed in L3, then it is consistent with the results of the previous experiments which show a large branching ratio to strange pseudoscalars. The $f_0(1500)$, which is known to mostly decay into pions is absent from the ALEPH data; this could imply it possesses a non $q\bar{q}$ structure.

The ZEUS collaboration observed the $f_0(1710)$ in the mass spectrum of $K_S^0 K_S^0$ in ep collisions (Fig. 2.6). They reported a much better signal for $f_0(1710)$ than observed in previous experiments [35].

There is no clear conclusion that can be drawn from the above experiments. The naive quark model would lead us to believe that the $f_0(1370)$, $a_0(1450)$, $K_0^*(1430)$, and $f_0(1710)$ form a nonet, the $f_0(1370)$ being the $n\bar{n}$ state, and the $f_0(1710)$, the $s\bar{s}$ state [70]. The narrow relative width of the $f_0(1500)$, its heightened production in central production favouring double Pomeron exchange, as well as its absence in the $\gamma\gamma$ fusion experiments suggest that it is mainly glue. However, it has been proposed that chiral suppression could cause the glueball to favourably decay to strange mesons [33]. This would favour the interpretation of the $f_0(1710)$ as being a closer glueball match.

Several mixing scenarios have been suggested after taking into account above experimental results. Representing the $f_0(1370)$, the $f_0(1500)$ and the $f_0(1710)$ by $|f_i\rangle$, where $i = 1,2,3$ and the states of pure $n\bar{n}$, pure $s\bar{s}$ and pure glue by $|n\bar{n}\rangle$, $|s\bar{s}\rangle$, and $|G\rangle$ respectively, the mixing between states can be represented by a matrix as shown in Eq. 2.2. The proposed mixing is generally model dependent and can be broadly divided into two groups based on whether the bare glueball is heavier or lighter than the pure $s\bar{s}$ state.

$$\begin{pmatrix} |f_1\rangle \\ |f_2\rangle \\ |f_3\rangle \end{pmatrix} = \begin{pmatrix} M_{1n} & M_{1s} & M_{1g} \\ M_{2n} & M_{2s} & M_{2g} \\ M_{3n} & M_{3s} & M_{3g} \end{pmatrix} \cdot \begin{pmatrix} |n\bar{n}\rangle \\ |s\bar{s}\rangle \\ |G\rangle \end{pmatrix} \tag{2.2}$$

For the case where the bare glueball is lighter than the $s\bar{s}$ state: Close and Amsler based their calculations mostly on results from the Crystal Barrel experiment and had slightly different mixing for cases in which the glueball could decay directly [52, 53] and when it could not [54]. F. Giacosa *et al.* did their calculations [55] based on a chiral

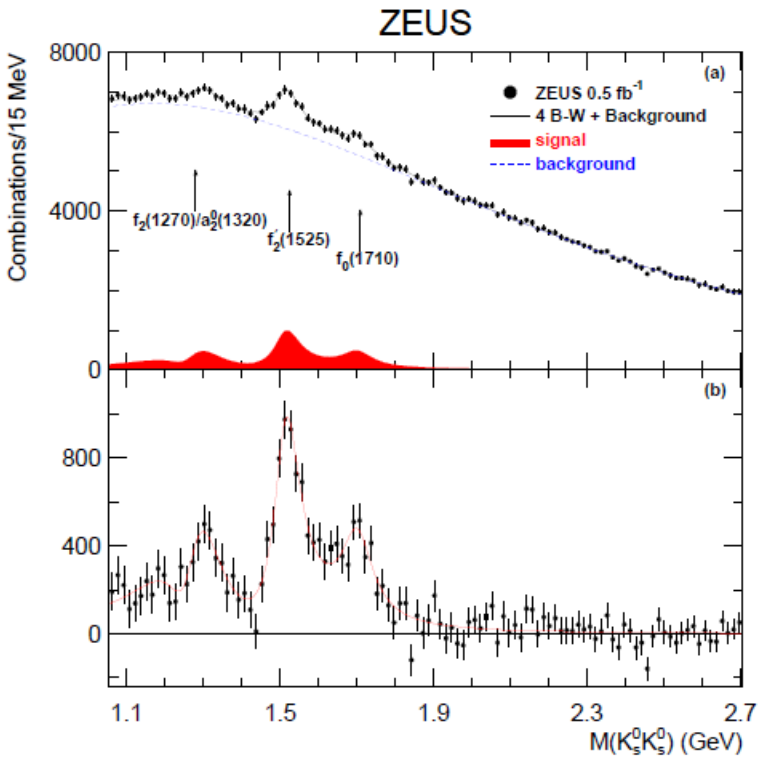

Figure 2.6: (a) The measured $K_S^0 K_S^0$ invariant-mass spectrum (points) from ZEUS. The solid line is the result of the fit and the dashed line represents the background function. (b) Background-subtracted $K_S^0 K_S^0$ invariant-mass spectrum (dots); the result of the fit is shown as a solid line [35].

approach. Flavour blindness was assumed for all these computations. In all of these calculations, the $f_0(1500)$ has the largest glue component and the $f_0(1370)$ is the most likely singlet state.

For the case where the bare glueball is heavier than the $s\bar{s}$ state : In their model, Weingarten and Lee made the assumption that the glueball decays more often into strange mesons than lighter ones [40]. F. Giacosa *et al.* [55] had two sets of calculations, as before, depending on whether or not a direct decay of the glueball was involved. Cheng *et al.* [56] set the starting mass of the glueball using lattice calculations. For all these calculations, the $f_0(1710)$ had the most glueball content and the $f_0(1500)$ was more likely to be the octet state.

2.3 Photoproduction

Photoproduction has been suggested as a means to look for glueballs [29]. It can occur via two channels, as shown in Figure 2.7.

In the glue rich s-channel, the photon and proton interact to form an intermediate particle which then undergoes decay. In the t-channel on the other hand, the large photon coupling with the outgoing particle makes it less likely that this process will produce a glueball. At high energies, the t-channel dominates, but near threshold energy (of production of f-meson/glueball), there are many s-channel resonances.

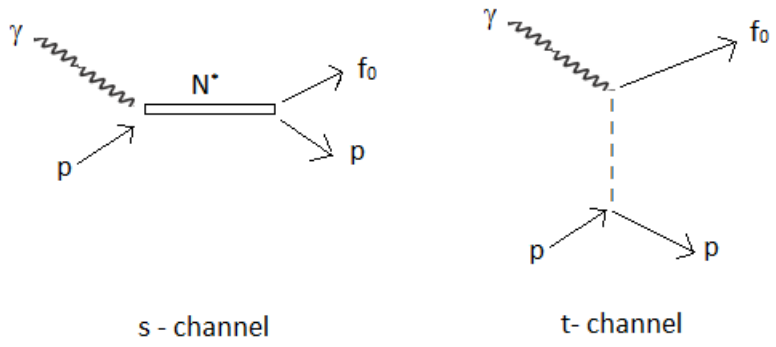

Figure 2.7: s and t channel for photoproduction

The analysis for this thesis examines the photoproduction spectrum of scalar mesons at energies $\sqrt{s} = 2.43$ GeV to $\sqrt{s} = 3.4$ GeV, the details of which will be given in the next few chapters.

3 EXPERIMENTAL SETUP

The data for this analysis was taken from the g12 experiment carried out in Hall B at Thomas Jefferson National Laboratory (TJNAF), also called Jefferson Lab or JLab, located in Newport News, Virginia. JLab has a Continuous Electron Beam Accelerator Facility (CEBAF) which, until 2012 was capable of providing a continuous electron beam of up to 6 GeV to three halls A, B and C. An upgrade is under way to double the maximum energy of the electron beam from 6 GeV to 12 GeV. This chapter will detail the various elements of the accelerator and the detector that were in use at the time of the g12 experiment. The CLAS (CEBAF Large Acceptance Spectrometer) detector in Hall B is designed for high efficiency in detecting multi-particle final states and for experiments with low luminosity.

The g12 data were taken with a 5.71 GeV electron beam delivered by CEBAF to Hall B, which was then converted to a bremsstrahlung photon beam and made incident on a proton target. The experiment was based on three CLAS proposals : 04-005 [12], 04-017 [13] and 08-003 [14]. The first, *Search for New Forms of Hadronic Matter in Photoproduction,* also called HyCLAS, would focus on meson spectroscopy. It required a large acceptance for multi particle meson states. Simulations showed that the the best placement of the target would be upstream from the center of CLAS. The second proposal, *Study of Pentaquark States in Photoproduction Off Protons,* also called Super-G, would study the baryon Ξ spectrum in addition to searching for the so-called pentaquark states. This required a higher energy beam, with the other requirements being similar to the HyCLAS proposal. The third proposal, *The $\gamma p \to \pi^+ n$ Single Charged Pion Photoproduction* required a single track trigger and lower current. These special requirements were added on to specific 'runs' and the data was included in the g12 data set. Cerenkov detectors were turned on after two weeks of starting the experiment, which enabled the distinction between pions and electrons. This resulted in the g12 data set including leptonic physics as well.

3.1 CEBAF, The Continuous Electron Beam Accelerator Facility

CEBAF, designed to study the electromagnetic structure of hadrons, was able to simultaneously deliver high power electron beams of up to 200μA with 75% polarization to halls A, B, and C until 2012. The maximum energy of the electron beam was 6 GeV. One major advancement was the employment of superconducting radio frequency (RF) cavities to provide the acceleration gradient. Previously, copper cavities were used for the acceleration gradient, but resistive heating resulted in low duty cycles. The non-resistive superconducting RF cavities had a 100% duty cycle and were cheaper to operate. This ensured a continuous high-quality electron beam, enabling high-statistics data collection even at low currents. Another innovation is beam recirculation which minimizes cost and which has large enough bend radii to accommodate energy upgrades [15].

Figure 3.1 shows the aerial view of the lab. The accelerator ring lies beneath racetrack-like area and the three grassy ring structures at the bottom of the picture are the three halls. Hall B is the smallest of the three and is situated in the middle.

The electron beam is produced using a three-laser photocathode system in which three independent lasers are directed at a GaAs photocathode. This gives each hall the ability to control its own beam current and polarization. Each laser is operated at a frequency of 499 MHz and the three lasers differ in phase by 120°. The three beams together produce a 'bunch-train' of frequency of 1497 MHz which is boosted by the injector system to 67 MeV. The beam, before entering the main accelerator is grouped into bunches of 2 ps separated by 667 ps; each bunch has its own properties which are repeated every third bunch.

The main accelerator system consists of two linear accelerators (linacs), each 1.4 km in length and containing 20 cryomodules. Each cryomodule contains eight superconducting niobium cavities (Figure 3.3) which are kept at 2 Kelvin by the Central Helium Liquifier (CHL). Standing radio frequency waves are induced in the cavities, as shown in

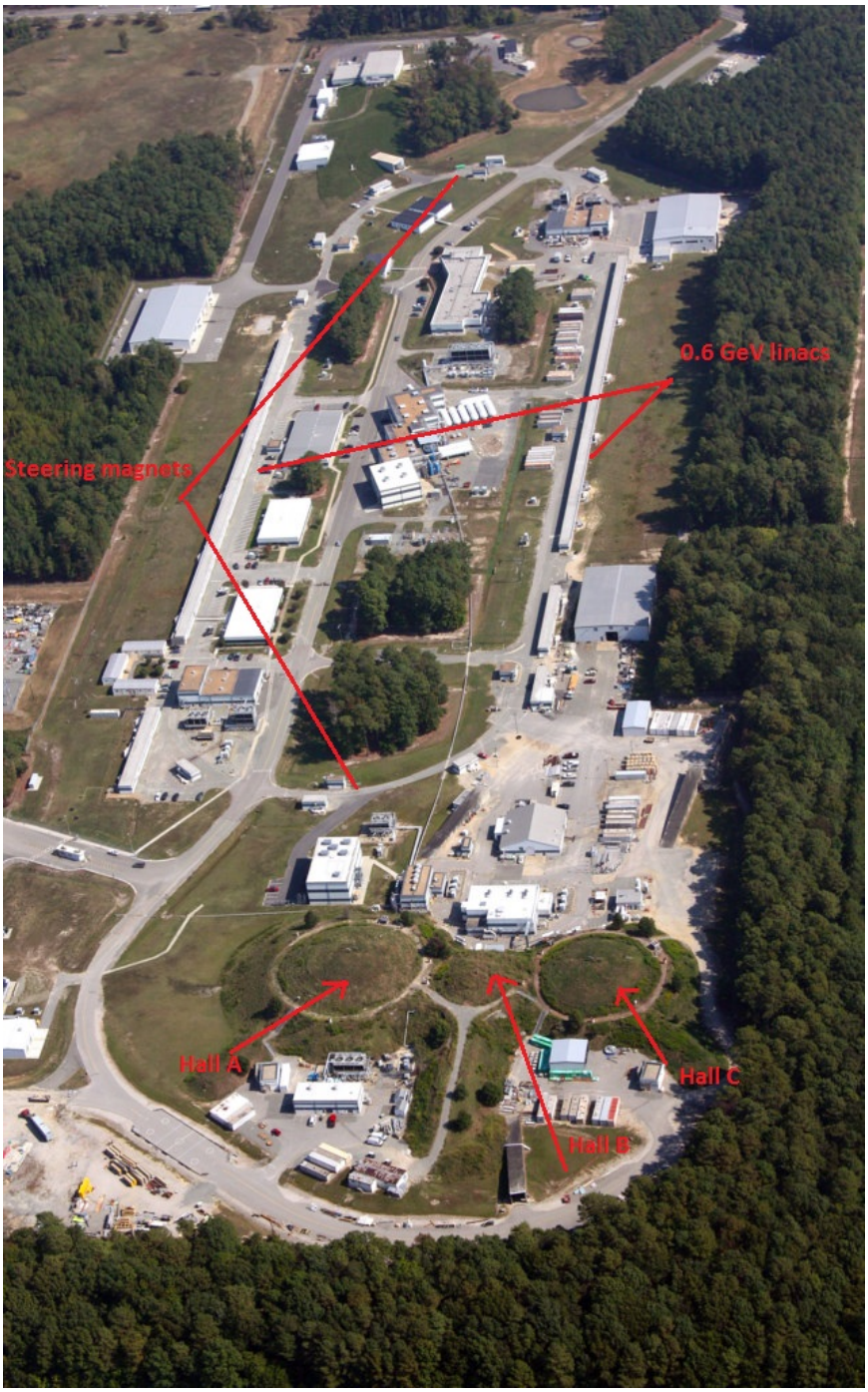

Figure 3.1: Aerial View of CEBAF at Jefferson Lab[17].

Figure 3.4 , and this provides the acceleration gradient to the electrons passing through. The linacs are connected by nine recirculation arcs with radii of 80 meters, refer to Figure 3.2. The beam can be passed unto 5 times through each linac, the electrons accelerating about 600 MeV at every pass through a linac. One whole pass would thus accelerate the beam by ~1.2 GeV.

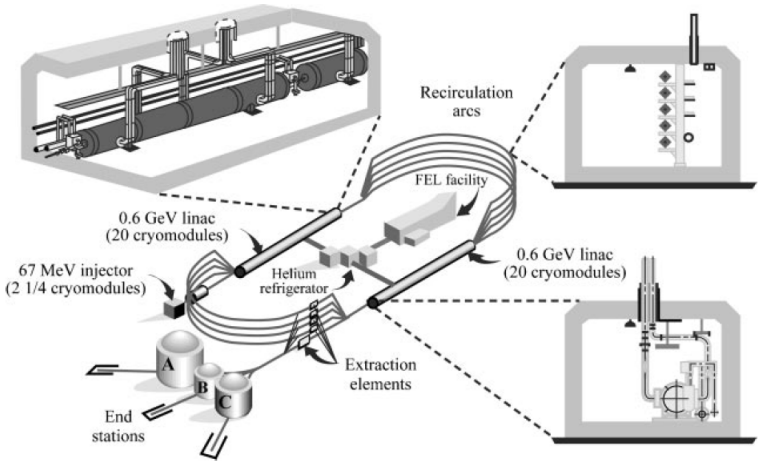

Figure 3.2: Schematic picture of CEBAF at JLab depicting the layout of the facility and the cross-sections of the linear accelerator (LINAC) and recirculation arcs [15].

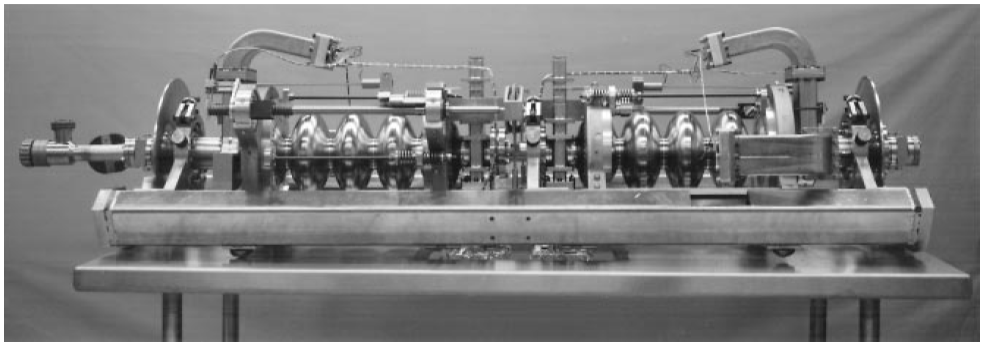

Figure 3.3: Photograph of superconducting niobium RF cavity pair. Each five-cell cavity is 0.5 m long [15].

The beam is extracted into each hall using RF separator cavities. Since the beam bunches are separated by 120°, each hall can control the type of beam that is required by

its experiment; a beam bucket is delivered to the hall every 2 ns. A detailed exposition on the historical development of CEBAF as well its construction and engineering is given in Ref. [15].

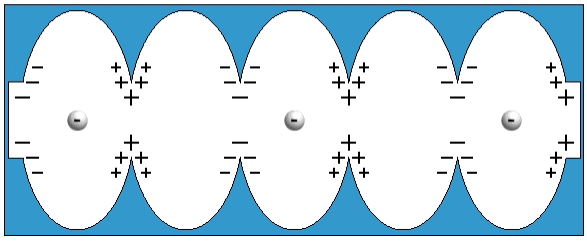

Figure 3.4: Diagram depicting an RF cavity. Standing waves are established across the cavity which lead to a continuous acceleration felt by the electron passing through the cavity [25].

3.2 The Photon Tagger

The photon beam for photoproduction experiments is produced from the electron beam by bremsstrahlung. The electrons are passed through a thin radiator, usually gold, with thickness ranging from 10^{-6} to 10^{-4} radiation lengths. The electrons, while passing through the radiator are decelerated because of the electromagnetic field of the radiator nuclei and emit energy in the form a photon. The energy transferred to the nucleus being extremely small, we can write

$$E_\gamma = E_0 - E_e \tag{3.1}$$

where E_γ is the energy of the emitted photon, E_0 is the original electron energy and E_e is the emitted electron energy. The degraded electrons are then defected by a magnet into a scintillator hodoscope which can measure its energy. Thus, knowing E_0 and E_e, the radiated photon can be tagged with the resulting energy.

For high energy electrons, the direction of the radiated photon and the decelerated electron is almost along the direction of the initial electron beam. Collimators are used to align the photon beam and sweep magnets get rid of any charged particles that are generated in the collimator. Figure 3.5 depicts the tagger system.

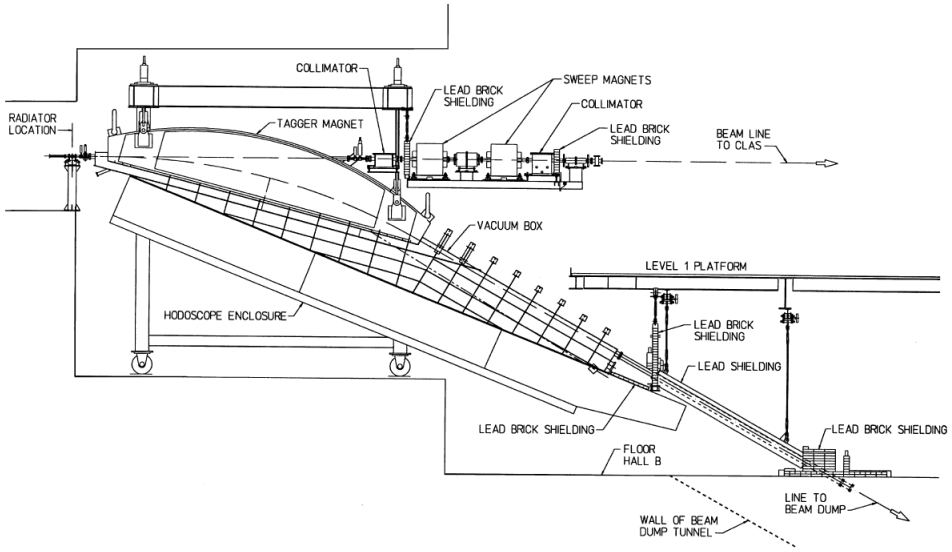

Figure 3.5: A schematic diagram of the Hall B photon tagger system. The radiator, tagger magnet, collimator and tagger spectrometer are the principal components. Image source:[18]

In order to efficiently tag the photons emitted from the collimator, two vital pieces of information are needed about the corresponding detected electron: sufficiently precise measurement of the electron momentum, so that that the photon momentum can be determined with the required degree of precision, and timing data so that coincidence measurements can be performed on any ensuing events that are triggered by the photon. This is obtained using the magnetic spectrometer of the tagger system. The scattered as well as non-interacting electrons are deflected away from the photon beam line by a uniform-field dipole magnet than can produce fields up to 1.75 T. The hodoscope, whose geometry is shown in Figure 3.6 , then detects and records information about these deflected electrons

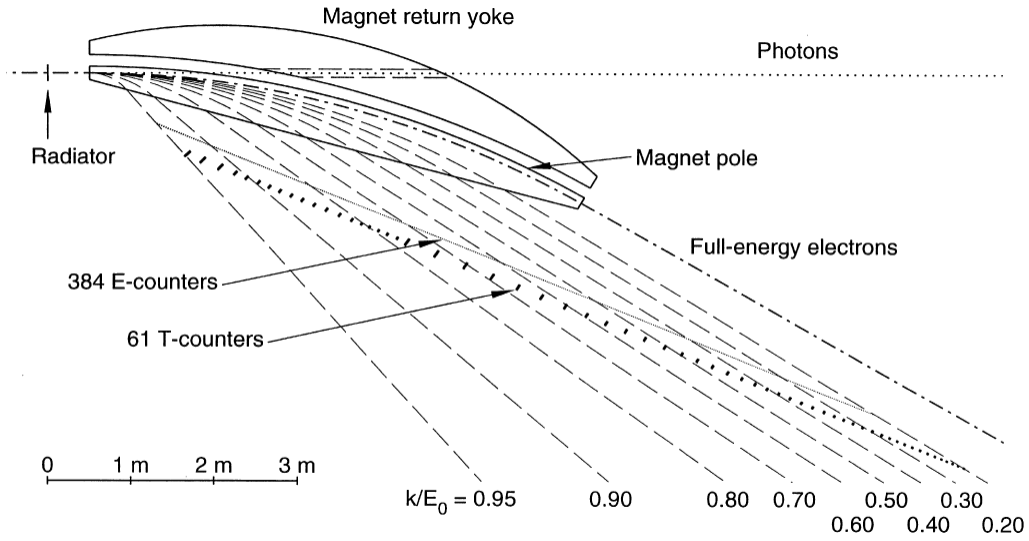

Figure 3.6: Schematic diagram of the tagger spectrometer. The dashed lines represent the trajectories taken by the recoil electron after being deflected by the spectrometer magnet. These are recorded by the E and T counters. The range of the tagged photon energies is 20% to 95 % of the incident electron beam energy[18].

using two planes of scintillators: E-counters to measure energy (momentum), and the T-counters to collect timing information. Both these detector planes are perpendicular to the trajectory of the deflected electron beam. There are 384 overlapping E-counters; they are 20 cm long, 4 mm thick and have widths 8-16 cm. Each electron detected by these scintillators gives information about the energy of the electron based on the location of the counter that is hit. The T-counter plane is 20 cm behind the E-counter plane. These 61 counters are 2 cm thick and give a resolution of about 110 ps. The timing from the T-counters can be used in coincidence with the track timing timing in CLAS to determine which photon was responsible for the interaction.

More information about the design and working of the photon tagger is given in Ref.[18].

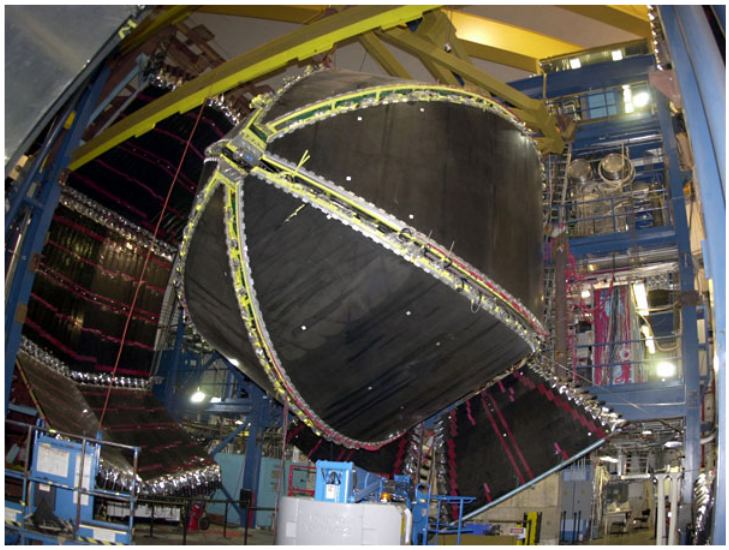

Figure 3.7: Photograph of the CLAS detector after assembly [17].

3.3 The CEBAF Large Acceptance Spectrometer

The main design requirements of CLAS were: good momentum resolution in the measurement of charged particles, large angular acceptance of charged particles, and the ability to use dynamically polarized targets. These requirements led to a detector system based on a toroidal magnetic field. Figure 3.7 shows a photo of the CLAS detector in Hall B. The torus magnet consists of 6 sectors spaced 60° apart; together these produce the toroidal magnetic field which bends positive particles away from the beamline and negatively charged particles towards the beamline.

Several detector sub-systems make up the whole CLAS detector. A start counter (ST), composed of 24 scintillator paddles surrounds the target and is used to record timing information for each event. The three drift chamber (DC) regions determine the charged-particle trajectories. Gas Cerenkov counters help in distinguishing between pions and electrons. The time-of-flight (TOF) of the particles is determined by the use of 6 arrays of scintillator paddles, each array containing 57 paddles. An electromagnetic calorimeter (EC) collects information on the various showers of different particles passing through it,

which can be used for energy determination. A schematic diagram of detector is shown in Figure 3.8. A review of the various components of CLAS is done is Ref. [16].

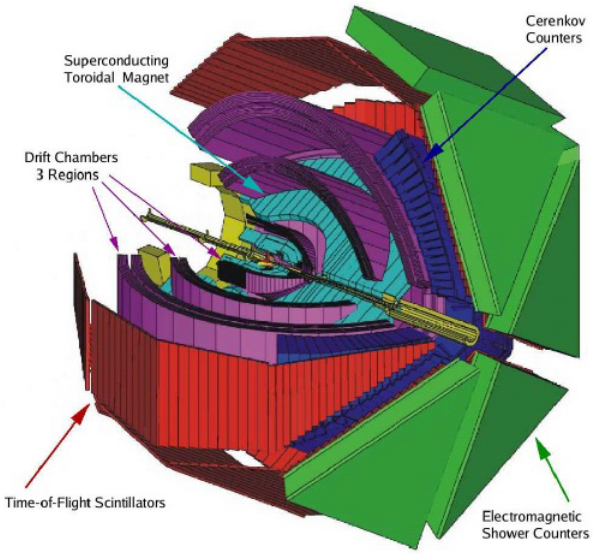

Figure 3.8: Schematic diagram denoting the various components of CLAS. The diameter of the detector is approximately 8m. [17]

3.3.1 The g12 Target

The g12 experiment used a cylindrical target cell, 40 cm in length and 2 cm in radius. The walls of the cylinder were made of aluminum, but the resistance of Kapton to extremes in temperature and radiation made it a good material for the beam windows. Several other experiments have made use of this target cell with different target materials. The target material for g12 was liquid hydrogen. In accordance with the requirements of the experiment, the target was placed 90 cm upstream from the CLAS center. This increased the detection of particles near the beamline, but the trade-off was the inability to detect particles more than 70° away from the beamline. A picture of the target cell can be seen in Figure 3.9

Figure 3.9: The g12 target : The liquid hydrogen is enclosed in a Kapton cylindrical cell of radius 2 cm and length 40 cm [24].

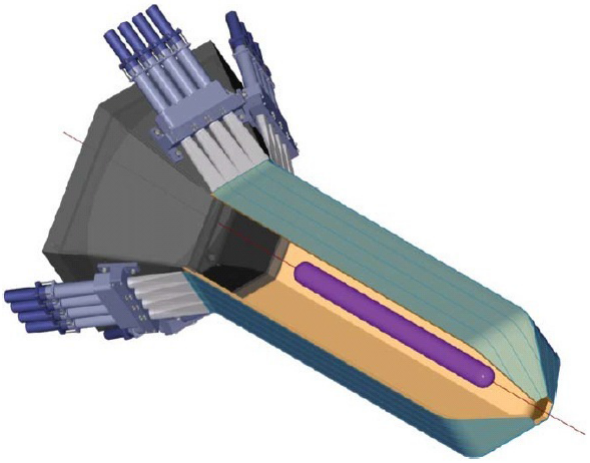

Figure 3.10: A schematic image of the start counter which surrounds the target. Six modules with four scintillators each provide increased segmentation for better handling of high current beams as compared to the previous model [19].

3.3.2 Start Counter

Particle identification with CLAS is done by measuring the time of flight of the particle from the interaction vertex to the TOF or EC detectors. A start counter is needed to determine the interaction vertex, in conjunction with other detectors. Minimization of multiple scattering effects in the ST can be achieved by using thin scintillator strips. The previous version of the ST used a three-scintillator "coupled-paddle" design which could not handle high-intensity runs. The current start counter has six sectors of 4 scintillators

each, which hermetically surround the target. Downstream of the ST, the scintillators curve to form a “nose” . On the opposite end, PMTs are attached to collect the light from the scintillators, see Figure 3.10. The increased segmentation allowed for thinner scintillators, which in turn give a better light yield.

The times recorded by the ST and the TOF counters, along with the path lengths calculated from the drift chambers, give the velocity of the charged particle. The velocity can, in turn be used to calculate the event time by propagating the particle from the ST to the event vertex. High multiplicity events, or, the events in which the number of tracks is greater than two, are able to have a better grasp on the event start time : the event start time is calculated for each track and then an average is taken over all tracks. This time congruous with the tagger T-counter timing determines which photon caused the event.

The segmentation of the start counter is useful for setting up trigger schemes for a particular experiment. Logic circuitry can set up between the tagger T-counters and the ST to control the energy range of the photons, and between the ST and the other detectors like TOF, CC, EC to record events with a set number of tracks or in particular sectors. Ref. [19] has more detailed explanation about the new start counter.

3.3.3 The Torus Magnet

The torus magnet consists of six kidney shaped superconducting coils arranged to form a toroid around the beam line. Each coil consists of 4 layers, each of which have 54 windings of aluminum-stabilized NbTi/Cu conductor. Figure 3.11 shows a photograph of the magnet coils before installation of the other sub systems and Figure 3.12 shows the cross-section of the magnetic field. The contours are the field lines in the plane between coils. For the g12 experiment, the field pointed into the page. The regions 1, 2 and 3 indicated in the figure are the three drift chamber regions. Region 2 of the DC is located inside the region of the coils. A larger picture can be seen in Figure 3.8.

Figure 3.11: Photograph of the coils of the CLAS toroidal magnet before installation of the rest of the detector sub-system [26].

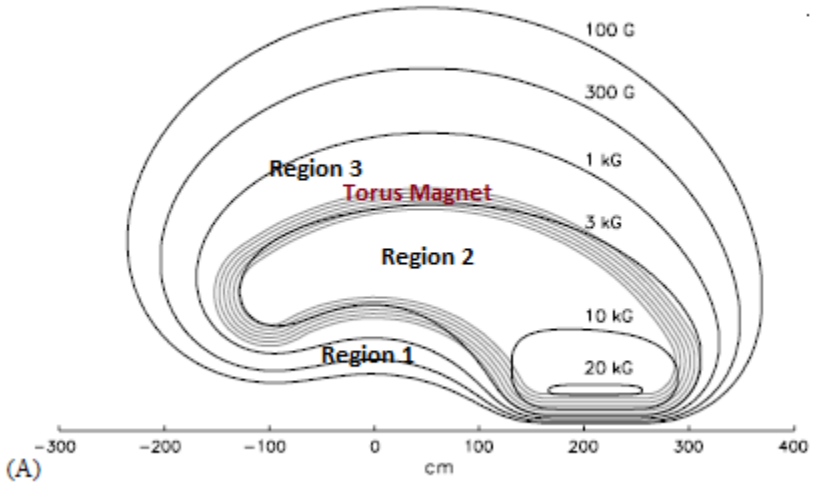

Figure 3.12: Diagram depicting the contours of the magnetic field of the toroidal magnet in the midplane between two coils. The gray lined area is the projection of the magnet in the midplane. The regions 1, 2 and 3 labeled on the diagram are the locations of the three drift chamber regions. Image source: [16]

The magnetic field is mostly in the ϕ direction except in the the region close to the coils. Refer to Figure 3.12 to see the magnetic field vectors transverse to the beam. The inner shape of the coil is circular to minimize the deviations from the ϕ field near the

coils. Due to the kidney-shaped coils, particles with higher momentum (forward direction) experience larger field effects than particles with lower momentum (emitted at large angles from the beam line). For the g12 experiment, the magnet was operated at a current of 1930 A, which is half its capacity. The field direction causes positively charged particles to bend away from the beam line and negatively charged particles to bend into the beam line. Thus, positively charged particles have a greater acceptance than negatively charged ones. A larger current could give better momentum resolution, but would cause a greater deflection, thus reducing the acceptance of these negatively charged particles. Since the experiment requires detection of a wide variety of particles, a lower current value was chosen to give a reasonable trade-off in these two variables. The coils are cooled to 4.5 K during operation of the experiment using super-critical helium. Refer to Ref. [26] for more information about the CLAS magnet.

3.3.4 Drift Chambers

The field of the toroidal CLAS magnet deflects the charged particles away from or towards the beam line, but does almost nothing to their azimuthal angle. This makes it easy to resolve the tracks into 6 sectors. The drift chamber, consisting of three regions for each sector, records the tracks of these charged particles. Knowing the direction and strength of the magnetic field, the tracks can be used for momentum determination of the particles.

Region 1 (R1) is located inside the CLAS torus, Region 2 (R2) is placed between the coil cryostats, and Region 3 (R3) is attached to the outside edges of the cryostat. Since R2 is located within the magnet, it experiences the largest field , and thus has maximum track curvature, providing good momentum measurements. R3 is the largest of the three regions with the largest radius. This is depicted in Figure 3.14 and Figure 3.15a . Each region of every sector has two superlayers (Figure 3.15 b), each of which consists of a hexagonal pattern of six layers. Each layer consists of an array of 20 μm gold-plated tungsten field

wires each surrounded by six 140 μm gold-plated aluminum alloy sense wires. This creates a honeycomb-like pattern where each layer is offset from the adjoining one by half a cell width.

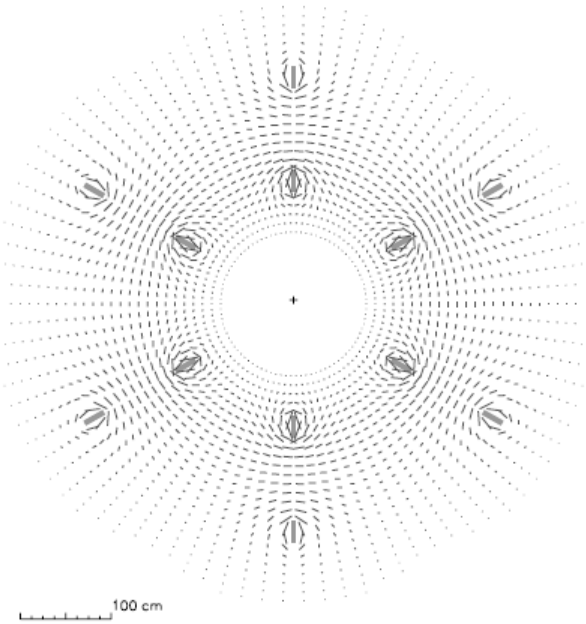

Figure 3.13: The magnetic field vectors transverse to the beam in a plane centered on the target. The gray rectangles are the projections of the six sectors of the magnet The lengths of the field lines are proportional to the strength of the magnetic field at that point [16].

Of the two superlayers, one has the sense wires perpendicular to the plane between coils (or axial to the magnetic field), while the sense wires in the other superlayer are oriented at 6° stereo angles. This placement provides information about azimuthal movement. The sense wires are maintained at a positive potential and the field wires at a negative potential. The gas inside the DC is a mixture of 90% argon and 10% carbon. This non-flammable mixture is easily ionized by charged particles passing through it and create a signal that passed through preamplifiers and amplifier discriminator boards (ADBs) and then to time-to-digital convertors (TDCs) to obtain timing information.

More information about the design, construction, installation, electronics and calibration of the DC is given in Ref. [22].

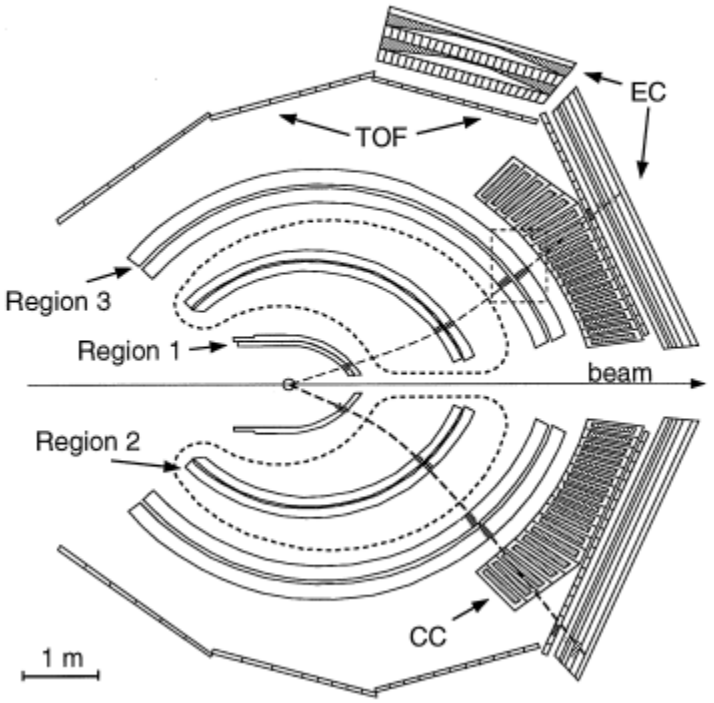

Figure 3.14: A schematic representation of the horizontal cross-section of the CLAS detector indicating the three drift chamber regions. The dashed lines surrounding region 2 indicate the toroidal magnet [22].

3.3.5 Time of Flight Detectors

The time of flight detector is an important part of the detection system. It provides timing information which, in conjunction with the start counter, can be used in particle identification. The TOF system is placed between the Cerenkov counter and electromagnetic calorimeter. It has six shells, one for each sector of the CLAS detector and every shell has 57 scintillator paddles of varying lengths mounted in four panels with phototubes on both ends, see Figure 3.16. The first 23 cover the polar angles 8.6°through 45.9° and are the forward angle scintillators; they have a width of 15 cm and are fitted with 2 in PMTs.

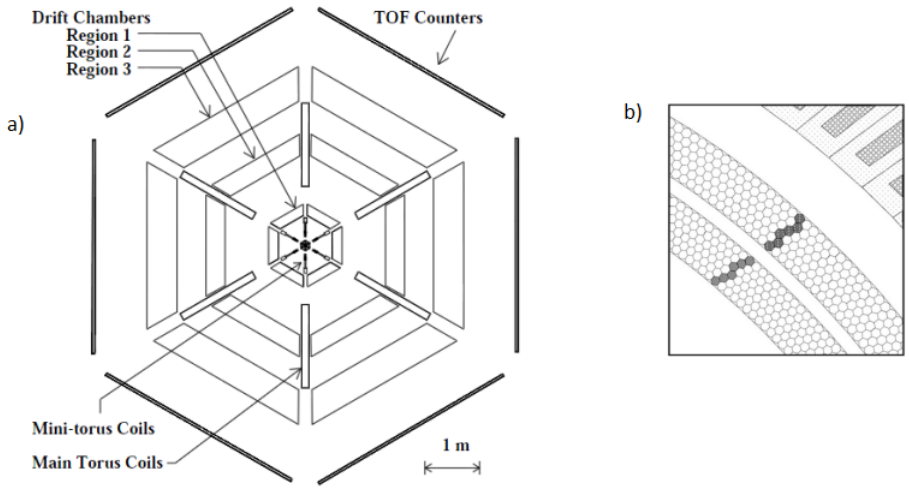

Figure 3.15: (a)Schematic diagram of the vertical cross-section of the CLAS detector representing the geometric location of the drift chamber regions in relation to the torus magnet. (b)Rendition of a portion of a region 3 chamber, which shows the layout of its two superlayers. Each hexagon houses a sense wire at the center which is surrounded by six field wires at the vertices. The path depicted by the highlighted cells indicates the drift cells that have fired [22].

Scintillators 24 - 53 operate at angles 47.4° to 131.4° and are 22 cm wide and fitted with 3 in PMTs. The last four are again 15 cm wide with 2 in PMTs and operate at angles 134.2° to 141.0°. All scintillators are 5.08cm thick, made of Bicron BC-408 scintillating material with lengths ranging from 32 cm to 445 cm . The last 18 paddles are coupled in pairs, thus giving a total of 48 logical counters per sector. The timing resolution of the TOF system ranges from 80 to 160 ps depending on the length of the scintillator paddles. The PMT output is read by various TDC and analog to digital (ADC) components. Though the ADC is used mainly for calibration, it can also be used for rough particle identification using the energy deposited in the TOF. This is not a reliable method to distinguish between kaons and pions.

Ref. [23] details the geometry, components, assembly and electronics of the TOF system.

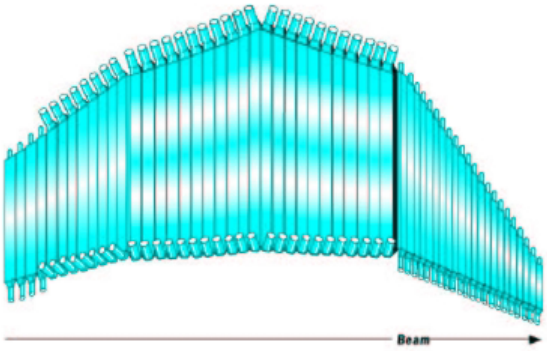

Figure 3.16: A diagram of a single sector of the time-of-flight (TOF) system [23] .

3.3.6 The Cerenkov Counter

The Cerenkov detector is an important component in separating pions and electrons. It is arranged between the drift chamber and the TOF scintillator system and can detect particles with polar angles between 8° to 45°. In the g12 experiment, due to the placement of the target 90cm upstream, the actual coverage is 6° to 35°. Similar to the other components, the Cerenkov system is also made up of six sectors. Every sector consists of 18 regions, each of which have a small angular range. Each region is further divided into 2 symmetric modules.

Each module consists of a combination of elliptical and hyperbolic mirrors, see Figure 3.17. Light emitted by the traversing electron hits the elliptical mirror and is reflected to the hyperbolic mirror. From there it is reflected again and collected PMTs and recorded. The CC is filled with perfluorobutane (C_4F_{10}) gas which has a refractive index of 1.00153. Pions below 2.5 GeV momentum do not travel faster than light in this medium and hence do not emit Cerenkov light. This is used as a discriminating factor between leptons and pions with an upper limit of 2.5 GeV. Kaons and protons have a much higher threshold than the maximum energy of g12, and hence do not leave any trace in the CC.

The rapid response time of the CC makes it useful for trigger configurations in conjunction with the electromagnetic calorimeter. More information about the CC can be found in Ref.[20].

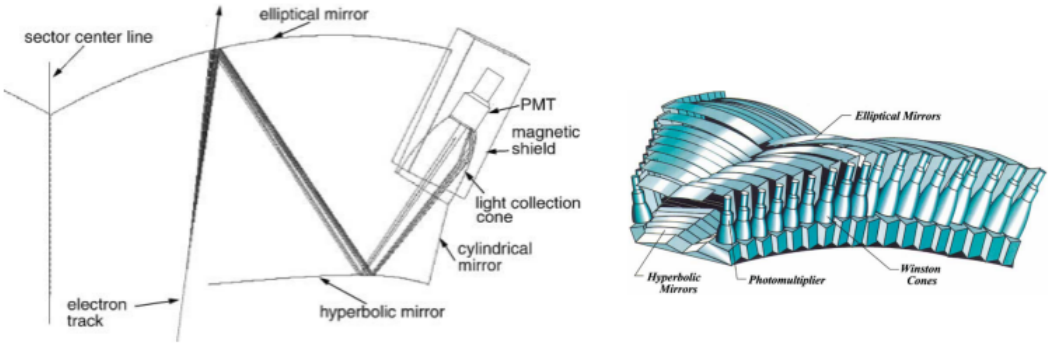

Figure 3.17: **Left**: Details of a single module of the Cerenkov Counter (CC). There are 216 such modules in the CC. **Right:** Diagram of the eighteen modules of a single sector [20].

3.3.7 Electromagnetic Calorimeter

The electromagnetic calorimeter (EC) is the final component of the CLAS system. The EC independently measures the energy of the recorded particles and is especially useful for reconstructing high energy neutral particles like photons and neutrons. The distinction between neutrons and photons can be made using TOF measurements. The EC can detect electrons above 0.5 GeV and this information can be used for setting up trigger configurations on account of its fast response time.

The EC is also divided into six sectors, like the rest of the CLAS sub systems. Each sector is shaped as an equilateral triangle with 39 layers of scintillator strips alternating with lead sheets. The total thickness of this sandwich structure is 16 radiation lengths. Each layer is composed of 36 plastic Bicron BC412 scintillators of dimension 1 cm x 10 cm and varying lengths thickness and a 2 mm sheet of lead. The scintillator lengths vary from 15 cm to 420 cm. They are placed such that they are parallel to one of the

ends of the equilateral triangle and each successive layer is rotated by 120° so that there are three orientations labeled U, V, and W views as shown in Figure 3.18. The area of each successive layer increases to minimize the shower leakage at the edges and also the dispersion in arrival time of the signals from different layers. The scintillator signal is transmitted to photomultiplier tubes by wavelength shifting optical fibers which absorb blue light and re-emit green light.

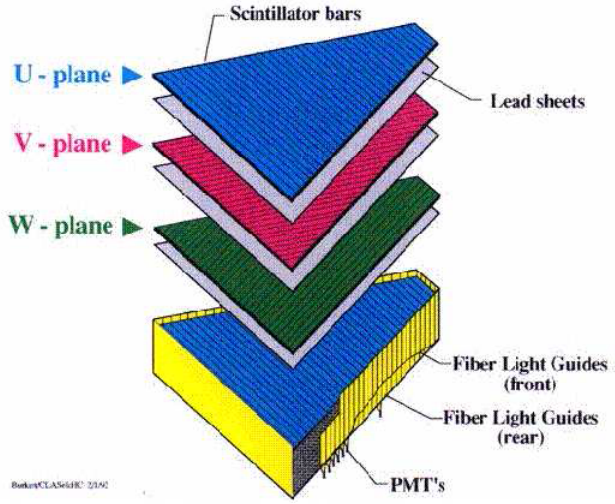

Figure 3.18: Diagram representing the three orientations of the scintillator layers in each sector of the electromagnetic calorimeter [21].

A single sector is divided into an inner stack consisting of the first fifteen layers (5 bundles of U-V-W view layers) and an outer stack made up of the remaining 24 layers. Consider the inner stack: the reading from the same numbered scintillator strip from each layer for a particular view is fed into one PMT, *i.e.,* strip 1 from each of the five U views is read out at PMT U1, strip 1 from each V view is read out at PMT V1 etc. Thus there are 36 x 3 = 108 PMTs for the inner stack. The same method is employed for the outer stack and hence each sector has 108 x 2 = 216 PMTs. The EC as a whole has 8424 individual scintillator strips and 1296 photomultiplier tubes.

Due to the way the signal is read out, a particle shower will give rise to three lines, one for each view (refer to Figure 3.19). This information can then be used by reconstruction software to make timing, position and energy calculations. Refer to Ref. [21] for an exhaustive description of the EC.

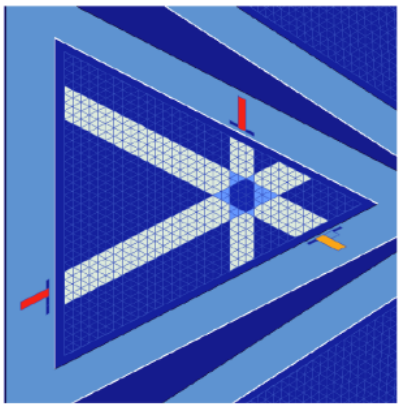

Figure 3.19: Representation of a simulated electromagnetic shower reconstructed in the inner layer. The three white lines are the signals from the energy deposition in each of three orientations [21].

3.4 Beamline Devices

Various devices were used during the g12 run to monitor the characteristics of the beam. These include two Beam Position Monitors (BPMs), three harps, a Total Absorption Shower Counter (TASC), a Pair Spectrometer (PS) and a Pair Counter (PC).

The BPMs, each consisting of two RF cavity monitors, are placed 36 m and 24 m upstream of the CLAS photon target to measure the x-y position and intensity of the electron beam. Harps are beam profile scanners located at 36.7 m ,22.1 m and 15.5 m upstream from the CLAS target. They consist of a set of perpendicular wires which are at 45° to the scanning motion. PMTs attached to the beam pipe, ~10 cm away from the beam are located 6.8 m upstream of the CLAS target; they act as counters for the signal from the harps. Harps act as localized radiators, and the scattered electrons emit Cerenkov light in

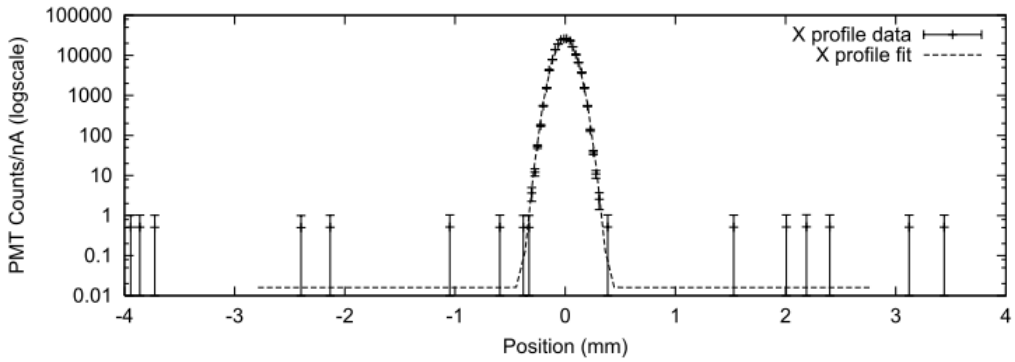

Figure 3.20: An electron beam x-profile measured by one of the harps. The dashed line is a Gaussian fit to the data [16].

the glass windows of the PMTs. Figure 3.20 shows a harp scan profile. Since the scanning by harps is an invasive process, it is only done when no data is being taken by CLAS.

The TASC, PS and PC are located downstream from CLAS and measure the photon flux. The TASC, made up of 4 lead-glass blocks, is capable of measuring the absolute photon flux with almost 100% efficiency, but it can be operated only at low currents of up to 100 pA. For this reason, it is used for calibration purposes on normalization runs where the current is low. The PS and PC have a much lower efficiency in measuring the photon flux, but they can run at higher currents and hence they are cross-calibrated with the TASC at low currents and then operated during the normal production runs of CLAS. The PS consists of a thin radiator, a dipole magnet and eight scintillators. The radiator converts the photons into e^-e^+ pairs which are deflected in the opposite direction by the magnet and detected by the symmetrically placed scintillator counters. The PC is a back-up monitor which consists of a thin convertor, a single front scintillator and 4 slightly overlapping rear scintillators. The e^-e^+ pairs created by the converter are detected by the rear and front scintillators to give rough information about the beam profile and lateral position stability. Figure 3.21 shows the layout of these downstream devices.

Refer to Refs. [18] and [16] for more information about the various beam line devices. The whole ensemble of the CLAS detector system along with the beamline components is depicted in Figure 3.22.

3.5 Data Acquisition System and Trigger Configuration

The Data Acquisition System (DAQ) consists of elaborate circuitry and electronics that collects the information from the various detector subsystems and writes it out in some particular format. The ST, DC, TOF CC, EC all have similar electronic modules for readout of the data collected from their instrumentation. This assortment of signals is fed to the DAQ for further processing. However, the presence of a signal in a detector element does not necessarily signify a physics event: there exists a lot of background due to cosmic rays, electronic noise, etc. A set of *trigger* conditions is put in place to define the requirements for the recording of a signal.

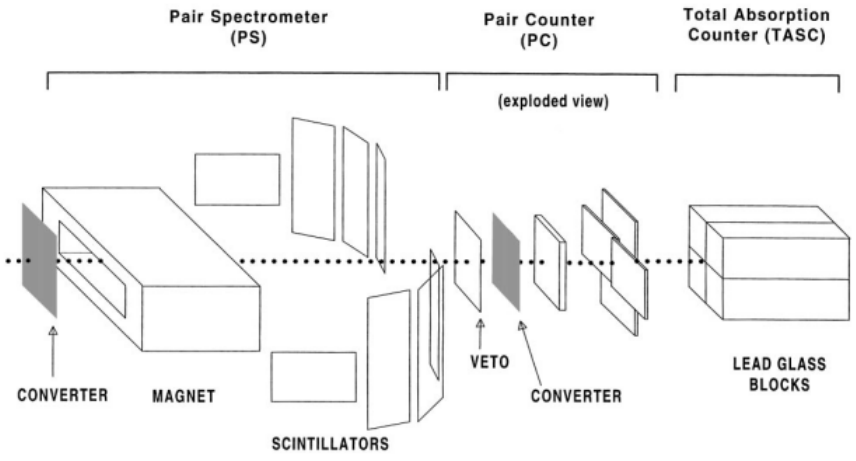

Figure 3.21: Layout of the beam monitoring devices downstream from CLAS [18].

The signals from each sub-system are first passed through a discriminator circuit which rejects signals below a pre-determined threshold so that physics events are selected. They are then digitized by two hardware systems: time to digital converters (TDC) and

analog to digital converters (ADC). The job of the TDC is to measure the time at which a particular signal was received, while ADCs report the amplitude of the signal by determining the energy deposition in the detector. This information is read out to the DAQ.

For the main trigger configuration, the presence of at least two charged tracks was required, where each charged track was verified by coincidence of a TOF signal in a particular sector with an ST signal in the same sector. This was then placed in coincidence with logical Master-OR (MOR) units to set the photon energy range. Different ranges of energies, specified by MORA and MORB, were used for different sets of runs. Though all the T-counters were functional, only the first 47 were used so that events below a certain energy were discarded. For lepton analysis, triggers were set based on coincidence with the EC and CC. A summary of the various trigger configurations can be found in Ref. [27].

The data for the g12 experiment was taken in several runs, each consisting of about 50 million triggers at a rate of ~8 kHz. Runs with less than 1 million triggers were discarded. This high rate was due to the use, for the first time at CLAS, of a Field-Programmable Gate Array (FPGA) logic control processor in the trigger system. 26 billion events were recorded, equivalent to 68 pb^{-1} of luminosity.

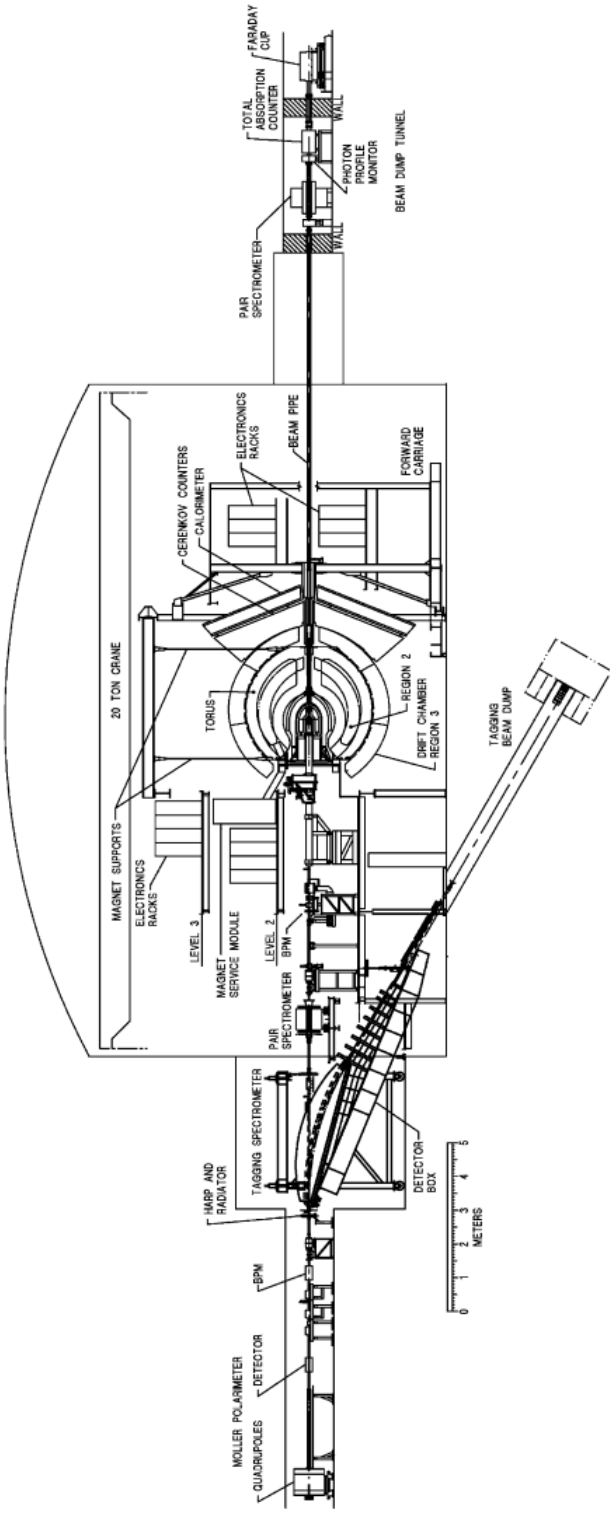

Figure 3.22: Side view of CLAS along with all associated equipment [16].

4 CLAS 12 PRESHOWER CALORIMETER

The detector described in the previous chapter ran while the CEBAF electron beam had a maximum energy of 6 GeV. Jefferson Lab has since upgraded its facility to have double that energy. The previous detector is now referred to as CLAS 6 and the upgraded one is CLAS 12. The higher beam energy means that the energy of electrons and photons impinging on the detector will be too high to be contained by the existing CLAS 6 electromagnetic calorimeter (EC). Several of the experiments commissioned to be performed using CLAS 12 require the accurate detection of neutral pions via their decay into two photons. The opening angle of the emitted photons decreases as the energy of the neutral pions increases. At the energies of CLAS 12, the calorimeter needs to have a very good position resolution in order to be able to detect both photons and to avoid labeling the two as a single photon. Thus, it was necessary to update the detector sub-system in order to improve its functionality at higher energies. To do this, another calorimeter, the preshower calorimeter (PCAL) is to be placed in front of the EC, the design and construction of which will be discussed in this chapter. As seen from Fig. 4.1 , a simulation to test the efficiency of the calorimeter with just EC and both EC and PCAL shows greater efficiency at high pion momentum with both sub-systems in place instead of just the EC.

4.1 Geometry

The preshower calorimeter (PCAL) is built with a similar geometry as the CLAS 6 EC. There are three views, U,V and W which are arranged alternatingly with a lead sheet between each scintillator layer. The PCAL is placed in front of the EC and the EC-PCAL system will act as the calorimeter for CLAS 12. One main difference in the construction is that, contrary to the EC, the PCAL does not have a progressive geometry, and all the layers of scintillators have the same area throughout. Each sector has 5 layers of each view, *i.e.*, 15 scintillators layers (and 14 lead layers). To be able to differentiate between two photons

which are emitted very close to each other, the PCAL also has a higher segmentation than the EC. A U-layer has 84 strips and the V and W layers have 78 strips each.

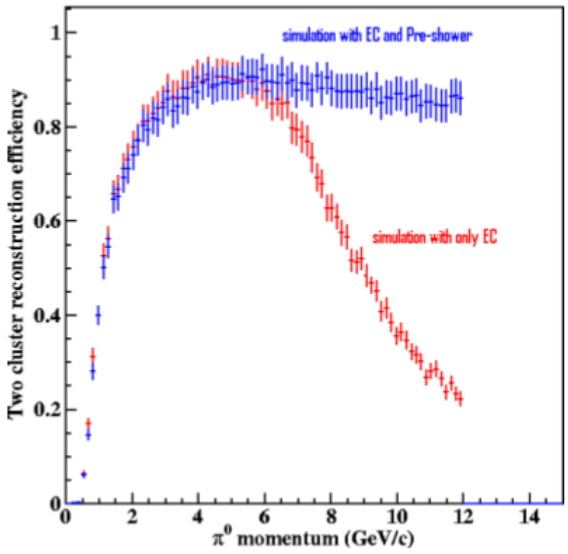

Figure 4.1: Simulation to test the efficiency of two-photon cluster reconstruction of $\pi^0 \rightarrow \gamma\gamma$ decays.[141]

The scintillator emits blue light after having absorbed energy from the traversing particles. The inner surface of each scintillator is coated with a reflecting material made of TiO_2 polystyrene, in order to contain the light within its area. However, polystyrene has a very small attenuation length for blue light, about 20-50 cm., which is not long enough for the light to be transmitted through scintillators which can have a maximum length of ~400 cm. To overcome these difficulties, wavelength shifting (WLS) optical fibres are used inside the scintillators, parallel with its length. These WLS fibres absorb the blue light and emit green light. The measured values for the attenuation lengths of the WLS fibres are greater than 3 m and in some cases, as high as 6 m. About 5% of the scintillator-emitted light is absorbed by the fibres. The fibres in the EC were embedded in grooves in the surface of the scintillator, whereas in PCAL, two holes are drilled through the scintillator and a pair of fibres are inserted through each hole (Fig. 4.4). The light from these fibres

is then collected by PMTs, and converted into an electric pulse. The area of this pulse is proportional to the energy of the shower. Analysis of these pulses by fast flash ADCs provide energy, time and location for single and multiple events.

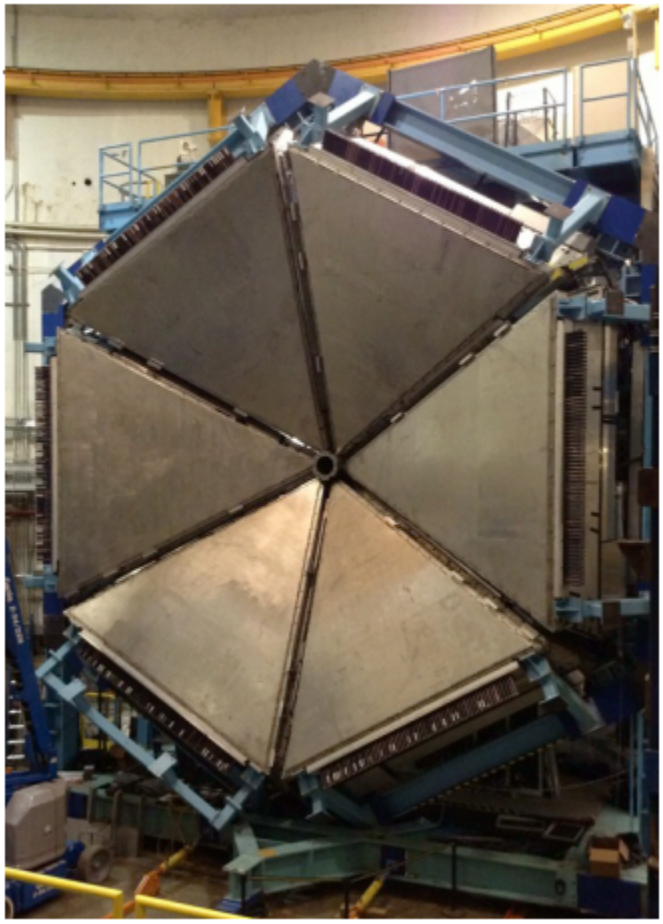

Figure 4.2: Arrangement of the completed PCAL with all six sectors, which will be placed in front of the EC.[142]

Of the 84 U-scintillators, the 52 shortest strips are read out by individual PMTs. For the remaining 32 strips, one PMT is employed to read out two scintillators, effectively doubling the width of the segment. Thus, there are a total of 68 PMTs for the U-view. For the V and W views, the longest 46 strips are read out individually, and for the shorter 32 strips, 2 strips form one read-out channel. The V and W views thus require 62 PMTs.

High energy pions will be deflected towards forward angles, which have the shortest U strips. This area of the PCAL has the shortest U-strips and the longest V and W strips. Thus, the width of the transverse segmentation is variable, unlike in the EC which has fixed segmentation width. A diagrammatic representation of this arrangement is depicted in Fig. 4.5

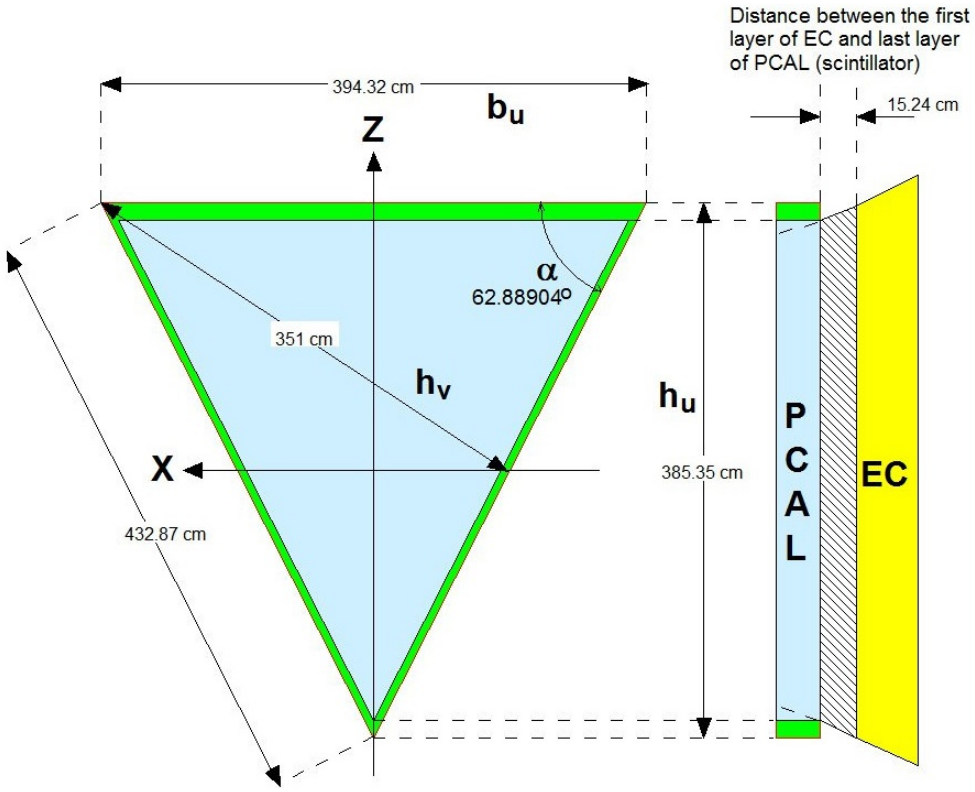

Figure 4.3: Dimensions of each sector of PCAL. [136]

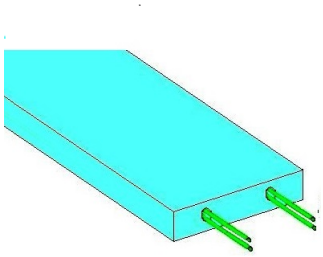

Figure 4.4: Scintillator-fibre system of the PCAL.[136]

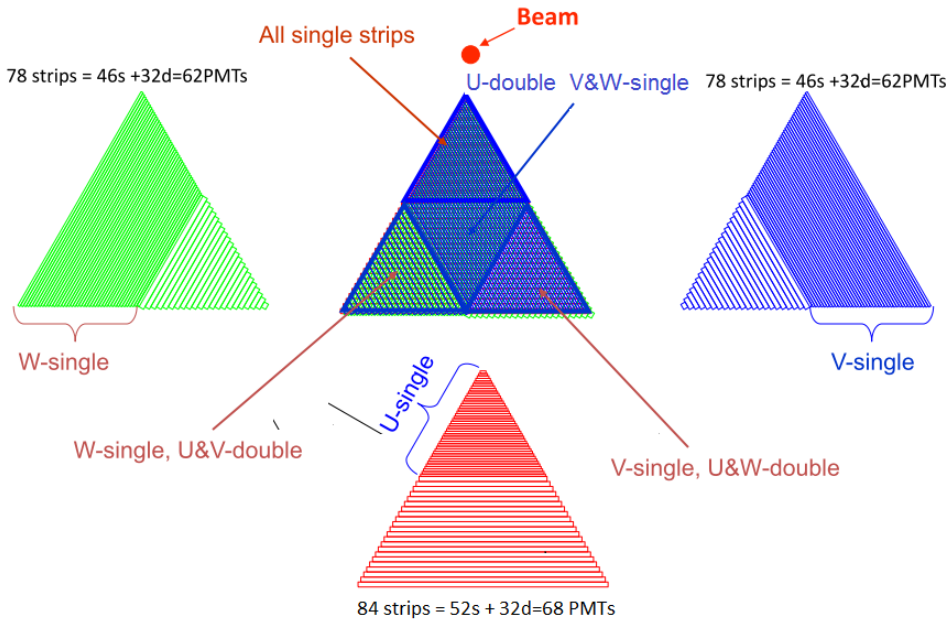

Figure 4.5: Variation in the width of the transverse segmentation of the layers.[135]

Of the 84 U-scintillators, the 52 shortest strips are read out by individual PMTs. For the remaining 32 strips, one PMT is employed to read out two scintillators, effectively doubling the width of the segment. Thus, there are a total of 68 PMTs for the U-view. For the V and W views, the longest 46 strips are read out individually, and for the shorter 32 strips, 2 strips form one read-out channel. The V and W views thus require 62 PMTs. High energy pions will be deflected towards forward angles, which have the shortest U strips. This area of the PCAL has the shortest U-strips and the longest V and W strips. Thus, the width of the transverse segmentation is variable, unlike in the EC which has fixed segmentation width. A diagrammatic representation of this arrangement is depicted in Fig. 4.5

The left wall of the box when facing the beam has the read-out channels for the U-strips, while the read-out channels for the V and W views are at the top wall. This is another difference with the EC, in which the output from each view is read out from separate sides of the wall.

4.2 Testing Procedures

4.2.1 Scintillator-Fibre System

A uniform response over the PCAL area requires the characterization of the transmission properties of the scintillators. As the irradiation source, the radioactive $^{90}\mathrm{Sr}(\beta)$ was mounted on a mechanical system that could be moved automatically along the strip. The source was moved 10 cm at a time and a corresponding measurement was taken at each step, as will be explained in this section. In the extrusion process, a scintillator bar is cut into the desired length such that one bar can form two strips in a particular view. For example, in the U view, the 1^{st} and the 84^{th} strip are cut from the same bar, the 2^{nd} and the 83^{rd} strip are cut from the same bar, and so on. Due to this, it is only necessary to test the longest scintillators. The process, which required two persons, is described below.

1. Gloves were used at all times while handling all the materials. The importance of turning off the high voltage supply before opening the dark box was stressed, since failure to do so would result in too much light being transported to the PMT necessitating its replacement.

2. For each view, the longest scintillator was measured first. A visual inspection of the strip was done to ensure the absence of scratches or other visible defects. Then, to clean the holes in the scintillators, the strip was placed on the staging table, and a long stainless steel wire was inserted into each hole and shaken to remove any visible debris in the hole. Gaseous nitrogen was then blown into each hole using a pressure valve to ensure the hole was free from debris.

3. Two test fibres were carefully inserted into each hole. The careful handling of these fibres was very important since defective fibres would give incorrect readings of the light output.

4. The scintillator-fibre system was then placed on the setup in the dark box such that the edge of the scintillator coincided with the zero marking on the aluminum profile (refer to Fig.4.6 and Fig. 4.7, Left). It was made sure that the fibres on this side were properly resting in the box.

5. On the other end of the scintillator, the fibres were inserted into a plastic adapter and then glued to ensure a proper connection. This adapter was then carefully inserted into the PMT housing such that it touched the photocathode.

6. The dark box was then closed and the top was secured using latches.

7. The HV was switched on and set to a value of 1000V.

8. The mechanical setup of the radioactive source was controlled via a computer. A GUI was used to input the sector, layer, view and scintillator number. This would then create a corresponding output file with the recorded readings. The $^{90}\mathrm{Sr}(\beta)$ source moved in steps of 10cm. At each position, 500 measurements of the PMT anode current were taken; the average and standard deviation of these measurements were recorded. To measure the 'dark current', or the background, one reading was taken after the source had moved beyond the length of the scintillator.

9. The HV was switched off and the adapter was detached from the PMT. The scintillator-fibre system was then moved to the staging table and the fibres were carefully removed from the tested scintillator strip. The tested strip was moved to the storage shelf.

10. To check the quality of the scintillator, the response of the PMT was plotted for each position of the radioactive source. If the typical response was seen (Fig. 4.7, Right) the scintillator was deemed fit to be installed in the final assembly.

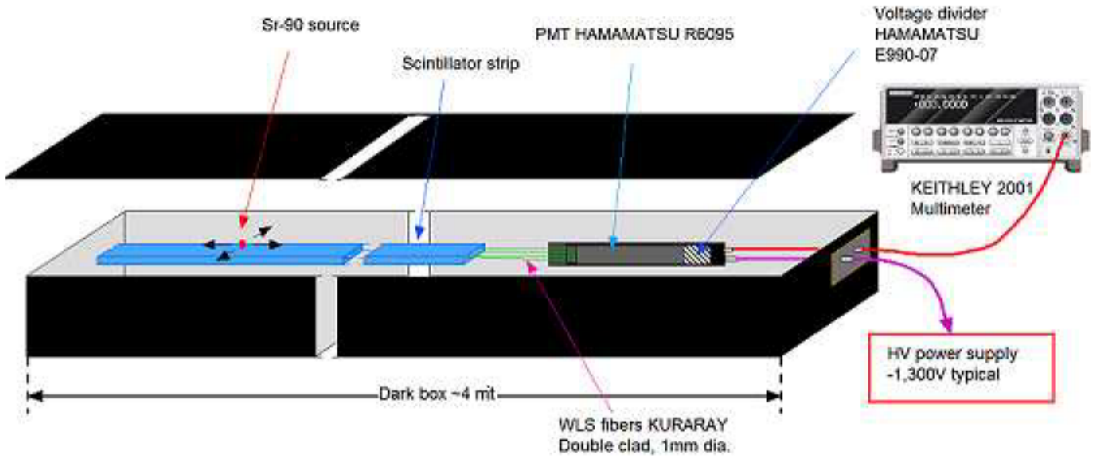

Figure 4.6: Schematic representation of the testing system, which includes the dark box, the scintillator-fibre assembly, the ^{90}Sr(β) source, a PMT, a HV power supply and a Keithley Multimeter[137].

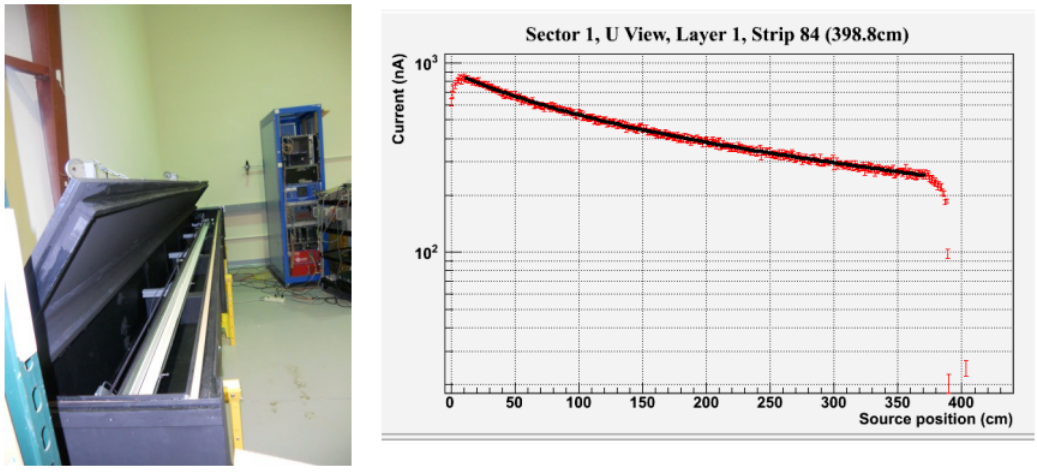

Figure 4.7: Left: Dark box which was used to conduct testing of the scintillator-fibre system. Right: Light-attenuation curve from one of the scintillator strips.[142]

4.2.2 Fibres

Each set of fibres was contained in a plastic wrapper. Several sets of these fibres were placed in a wooden box to minimize exposure to light and dust. To test these fibres, the same setup as that to test the scintillators was made use of.

1. The set of fibres was placed on the stacking table. 4 fibres were chosen at random from the set. These were visually inspected to make sure that none were broken.

2. These 4 fibres were moved to the dark box and placed on the setup such the length of the fibres rested on the aluminum profile.

3. At one end, the fibres were connected to the PMT in the same manner as step 5 of Section 4.2.1.

4. At the other end, the fibres were inserted into a short test scintillator (about 10 cm in length).

5. The dark box was then closed and the top was secured using latches.

6. The HV was switched on and set to a value of 1000V.

7. Using the GUI, the fibre serial number and set number was entered. The measurement was only done at one point on the scintillator-fibre system. Another measurement was taken to record the dark current. In this case, only 20 measurements were taken, and the average and standard deviated was recorded.

8. The HV supply was then switched off and. After carefully detaching the fibres from the PMT, and removing them from the test scintillator, the fibres were placed back on the staging table.

9. The value of the PMT anode current was then checked to be above 15% of the nominal value, if not, that particular bunch of fibres was separated from the rest. The

questionable fibres were then visually inspected individually to check for defects. If none were found, then testing different combinations of these fibres with new ones, the 'bad' fibre was identified and discarded.

10. This procedure was repeated for 4 more bunches of fibres in the given set.

4.2.3 Lead

The thickness of the lead sheets was mapped out using an ultrasonic thickness gauge (model TI-25DL).

1. Before starting the measurements, the lead sheet was first cleaned using isopropanol to remove residual oil or dirt.

2. A drop of coupling liquid was used between transducer and lead for good sound transmission. Measurements were taken at 32 places along the sheet to check for consistency in its thickness.

3. The sheet was then cleaned to remove the coupling liquid.

4.3 Stacking Procedures

4.3.1 Scintillators

It was required to wear gloves and clean-room coats while working on this.

1. The PCAL box assembly was cleaned using isopropanol to remove debris and grease.

2. A layer of 0.5 mm thick Teflon sheets was laid on the bottom wall of the box so as to cover the area before laying down the scintillators.

3. The U layer was installed first, followed by the V and then the W. Starting with the longest strip in the layer, the scintillators were first visually inspected, and cleaned with alcohol, and then laid in the box. While stacking the strips, it was endeavoured

to minimize the gaps between two scintillators. Shims were used at the corner of the shortest scintillator so that the strips were pushed towards each other.

4. After a visual inspection of the fibres, a pair of fibres was inserted into each hole of a scintillator.

4.3.2 Lead

The lead sheets were ordered precut as right angled triangles which are half the size of a layer. They were deburred by the manufacturer. It was required that a coat and gloves be used at all times while handling lead.

1. The lead sheet was placed in a wooden table and isopropanol was used to clean the lead surfaces from any residual oil or dust.

2. If the sheet was not flat throughout, wood blocks were used to flatten it.

3. The lead sheet was picked up with the help of gantry crane and several suction cups along the area of the sheet. This was then moved and placed on top of the scintillator layer. Care was taken to ensure that the edge of the scintillator matched the end of the lead sheet.

4. The above procedure was repeated for the second half of lead layer.

50 percent of my time over a period of two years was spent in being involved extensively in all aspects of quality control testing and stacking. I was also a part of setting up the assembly for the cosmic ray testing. This involved cabling and setting up the connectors and measuring devices.

More information about the testing and stacking procedures can be found in Ref. [134]. Detailed expositions about the installation, GEANT and GEMC simulations, as well as cosmic ray testing can be found in Refs.[134]-[141]

5 EVENT SELECTION

The data set that is obtained from an experiment generally has several subsets that can be investigated. Any given subset will be a mixture of the signal events that need to be probed, and background events that investigators try to minimize as much as possible. Several *cuts* are made on the data in order to select events such that the signal to background ratio is large. These selections, however, introduce statistical and systematic uncertainties, and hence one of the objectives of the analysis is to achieve a balance between reducing the uncertainties and increasing the signal size.

The current analysis looks at the photoproduction of scalar mesons via the $K_S^0 K_S^0$ decay channel. The reaction that is studied is :

$$\gamma + p \rightarrow f_0/f_2 + p \tag{5.1}$$

$$f_0/f_2 \rightarrow K_S^0 + K_S^0 \rightarrow \pi^+\pi^- + \pi^+\pi^- \tag{5.2}$$

In the above reaction, the photon beam and the proton target interact via either the s-channel or the t-channel, as shown in Fig. 2.7, to produce a scalar/tensor meson and the proton. The scalar/tensor meson then decays into a pair of short lived neutral kaons (K_S^0), each of which decay into a pair of charged pions. The final state particles are $2(\pi^+\pi^-)p$, of which the four charged pions are detected, while the proton is reconstructed via missing mass off of the pions. Detecting all four pions ensures that the *PC* of the resonant meson is $++$.

5.1 The Basic Cuts

The basic cuts that are applied to the data are listed in Table 5.1. These will be discussed in Sections 5.1.1 through 5.1.5.

Table 5.1: The basic cuts

Cut Level	Type of Cut
1	Timing Cut for identification of pions.
2	Energy loss corrections to correct for the loss energy of the pions while passing through the beam pipe, the target, the start counter, *etc.*, and before reaching region 1 of the drift chamber.
3	Missing mass cut to exclusively choose events with a missing proton.
4	Beam energy cut to remove the events for which the incident photon energy is below the threshold for the production of the $f_0(1500)$.
5	Sideband subtraction

5.1.1 Timing Cut

During the time that the DAQ records one event, several photons can be measured by the tagger. Of these many photons, it is necessary to find that photon which interacted with the target to produce the particle tracks. The tracks measured in the DC are extrapolated to the start counter and also to the TOF counters. Using the time measurements of the hits in the corresponding panels of the counters and the distance between the start counter and the TOF panels, the velocity of the track is calculated. The point of closest approach of the particle track from the DC through the start counter to the beamline is then the vertex of the track. The event start time can now be calculated using the previous calculation of the track velocity and the distance between the vertex point in the target and the start counter. This gives the start time for that track. This entire calculation is done for every track in the event and the average of the start times for all tracks is taken as the event vertex time.

To identify and select the detected particles as pions, the Time of Flight (TOF) Difference method is employed. In this method, the difference between the calculated and measured time of flight is constrained to be within 1ns. The calculated TOF is determined in the following manner: The mass of the particles is assumed to be the mass of the charged

pion, *i.e.,* 139.57 MeV. Then, using the measured momentum of the particle, we can calculate the time required by the π^+or $\pi^-$to traverse the path, L_{sc}, from the target to the TOF counters.

$$\beta_{calc} = \frac{p_{measured}}{\sqrt{p^2_{measured} + m^2_{\pi}}} \tag{5.3}$$

$$TOF_{calc} = \frac{L_{sc}}{c\beta_{calc}} \tag{5.4}$$

where c is, as usual, the speed of light.

The measured TOF is the difference in the time that the SC records as a hit (t_{sc}) and the event vertex time (t_{vertex})

$$TOF_{measured} = t_{sc} - t_{vertex} \tag{5.5}$$

The difference between the measured and calculated TOF,

$$\Delta TOF = TOF_{measured} - TOF_{calc} \tag{5.6}$$

is plotted versus the particle momentum in Fig. 5.1. The dark band around the zero of the vertical axis in the left plot contains the pions. A cut is made on this region to select these events. If this cut leads to the selection of at least two positively charged pions and at least two negatively charged pions, then the event is passed on for further scrutiny.

For every photon measured during the event, the tagger measures the time of the corresponding scattered electron. Using this time and the distances for the electron to travel from the radiator to the tagger and the photon to travel from the radiator to the target, the time of arrival of the photon at the event vertex can be inferred. This photon whose vertex time matches most closely to the average start counter vertex time is chosen. Depending

on the electron beam current, there can be more than one 'good' photon. Using the four-momenta of the four pions, the target and the photon, the missing mass off of the four pions can be calculated and the photon which gives greater agreement with the mass of the proton is chosen.

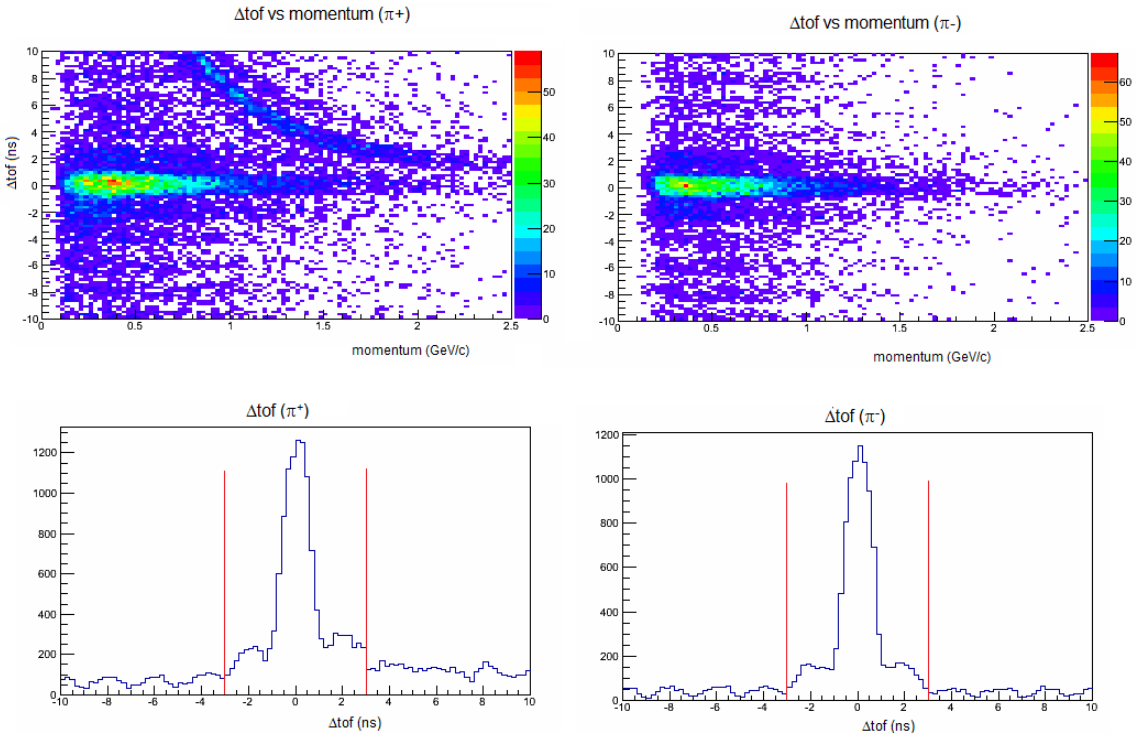

Figure 5.1: Timing cuts: The top plots denote ΔTOF of the pions as a function of their momentum, whereas the bottom two figures are 1-dimensional plots of ΔTOF for $\pi^+ s$ and $\pi^- s$. Those particles with $\Delta TOF = 3ns$ are selected. Cut Level:1

5.1.2 Energy Loss Corrections

The CLAS detector has several sub-detector systems, as described in Chapter 3, and the reconstruction process of the decay particles starts at the drift chambers, where the tracks of the particles are recorded to measure their momenta. Before reaching reaching region 1 of the drift chamber, however, the particles undergo energy loss while traversing through the target, start counter and their associated assembly materials. To account for

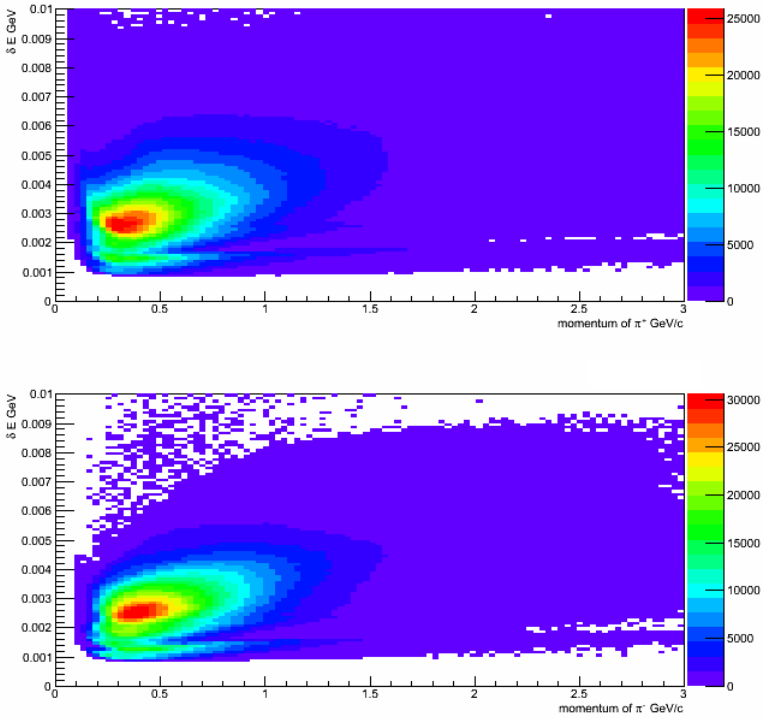

Figure 5.2: Energy correction, δE, v/s momentum of pions. The top plot illustrates this for π^+ and the bottom plot for π^-.

this energy loss, a standard CLAS package called `eloss`, authored by Eugene Pasyuk[11], is employed. It corrects for the loss of energy using the Bethe equation[10], which relates the energy loss of a particle through a material with the characteristics of the material, and the distance traveled by the particle in the said material. The energy correction is the difference between the energy corrected by the `eloss` package, E_{corr}, and the uncorrected energy, E_{unocrr} :

$$\delta E = E_{corr} - E_{uncorr} \tag{5.7}$$

Fig.5.2 shows the energy correction for both the $\pi^+$and the π^-.

Fig. 5.3 shows the invariant mass spectra of a charged pion pair ($= Mass(K_S)$) before and after correction. The red curve, which denotes the spectrum after the eloss

correction has been applied, peaks at 0.4977 GeV, very close to the PDG value of 0.4976 GeV, as opposed to the uncorrected peak value of 0.4957 GeV.

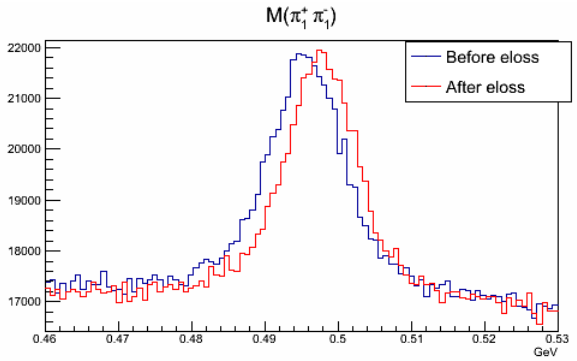

Figure 5.3: This shows the $\pi^+\pi^-$ invariant mass before and after energy loss corrections. The eloss package corrects the mass of the K_S^0 from 0.4957 GeV to 0.4977 GeV. The PDG lists the K_S^0 mass as 0.4976 GeV. Note: The axes of these spectra have been zoomed in for a better look at the shift in the $\pi^+\pi^-$ peak due to the correction. For a broader viewing scope, refer to Fig. 5.6

5.1.3 Missing Mass Cut

The missing particle in the reaction is calculated using the four-momenta of detected pions, beam and target:

$$\mathrm{P}_{missing} = (\mathrm{P}_{beam} + \mathrm{P}_{target}) - (\mathrm{P}_{\pi^+} + \mathrm{P}_{\pi^-} + \mathrm{P}_{\pi^+} + \mathrm{P}_{\pi^-}) \tag{5.8}$$

The missing particle is then ensured to be the proton by selecting those events which have the missing mass close to the mass of the proton (Fig. 5.4).

5.1.4 Beam Energy Cut

This analysis is based on the reactions given in Eqs. 5.1 and 5.2.

The threshold photon energy for the production of the $f_0(1500)$, which is the particle of main interest, can be calculated by means of the following equation:

$$E_{\gamma threshold} = \frac{m^2_{f_0(1500)} + m^2_p + 2m_{f_0(1500)}m_p - m^2_{target}}{2m_{target}} \tag{5.9}$$

where $m_{f_0(1500)}$ is the mass of the $f_0(1500)$, m_p is the mass of the proton, and m_{target} is again the mass of the proton since g12 makes use of a liquid hydrogen target. Hence,

$$E_{\gamma threshold} = \frac{m^2_{f_0(1500)} + 2m_{f_0(1500)}m_p}{2m_p} \tag{5.10}$$

From Eq. 5.10, the minimum energy to obtain an $f_0(1500)$ in this reaction is 2.7 GeV. Fig. 5.5 illustrates this with a 2-dimensional plot of the photon energy *vs* the 4π invariant mass.

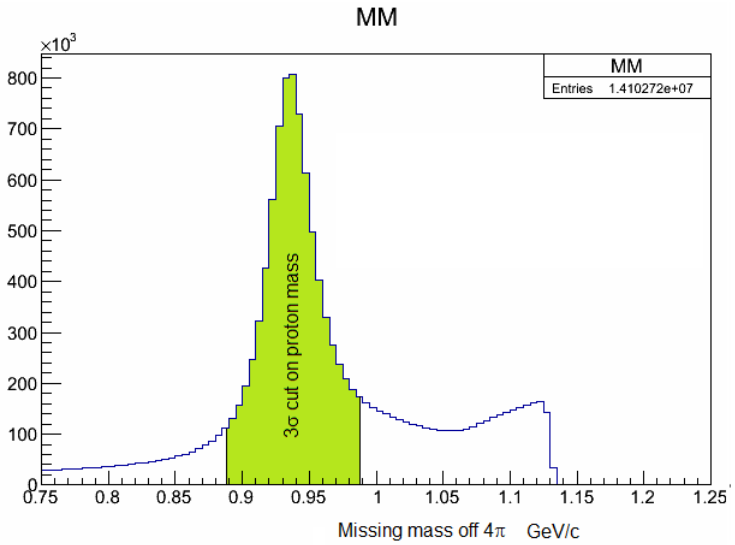

Figure 5.4: Plot of missing mass off of the four charged pions. A cut of 3σ is made around the proton mass, and only those events with the missing mass falling in this range (indicated by the green area) are retained for further analysis. Cut Level: 3

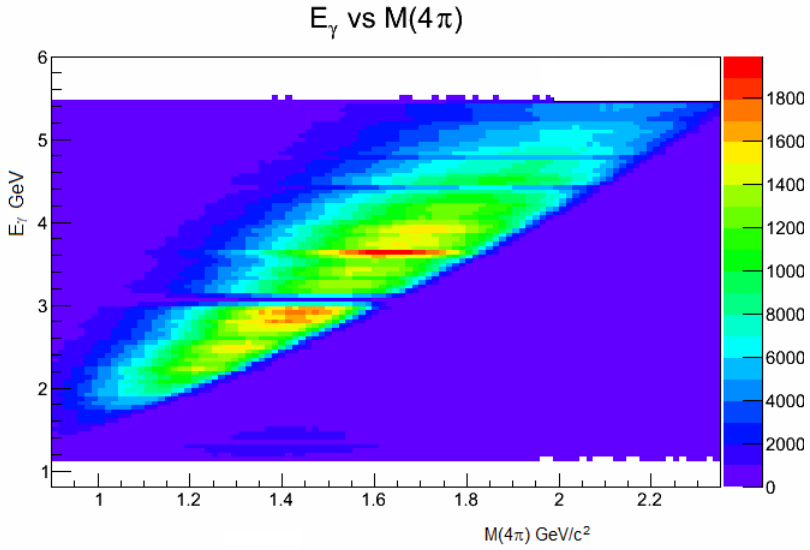

Figure 5.5: It can be seen from the plot of E_γ vs the 4π invariant mass that the threshold energy for the production of a resonance at 1.5 GeV is ~2.7GeV. The horizontal discontinuity at ~3 GeV is due to a bad timing counter in the photon tagger; this region is excluded from the analysis. The sharp increase in counts at 3.6 GeV is due to a change in the trigger configuration at that energy. Cut Level: 4

5.1.5 Sideband Subtraction

The four pions, $\pi_1^+, \pi_1^-, \pi_2^+, \pi_2^-$ can form $2K_S^0$ in two ways. We use the following naming convention:

$$K1 = \pi_1^+ \pi_1^-,$$

$$K2 = \pi_2^+ \pi_2^-,$$

$$K3 = \pi_1^+ \pi_2^-,$$

$$K4 = \pi_2^+ \pi_1^-$$

In a given event, the 4 pions can either form (a) $K1$ and $K2$, or (b) $K3$ and $K4$. Fig. 5.6 shows the invariant mass spectra for each possible pair of $\pi^+\pi^-$. The numbering of the pions is sector based; for two positively charged pions, one detected in sector 2 and the other in sector 5, the sector 2 pion is numbered 1 and the sector 5 pion is numbered 2. In all the spectra in Fig. 5.6, a clear K_S peak is seen above a combinatorial background.

If the invariant masses of the pairs of pions are plotted against one another, a high correlation is observed between the two kaons indicating a common decay source for a majority of the events. Fig. 5.7 illustrates this for both cases mentioned above.

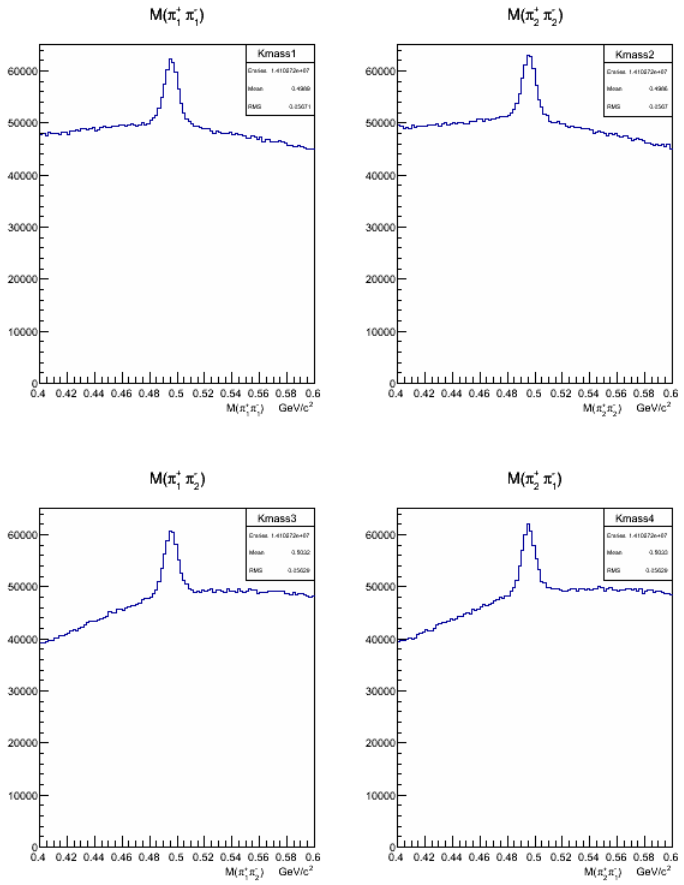

Figure 5.6: Invariant mass spectra for all combinations of $\pi^+\pi^-$. A clear K^0_S peak is seen over a combinatorial background in all the plots.

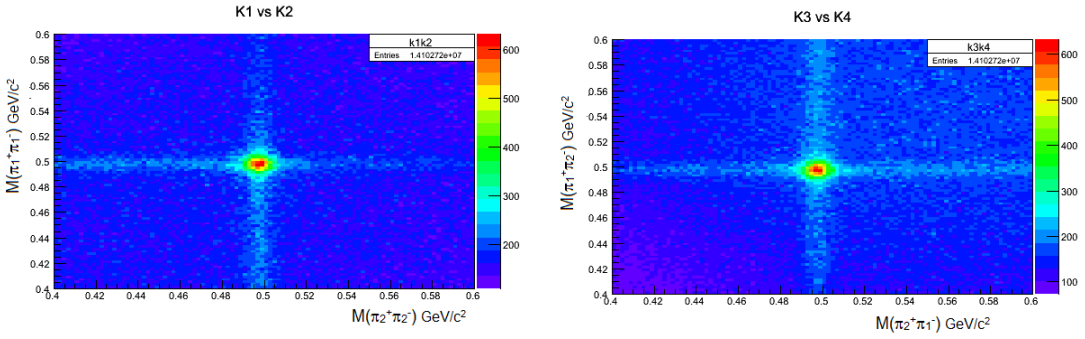

Figure 5.7: $K1 = \pi_1^+\pi_1^-$, $K2 = \pi_2^+\pi_2^-$, $K3 = \pi_1^+\pi_2^-$, $K4 = \pi_2^+\pi_1^-$. The 4 pions can either form (left)$K1$ and $K2$, or (right) $K3$ and $K4$. In both cases, the high correlation between the pair of kaons show a propensity towards a common source for a majority of the events.

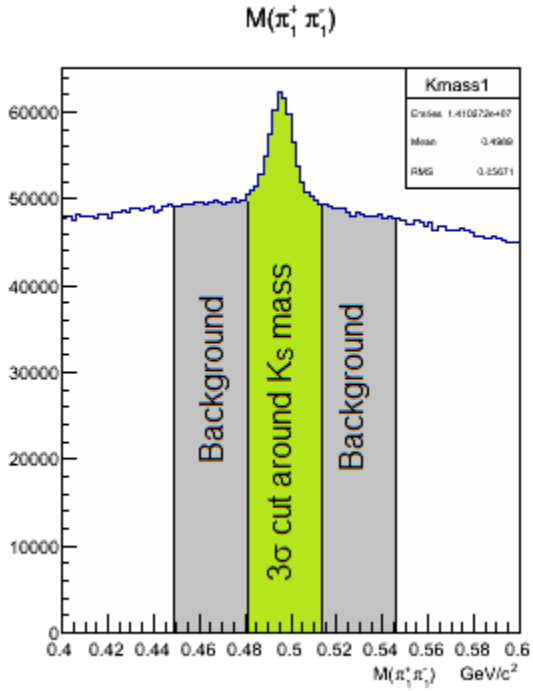

Figure 5.8: As part of the sideband subtraction method, a 3σ cut is made around the K_S mass to mark the signal region. The sidebands are the grey bands of equal width on either side of this region, and contribute to the average background below the signal.

In order to reduce background below the K_S peak, the fairly standard method of background subtraction is used. Referring to Fig. 5.8, which is a plot of the invariant mass spectrum of $\pi_1^+\pi_1^-$, the green region at the center includes the K_S signal, along with background underneath the peak. A 3σ cut is applied around the K_S mass to pick out the events lying in this region. Since the background is relatively flat, the grey bands on either side of the signal can be considered to be the average background below the K_S peak. These are of the same width as the signal region and are called 'sidebands'.

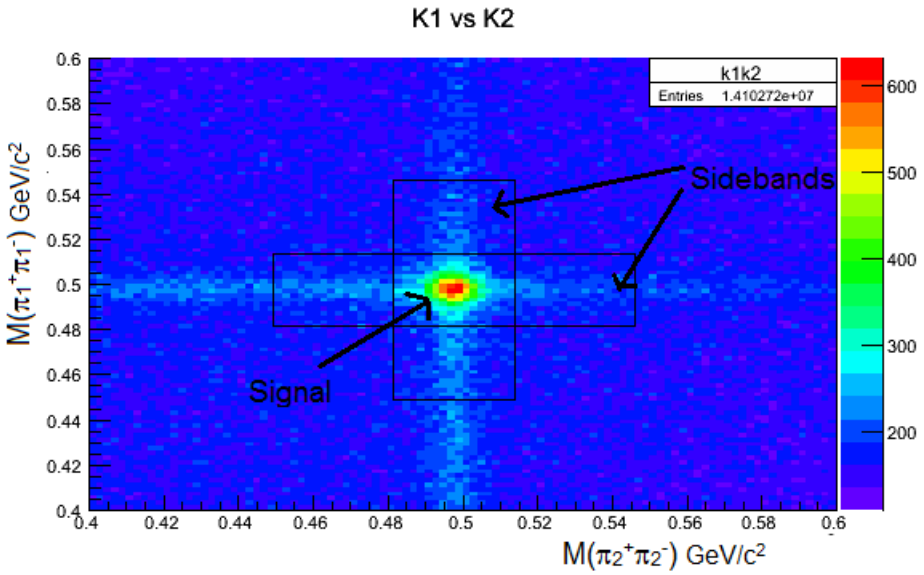

Figure 5.9: Referencing Fig. 5.8, we choose those regions as the background for which the invariant mass of one pion pair lies in the signal region and the other pair in the sideband region. The area in which masses of both pion pairs are within the signal region is taken to the signal. In the above figure, the outward four squares are the background and the middle square is the signal. Cut Level: 5

Looking at the 2-dimensional plot , Fig. 5.9, of the invariant masses of a pair of pions versus the other, there are four sidebands to consider. Each sideband region includes that region in which one pair of pions lies within the 1-D sideband, while the other pair lies within the 1-D signal. This is done so that in addition to the general 4π background, we can get rid of those events which have unrelated kaons. That region for which the masses

of both the pairs of pions lie within their respective 1-D signal bands, is taken to be the signal. Thus, for each case, $(K1, K2)$, or $(K3, K4)$, there are four sidebands and one signal region.

The average of the four sidebands is taken and subtracted from the signal to give the background subtracted signal.

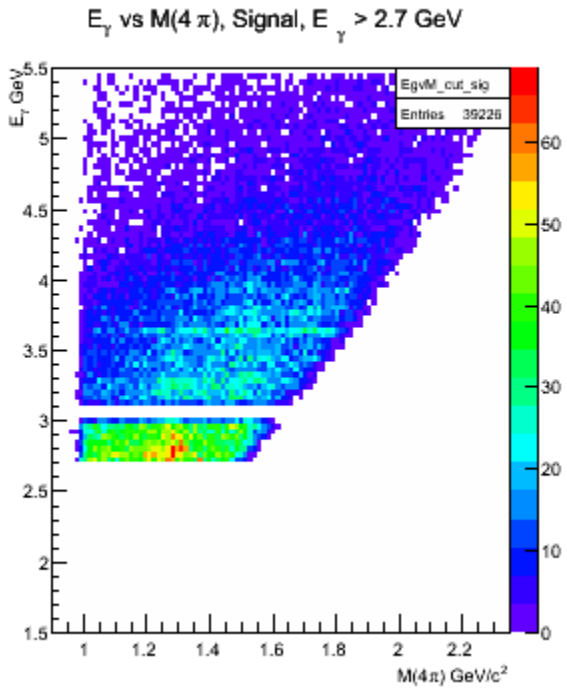

Figure 5.10: The beam energy vs. the 4π invariant mass spectrum after all the basic cuts.

5.2 Invariant Mass Spectra After the Basic Cuts

After all the cuts discussed in the previous section have been applied, the plot for the beam energy *vs* the 4π invariant mass is represented by Fig. 5.10,

Fig. 5.11 shows the 4π invariant mass spectrum before and after background subtraction. Two definite peaks, one at ~1.28 GeV and another at 1.5 GeV are seen.

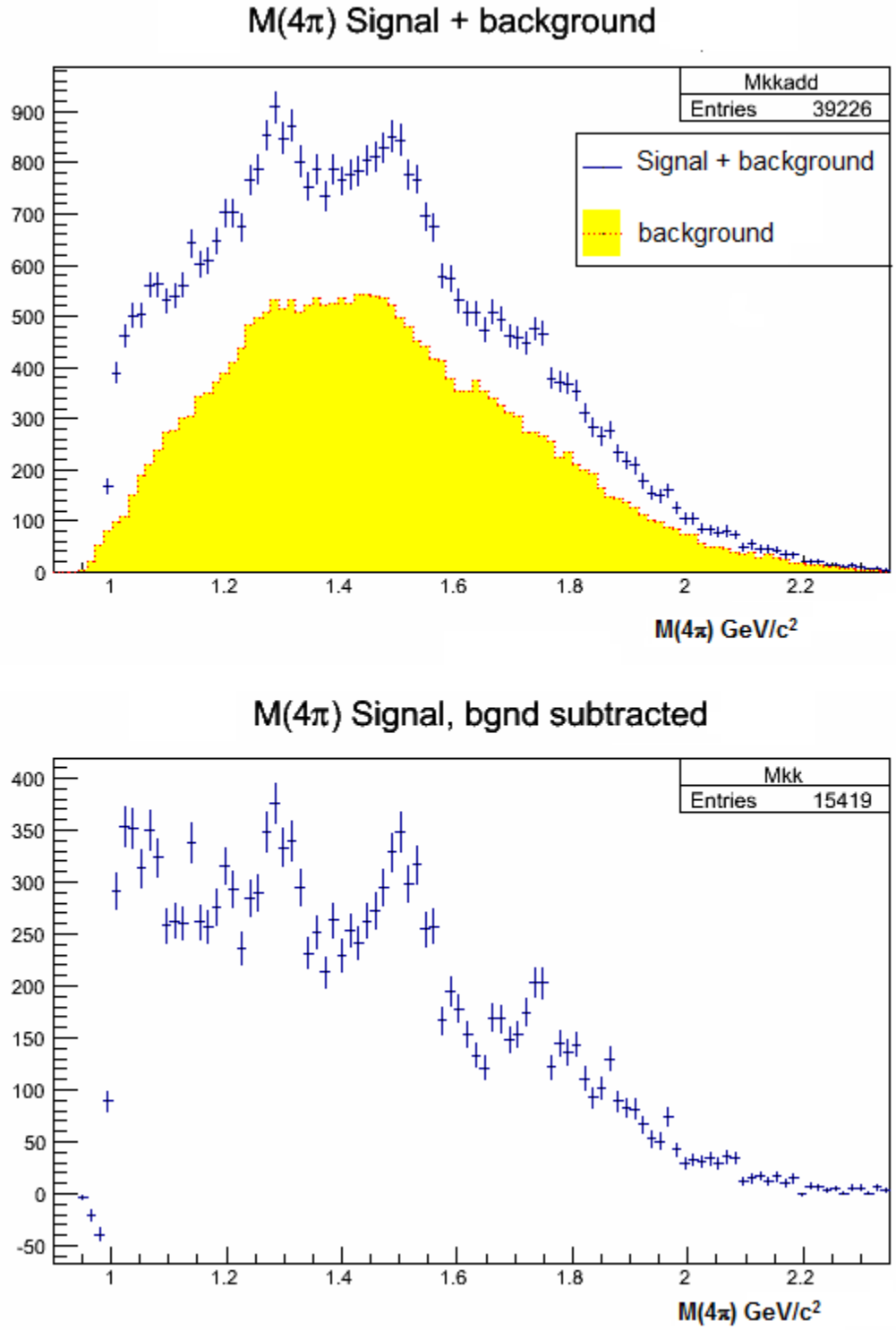

Figure 5.11: The blue histogram with the error bars shows the signal + background, whereas the yellow filled histogram is the average background. The bottom plot is the background subtracted histogram. At least two peaks can be identified, one around 1.28 GeV and another at 1.5 GeV.

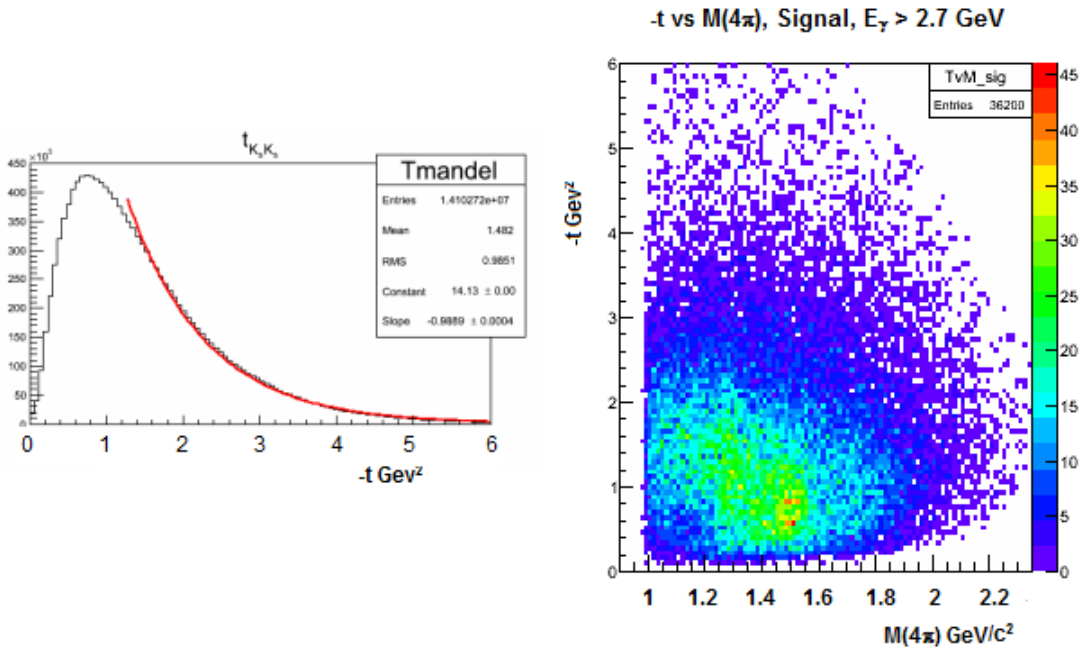

Figure 5.12: The left plot shows the negative of the Mandelstam variable 't' for the $K_S^0K_S^0$ system. When this variable is plotted against the 4π invariant mass (right), it can be seen that most of the events for the 1.5 GeV resonance are below $-t = 1$ GeV^2.

5.3 Momentum Transfer Cut

In the invariant mass spectrum in Fig. 5.11 the resonance of interest is the one at 1.5 GeV. In order to further investigate it, cuts of momentum transfer are applied. Momentum transfer between the beam and the f_0 resonance is denoted by the Mandelstam variable t:

$$t = (P_{beam} - P_{K_S^0K_S^0})^2 \tag{5.11}$$

A plot of t vs. the 4π invariant mass (Fig. 5.12 , right) shows a forward angle dependance for the 1.5 GeV resonance. For $-t < 1$ GeV^2, the 1.5 GeV resonance is enhanced in the spectrum (Fig.5.13, top), whereas it disappears for $-t > 1$ GeV^2 (Fig. 5.13, bottom). This is consistent with a meson exchange process.

5.4 Dalitz Plots to Look for Baryon Resonances in Background

To look for any possible resonances due to combination of K_S and p, Dalitz plots are of K_SK_S vs. K_Sp , and K_Sp vs. K_Sp are plotted in Figs. 5.14 and 5.15. These plots are after application of cuts 1-5 from Table 5.1, as well as the momentum transfer cut, and hence these are the events remaining in the signal region after background subtraction has been done. For the K_SK_S vs. K_Sp plot (Fig. 5.14), the only resonances to be seen are the ones on the vertical axes, for the $K_SK_S$combination. Similarly, in Fig. 5.15, the diagonal lines indicate that there is no structure in the K_Sp combination. Both these Dalitz plots indicate there is virtually no baryon background in the signal region.

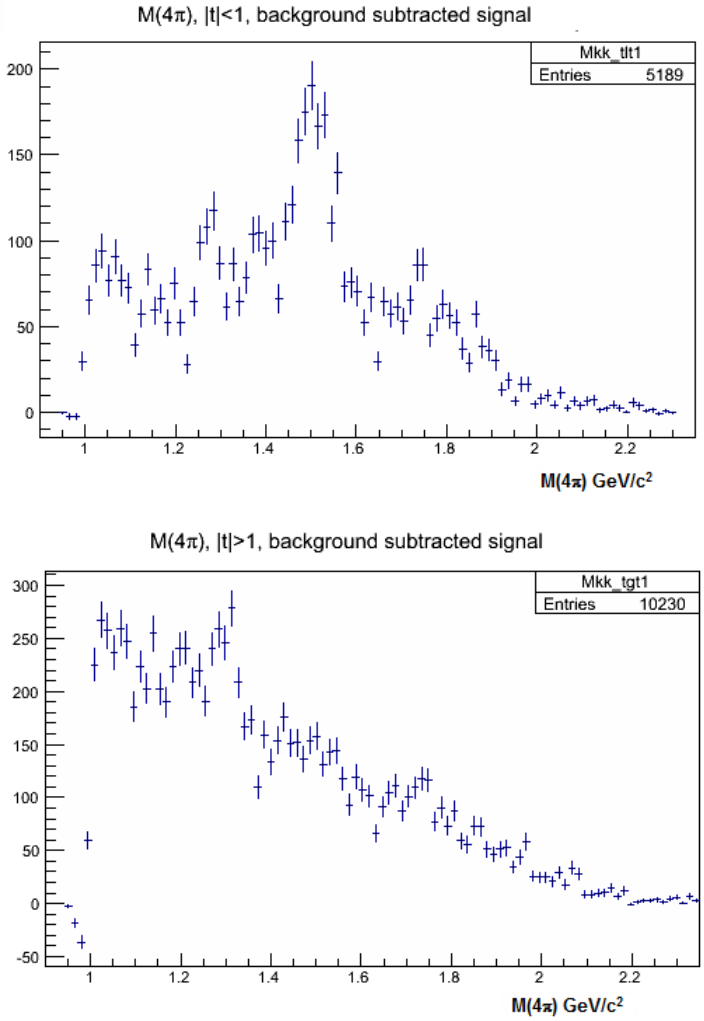

Figure 5.13: Background subtracted plots for the 4π invariant mass for (left) $-t < 1$ GeV^2, (right) $-t > 1$ GeV^2. The 1.5 GeV peak is enhanced for $-t < 1$ GeV^2, whereas it disappears for $-t > 1$ GeV^2.

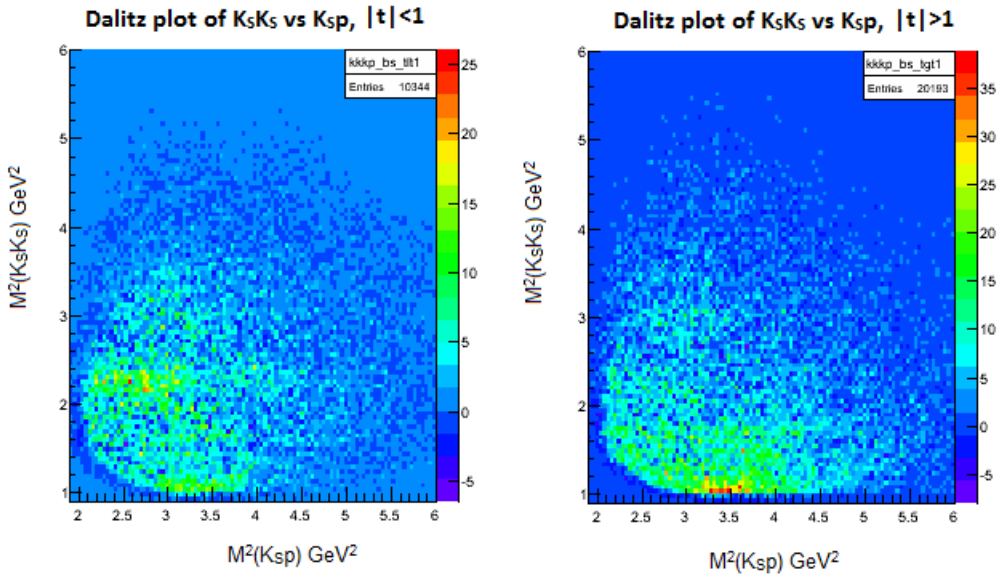

Figure 5.14: Dalitz plots of the three decay particles, the two kaons and the proton.

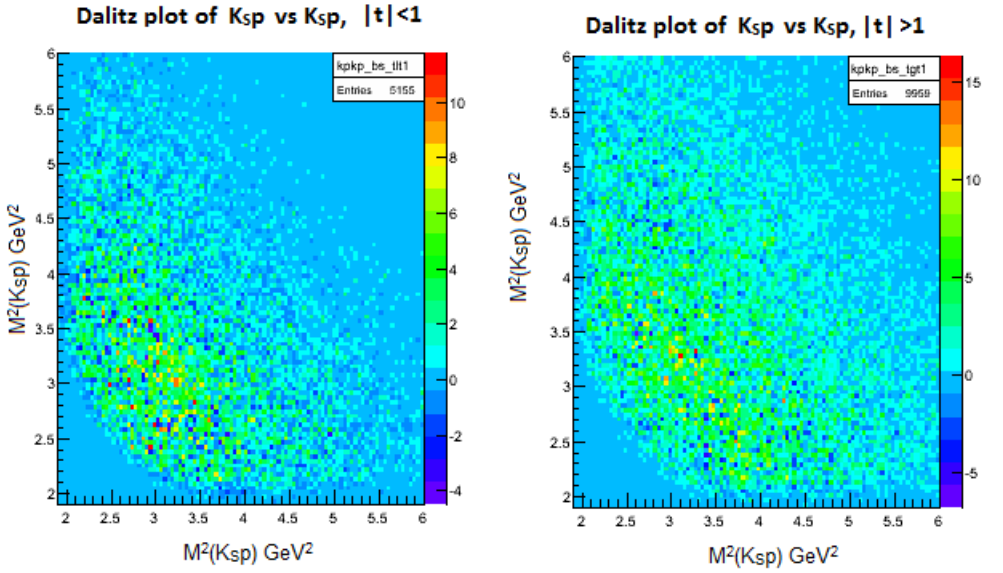

Figure 5.15: Dalitz plots of the three decay particles, Left: $-t < 1$ GeV^2, Right: $-t > 1$ GeV^2

6 SIMULATIONS

In order to do a moments analysis, it is necessary to have a proper understanding of the acceptance of the CLAS detector. Not all of the events generated by the interaction of the target and photon beam are 'seen' by CLAS, and hence, a knowledge of whether the observed spectra are due to physics or due to visibility to the detector is crucial for their interpretation. If we know the effect on the detector on uniform 4π phase space, we can use this information to normalize the data .

6.1 Modeling the CLAS Detector

In order to study the acceptance of CLAS, a sample of $\gamma p \to K^0_S K^0_S p$, with $K^0_S K^0_S \to \pi^+\pi^-\pi^+\pi^-$,was generated using the event generator FSGEN (Full Spectrum Generator). The sample events were generated isotropically with no dependance on t. The incident electron energy was set at 5.7 which translated into bremsstrahlung photon beam energies of 1.5 GeV to 5.45 GeV. As in the g12 experiment, the simulated target was 40 cm in length, with its z-position from -110 cm to -70 cm. These generated events are called *'raw monte-carlo*'. A large enough sample was generated so as to reduce its effect on systematic uncertainties.

These *raw* events were then fed through CLAS software called GSIM (Geant SIMulation). GSIM utilizes CERN Geant libraries to mimic the geometry of every CLAS detector sub-system, so that this simulated model passes the generated events through it in the same manner that CLAS would for real data. After being processed through GSIM, the set of events are passed through another software program called (GSIM post processor), which compares the condition of the CLAS detector to that during the g12 experimental run period. In response to a set of parameters denoting this condition, it removes hits that come from non-functioning parts of the detector and smear values of measurements depending on the resolution of the corresponding detector element during the g12 run period. These

twice processed events are then fed into reconstruction software called $a1c$.

Reconstruction is carried out independently in each sector. Beginning with the region one of the drift chamber, hits in adjoining layers form clusters, which, when combined with hits in the other regions of the DC, provide a "hit-based" track. The charge and momentum of the particle is deduced from the sign and magnitude of the curvature of the particle-track. Not all tracks formed in this way are physical and include noise. To eliminate this, the DC track is extrapolated to the TOF counter panels. If the corresponding TOF panel has also recorded a hit, then the TOF time for the track is the upper limit for the DC track. Making use of this, the superfluous hits in the DC are discarded. Up to two more iterations of this process are carried out in order to fine-tune the measurements. This is called "time-based" tracking.

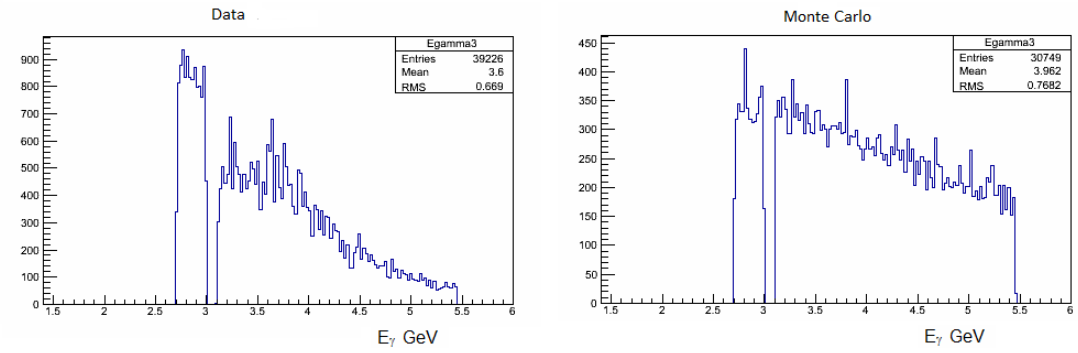

Figure 6.1: A comparison of the beam bremsstrahlung spectra for data and simulation after all cuts. The bad tagger counter at 3.0 GeV was not reconstructed in the Monte Carlo and hence was removed in the analysis.

Once this initial set of iterations is done, the track is extrapolated to the other CLAS sub-systems: the start counter, the Cerenkov detector and the electromagnetic calorimeter. If hits in these systems are found in the parallel regions, then this information is added to the track to get a complete picture of the type of particle and its characteristics. These set of algorithms are then coded with C and FORTRAN to create the reconstruction software .

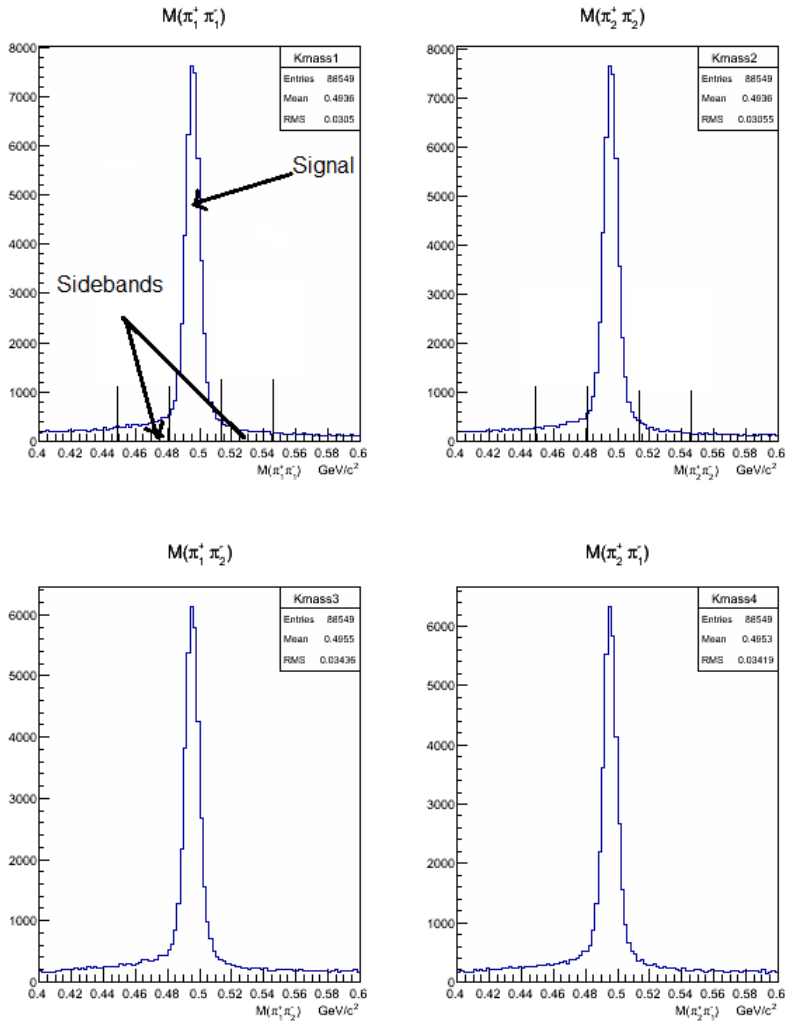

Figure 6.2: The invariant mass spectra for all combinations of $\pi^+\pi^-$. The K_S peak stands out with very little background.

6.2 Checking Against Data

To analyze the acceptance of CLAS, phase space for $\gamma p \to K_S K_S p$ was simulated. In addition, a separate simulation was carried out for $\gamma p \to f_0(1500)$, which could then be added to the phase space Monte Carlo (MC). The monte carlo events that pass GSIM, and are fed through the same analysis code as real data. The events remaining after this are called *accepted* events.

The beam energy after all cuts outlined in 5.1 has a shape denoted by the left plot on Fig. 6.1. The corresponding beam energy spectrum for monte Carlo (MC) is shown on the right of the same figure. The difference in the spectral shape is likely due to the fact that the MC was generated isotropically with no dependance on *t*.

As in the case of real data, the invariant masses for all the different combinations of $\pi^+\pi^-$are plotted in Fig. 6.2. The K_S signal is strong in all cases with presence of very little background.

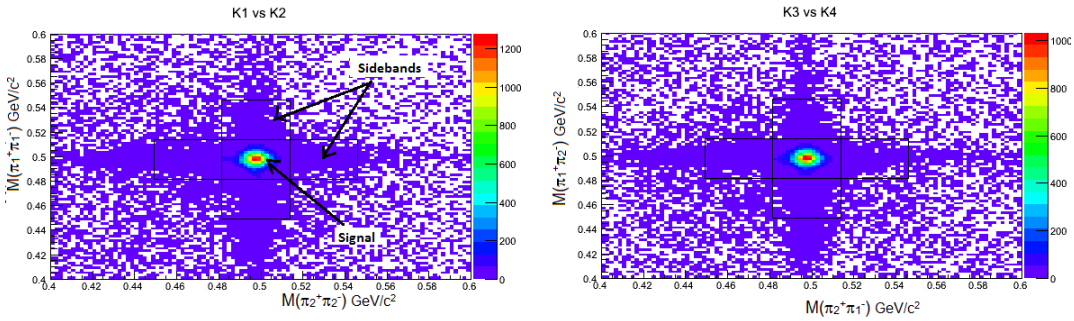

Figure 6.3: The 2-D plots for a pair of $\pi^+\pi^-$ versus the other. Most of the events are concentrated in the region where at least one K_S is formed, as expected from the 1-D plots.

Fig. 6.3 showcases the 2-dimensional plots for the 2 possible pair-combinations of $\pi^+\pi^-$. Most of the events are concentrated in the region where at least one $\pi^+\pi^-$pair forms a K_S. The sideband and signal regions are chosen in the same way as for the data.

The missing mass off of the 4-pions is shown in Fig. 6.4. A 3σ cut is applied around the proton mass, as in the data.

6.2.1 Phase Space Monte Carlo

First, we look at how the phase space MC plots compare against the data before moving on to the MC with the $f_0(1500)$ added to the phase space.

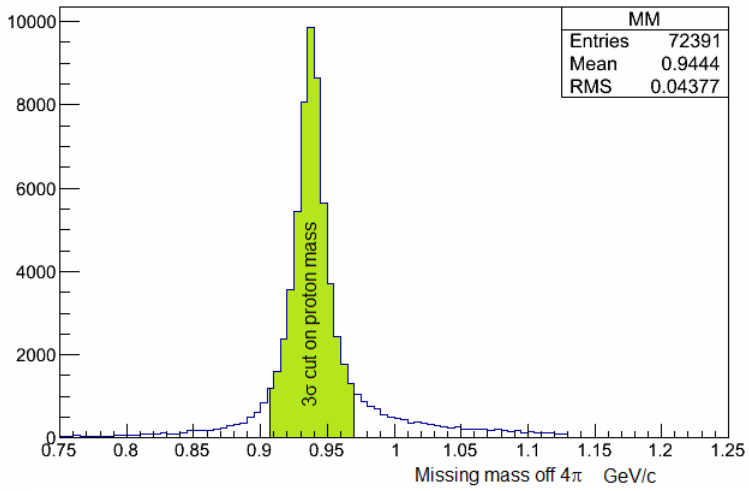

Figure 6.4: The missing mass off of the 4 pions. The same cut is used here as was used for real data.

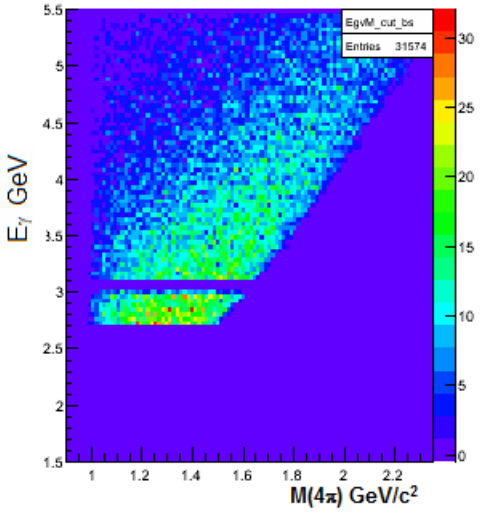

Figure 6.5: For phase space Monte carlo, the beam energy *vs* the 4π invariant mass.

Fig. 6.6 shows the 4π invariant mass plots after all cuts have been applied. Very little background in present. as indicated by the yellow histogram in the top plot. The bottom plot in the same figure shows the background subtracted 4π invariant mass spectrum. Apart from statistical fluctuations, this spectrum has no structure, as should be the case for a phase space Monte Carlo.

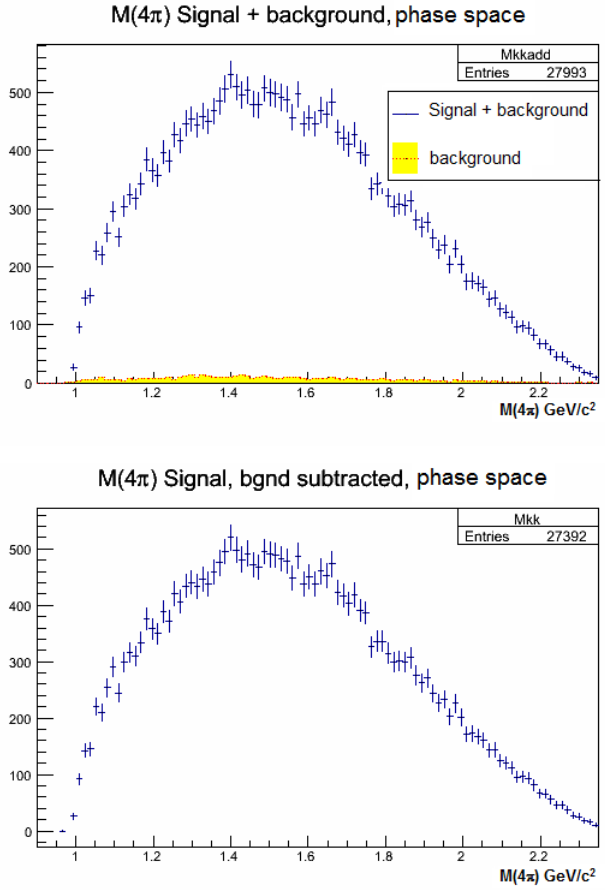

Figure 6.6: In the top plot, the blue histogram is the region which contains the signal plus the background. As expected, the yellow region, which represents the background makes only a small contribution to the histogram. The bottom plot shows the background subtracted 4π invariant mass spectrum. The bump at 1.4 GeV cannot be caused by physics, neither can it be caused by kinematic constraints, and hence is likely statistical fluctuation.

The t variable is plotted on the left of Fig. 6.7. The slope after fitting an exponential function to this curve is -0.815. A plot of t *vs* the 4π invariant mass, shown on the right of Fig. 6.7, unsurprisingly indicates no structure. This is demonstrated in Fig. 6.8 which shows the 4π invariant mass spectra after cuts on t. Apart from the shape imparted by the momentum transfer, there are no additional peaks in the spectra.

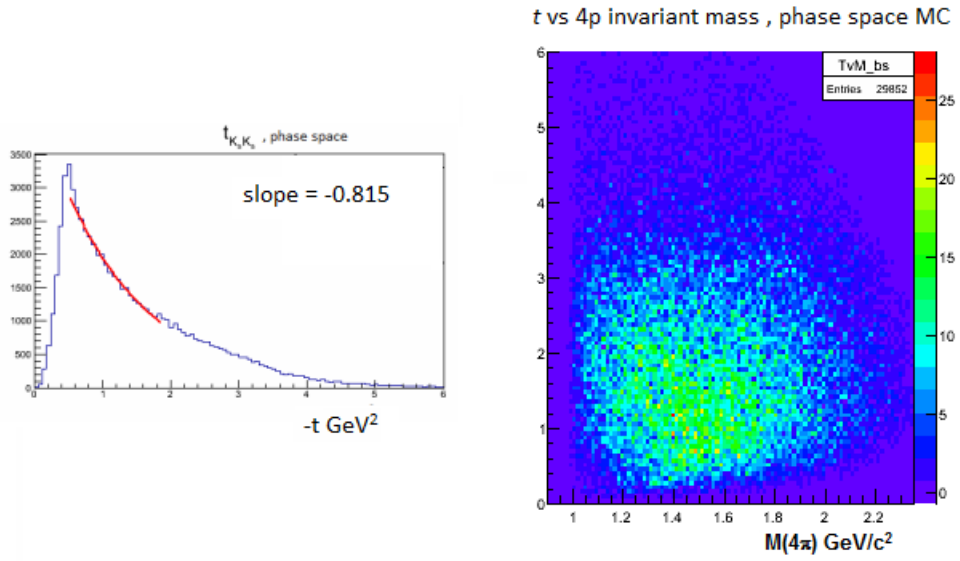

Figure 6.7: The slope of the phase space$t$ distribution (Left plot), which is calculated by fitting an exponential (the red line) to the curve, for isotropically generated events, comes out to be -0.815. When the t-variable is plotted against the 4π invariant mass (Right plot), no structure is seen, since this is phase space.

6.2.2 Monte Carlo with Phase Space, Plus $f_0(1500)$

After adding the generated $f_0(1500)$ to the phase space MC, the plot for beam energy *vs* the 4π invariant mass now shows a definite spike at 1.5 GeV on the horizontal axis, Fig. 6.9. When the 4π invariant mass spectrum is plotted in Fig. 6.10, the $f_0(1500)$ makes its presence known by the peak at 1.5 GeV. This is also seen in the plot of t *vs* the 4π invariant mass, Fig. 6.11(right).

If cuts are made to divide the 4π invariant mass spectrum into two sets, one with $|t| < 1GeV^2$ and the other with $|t| > 1GeV^2$ (Fig. 6.12), then the peak at 1.5 GeV is present in a larger extent for $|t| > 1GeV^2$ than for $|t| < 1GeV^2$. The increased number of counts of the 1.5 GeV peak in the $|t| > 1$ plot is expected because kinematically, a high momentum transfer would increase the probability of formation of the simulated f_0 if there was no other physical process to change this dynamics. This is reiterated in the Dalitz plots shown in Fig. 6.13. For real data, the peak at 1.5 GeV is present for $|t| < 1GeV^2$, but not for

$|t| > 1GeV^2$. By comparison with MC, we see that the physical process associated with the production of the $f_0(1500)$ is t-channel photo-production.

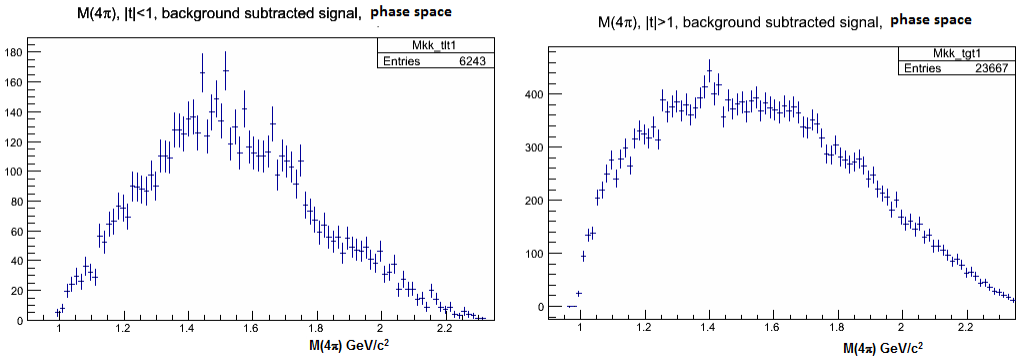

Figure 6.8: A comparison of the 4π invariant mass background subtracted spectra for $|t| < 1\text{GeV}^2$(Left) and $|t| > 1\text{GeV}^2$(Right). The only structure is that imparted due to kinematic constraints. The bump at 1.4 GeV is the one seen in Fig. 6.6.

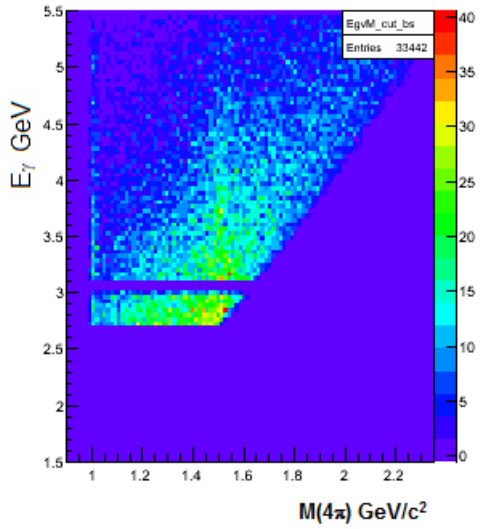

Figure 6.9: Beam energy *vs* the 4π invariant mass for phase space MC with the addition of the $f_0(1500)$. The spike at 1.5 GeV on the horizontal axis shows the presence of the $f_0(1500)$.

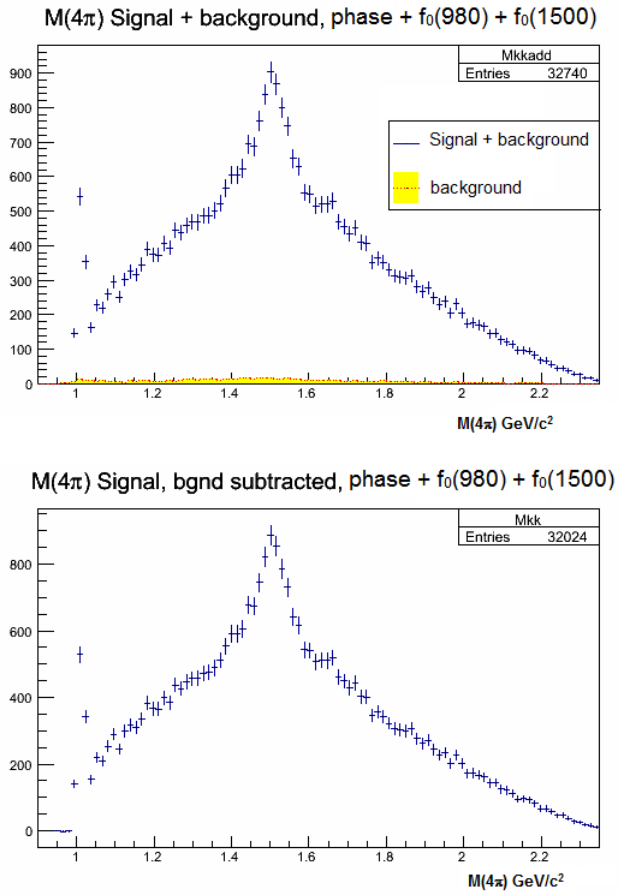

Figure 6.10: 4π invariant mass background subtracted signal for generated phase space + generated $f_0(1500)$. Since the $f_0(1500)$ was added on top of phase space while generating the Monte carlo events, the 4π invariant mass spectrum has the prominent peak at 1.5 GeV on top of the same general shape as the spectrum in Fig. 6.6.

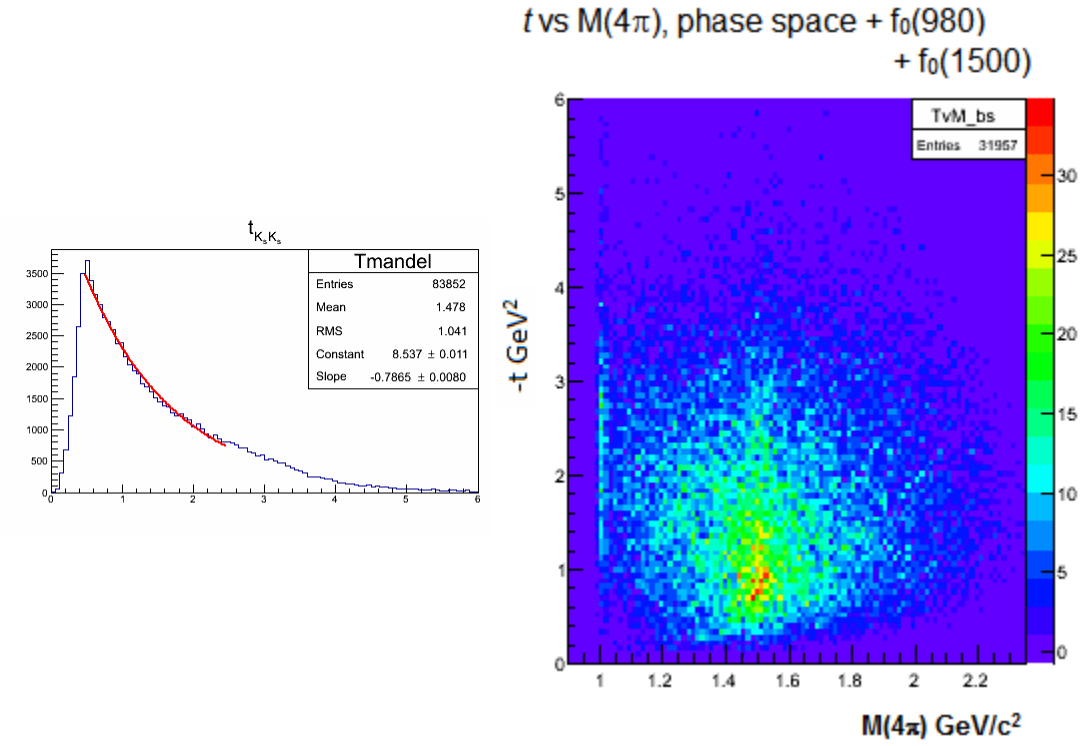

Figure 6.11: **Left:** t- distribution of generated phase space + generated $f_0(1500)$. The slope of the t plot is similar to that for just phase space since these are still isotropic events. **Right**: 4πinvariant mass v/s $-t$ for generated phase space + generated $f_0(1500)$. The line at 1.5 GeV on the horizontal axis shooting up denotes the presence of the $f_0(1500)$ in the MC sample.

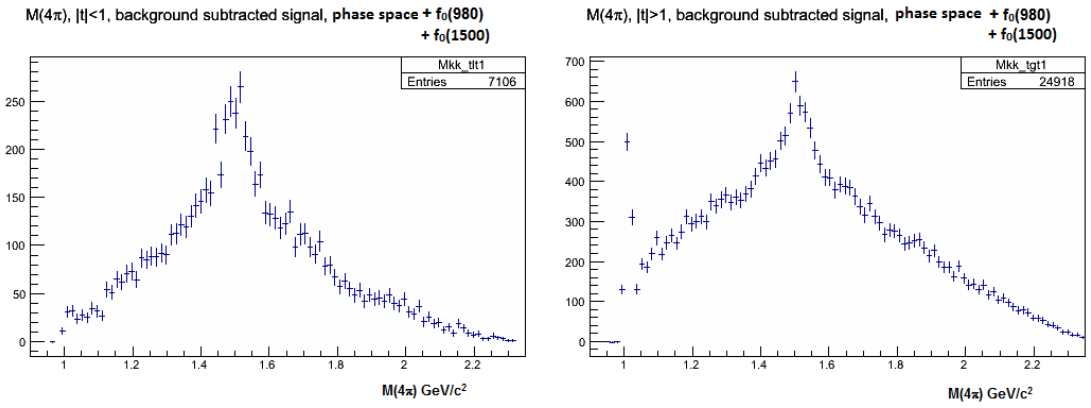

Figure 6.12: 4π invariant mass background subtracted spectrum for phase space + $f_0(1500)$ with momentum transfer cuts $|t| < 1GeV^2$(Left) and $|t| > 1GeV^2$(Right) . The peak at 1.5 GeV shows almost double the counts in the $|t| > 1GeV^2$ plot as compared to the $|t| < 1GeV^2$ plot.

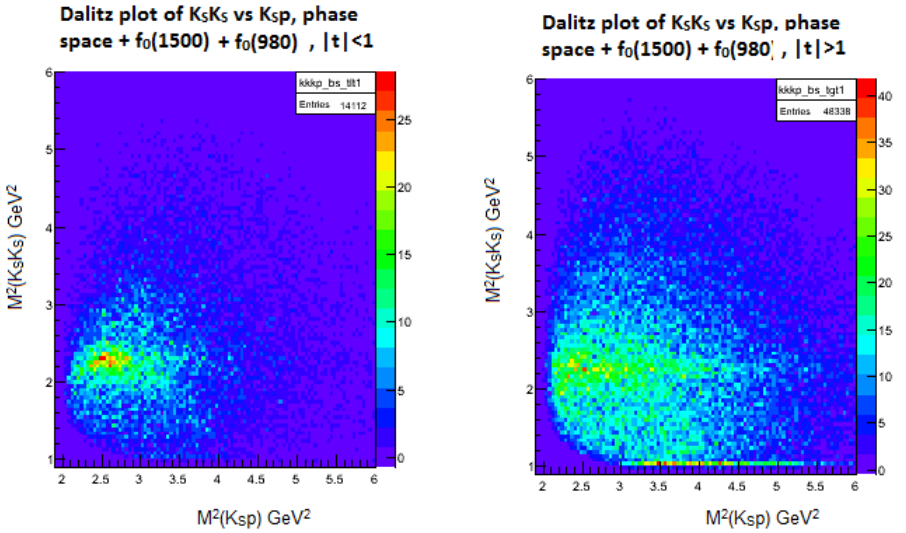

Figure 6.13: The Dalitz plots of K_SK_S vs K_Sp for $|t| < 1GeV^2$(Left) and for $|t| > 1GeV^2$ (Right) for generated phase space + generated $f_0(1500)$. The increased number of counts of the 1.5 GeV peak in the $|t| > 1$ plot is expected because kinematically, a high momentum transfer would increase the probability of formation of the simulated f_0 if there was no other physical process to change this dynamics.

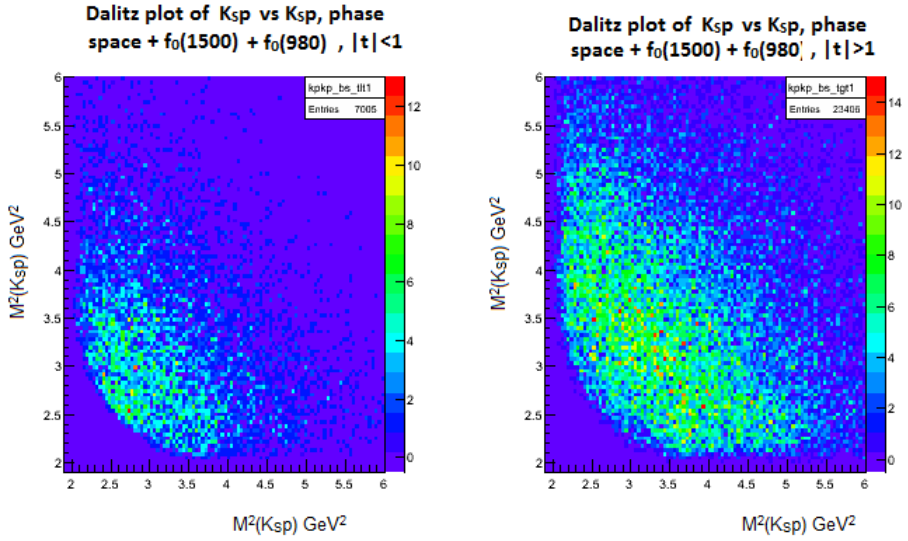

Figure 6.14: The Dalitz plots of K_Sp vs K_Sp for $|t| < 1GeV^2$(Left) and $|t| > 1GeV^2$(Right) for generated phase space + generated $f_0(1500)$. There are no K_Sp resonances observed in either plot, as anticipated.

7 FORMALISM FOR MOMENTS ANALYSIS

In the analysis of the invariant mass spectrum of final state particles in a scattering experiment, an enhancement or peak in the spectrum is one of the indicators of the presence of a resonance. The mass and width of such a peak can be estimated using fitting procedures. However, in order to get a complete picture, we need to determine the spin-parity quantum numbers of the resonances. A 'peak' may contain contributions from several different spin-parity configurations; we call these partial waves. Partial wave analysis is a method to extract the degree of contribution of different waves from a particular intensity distribution. By examining the angular distribution of the secondary decay particles, we can derive the moments $\langle Y_{LM} \rangle$ of the resonance in question and use these to look for interferences from different partial waves.

7.1 Introduction

The study of the properties of particles usually begins with a scattering experiment. In the g12 experiment, as was described in the previous chapter, a photon is scattered off of a proton target. Every interaction between the photon and proton produces particles through different processes. We then need to choose those events which produce the final particles of interest in our investigation. The probability of occurrence of a particular reaction is related to the cross-section of that reaction. In general, the cross section is given by:

$$\sigma = \frac{N_{obs\ events}}{N_{\gamma Flux}\, \rho_{target}\, L_{target}\, N_A\, \eta} \tag{7.1}$$

Here. N_γ =total number of photons incident on the target,

ρ_{target} =density of the target,

L_{target} =length of the target,

N_A =Avogadro's number

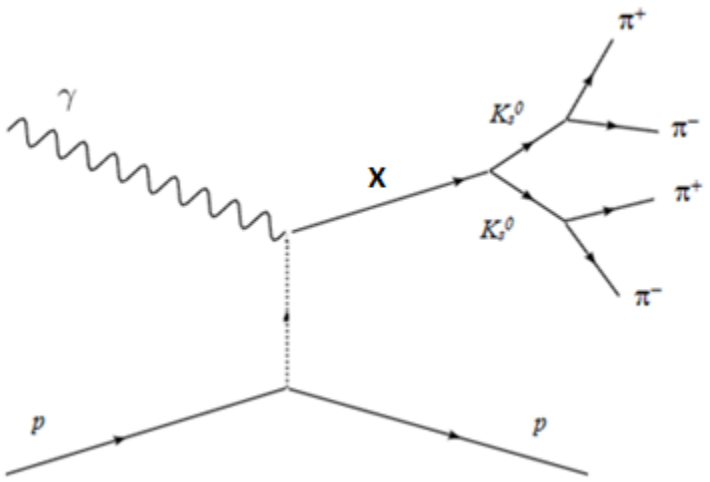

Figure 7.1: The diagram representing the reaction. The photon interacts with the proton, and produces a resonance X, with the proton as the recoil particle. The resonance X then decays into 2 K-shorts. Each K_S further decays into two charged pions.

η =detector acceptance

The quantity above is the total cross-section integrated over all angles and momenta. A better picture would be obtained if we were to calculate the *differential cross-section*, or, the cross-section per unit of phase space (*e.g.* per unit of solid angle or per unit momentum transfer). Consider the figure 7.1. This is a sequential decay (Eq. 7.2),

$$\gamma + p \rightarrow X + p, \quad X \rightarrow K_S^0 K_S^0, \quad K_S^0 \rightarrow \pi^+ \pi^- \tag{7.2}$$

and while evaluating the reaction we make use of the *isobar model*. The approach of this is to think of every subsequent decay as a two-body decay. Every decaying node is completely factored out from the recoiling particle[6]. Even if the recoiling particle decays further, we now will consider the initial particle we picked out to evaluate, while making use of the properties of the recoiling particle for energy, momentum and spin conservation. In our decay channel, we want to analyze the properties of X and hence we will consider its decay into the two K_S^0s . Then, we choose any one K_S^0 and consider its decay into two charged

pions.

The quantum numbers required to describe this reaction are:

- J, the total spin of X
- M, the spin projection of J along the Z axis in the rest frame of X
- P, the parity of X
- L, the angular momentum between the two kaons
- s, the spin of X
- I, the isospin of X

Now that we have a model, the choice of frames of reference depends on which basis we will describe the reaction with. The spin-orbital basis is not useful when we are dealing with several decays. This is because of the way that these quantities are defined; the orbital angular momentum is defined in the center of mass frame of two interacting particles, whereas the spin angular momentum is defined in the rest frame of an individual particle. This leads to complications while expressing the states, which we can avoid by using the helicity formalism [3]. Helicity is the spin projection in the direction of motion, whose operator is defined by $\hat{h} = \hat{S} \cdot \hat{p}$. It is invariant under rotations since the quantization axis is itself rotated to coincide with the direction of momentum. At the same time, it is also invariant under Lorentz boosts along the direction of momentum [1], and hence is a good choice to describe our model. The following discussion is based on the exposition in Ref. [4].

The first reaction in Eq. 7.2 is

$$\gamma + p \to X + p \tag{7.3}$$

In the Center of Mass (CM) frame of the photon and proton, this is a two body scattering process, and the phase-space element is proportional to the scattering angle θ_X^{CM} of X :

$$d\rho_0 \propto d\theta_X^{CM} \tag{7.4}$$

For the next process in the reaction,

$$X \to K_S^0 K_S^0 \tag{7.5}$$

we can choose either the Gottfried Jackson (GJ) frame or the helicity frame. For the resonance X, the helicity and GJ frames differ only in the orientation of the $\hat{z}$ axis. For reasons explained in Chapter 8, we choose the GJ frame. First, the system is boosted to the rest frame of the resonance X and the axes are chosen in the following way: the $\hat{z}$-axis is aligned in the direction of the photon, the $\hat{y}$-axis is perpendicular to the production plane, $\hat{y} = \hat{z} \times \vec{p_{X_{CM}}}$, and the $\hat{x}$-axis is chosen according to the right handed coordinate system $\hat{x} = \hat{y} \times \hat{z}$. The reaction in Eq.(7.5) is a single-body decay into two particles and the phase-space element now takes on factors $d\theta_{K_S^0}^{GJ}$, $d\phi_{K_S^0}^{GJ}$, dm_X, and $p_{K_S^0}^{GJ}$, where $(d\theta_{K_S^0}^{GJ}, d\phi_{K_S^0}^{GJ}) = d\Omega_{K_S^0}^{GJ}$ are the polar and azimuthal angles of one of the kaons, let us call it K_{S_1} , in the GJ frame, m_X is the mass of the resonance X, and $p_{K_S^0}^{GJ}$ is the momentum of K_{S_1} in the GJ frame [1].

$$d\rho_1 \propto d\Omega_{K_S^0}^{GJ}\, dm_X\, p_{K_S^0}^{GJ} \tag{7.6}$$

The helicity and GJ frames are represented in Fig.(7.2). The next decay in the sequence, $K_{S_1} \to \pi^+\pi^-$ is a weak decay. Since parity is one of the quantities we are interested in, we will only consider the processes which conserve parity, and hence we do not include the decay vertex of the K_S in the calculation of the phase space element. We only make use of the 4 momenta of the detected pions to calculate the corresponding

4-momenta of the two kaons. Gathering the above factors, the phase space element, $d\sigma$, can be expressed as in Eq. 7.7.

$$d\sigma \propto d\theta_X^{CM}\, d\Omega_{K_S^0}^{GJ}\, dm_X\, p_{K_S^0}^{GJ} \tag{7.7}$$

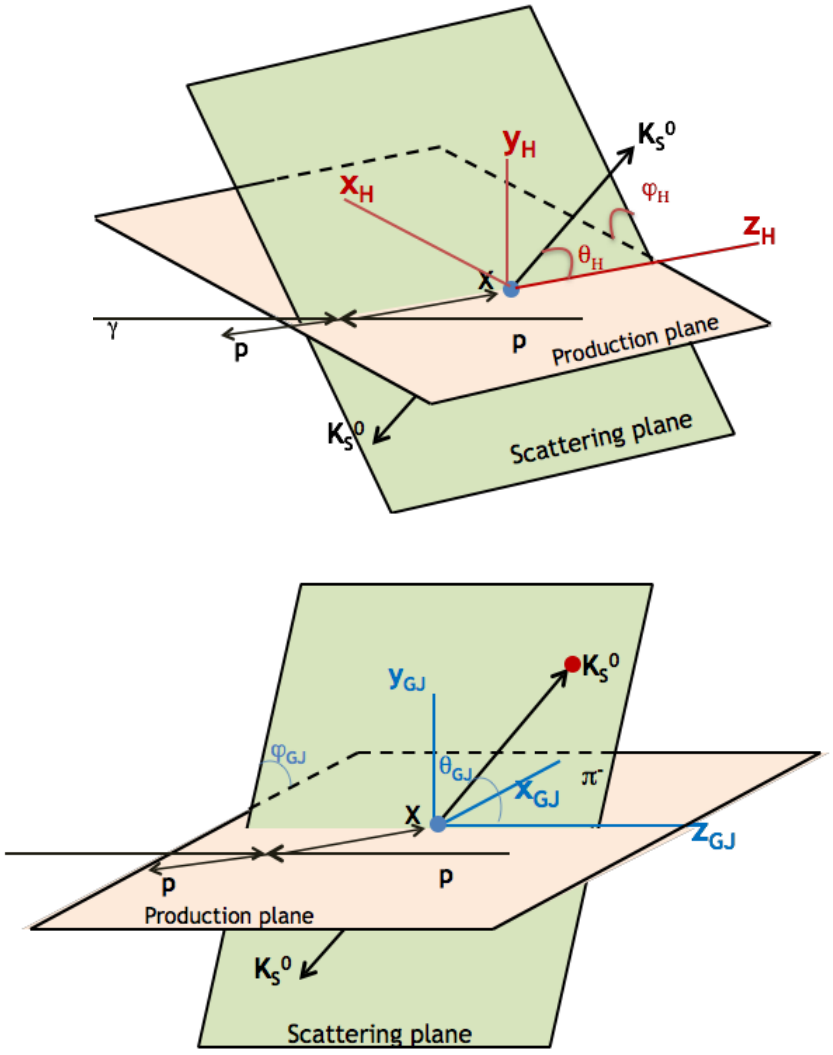

Figure 7.2: The two frames of reference. **Top:** The helicity frame. Here, the $\hat{z}$-axis is aligned along the momentum of X in the center of mass frame. **Bottom:** The Gottfried Jackson frame. Here, the $\hat{z}$-axis is aligned along the direction of the photon.

The scattering angle θ_X^{CM} can be expressed in terms of the momentum transfer t between the photon and X, and so we can write the differential cross-section as

$$\frac{d\sigma}{dt dm_X d\tau} \propto |\mathscr{M}|^2 \, p_{K_S^0}^{GJ} \tag{7.8}$$

where τ includes all the factors that are required to describe the reaction $X \to K_S^0 K_S^0$, *i.e.,* $\Omega_{K_S^0}^{GJ}$. $\mathscr{M}$ is the matrix connecting the initial state $p+\gamma$ to the final state $K_S^0 K_S^0 p$. In order to describe the experimental intensity distribution, which is directly related to the matrix term as $I(\tau) = I(\Omega_{K_S}) = |\mathscr{M}|^2$. We will need to parametrize $\mathscr{M}$ in terms of Ω_{K_S}. The dependance on the mass m_X of the resonance X, can be taken into account by binning the data into mass bins for which the intensity I can be assumed to be constant. The angular dependance of $\mathscr{M}$ is expressed by the Wigner D-functions (Eq. 7.9),

$$D^j_{m'm}(\alpha,\beta,\gamma) = e^{-im';\alpha} \, d^j_{m'm}(\beta) \, e^{-im\gamma} \tag{7.9}$$

where $d^j_{m'm}(\beta)$ is given by Eq. 7.10.

$$d^j_{m'm}(\beta) = \sum_k (-1)^{k-m+m'} \frac{\sqrt{(j+m)!(j-m)!(j+m')!(j-m')!}}{(j+m-k)!k!(j-k-m')!(k-m+m')!} \\ (\cos\frac{\beta}{2})^{2j-2k+m-m'} (\sin\frac{\beta}{2})^{2k-m+m'} \tag{7.10}$$

7.2 Parity Conservation and Reflectivity

Now we have to think about choosing proper basis states to best describe the whole reaction, in order to extract the variables that we are interested in. For moments analysis, we want to be able to have access to the spin, parity, isospin and G-parity of the particles. Hence, we need to choose a basis which conserves these quantum numbers. However,

helicity is not an eigenstate of parity. This can be understood as follows: In the rest frame of a massive particle with spin J, the helicity λ is the same as the spin-projection M and can take values $-J,-J+1,....J-1,J$. For a massless particle, like the photon, the helicity can only take two values, $\pm J$. In the frame where this particle has momentum $\vec{p}$, M is no longer defined, but the helicity still has the same values as before and we can write the state as $|\vec{p},J\lambda\rangle$. Suppose the parity operator now acts on this state. The momentum reverses its direction, but the angular momentum remains unchanged. Hence, the helicity will now have a value of $-\lambda$. Due to this, we cannot use the helicity basis to represent our data, but we can construct linear combinations of states with opposite helicities such that the new state is now an eigenstate of parity. In the GJ frame, the parity operation causes a reflection in the $\hat{x}-\hat{z}$ plane and hence commutes with the a rotation about the $\hat{y}$-axis. To construct our new basis, we need to have states with the same momentum, spin and parity, a detailed explanation of this can be found in Ref. [145, 146, 148].

$$\hat{\mathsf{P}}\,|\vec{p},J\lambda\rangle = P(-1)^{J-\lambda}e^{i\pi J_y}\,|\vec{p},J-\lambda\rangle \tag{7.11}$$

$$\hat{\mathsf{P}}e^{-i\pi J_y}\,|\vec{p},J\lambda\rangle = P(-1)^{J-\lambda}\,|\vec{p},J-\lambda\rangle \tag{7.12}$$

The reflection operation $\hat{\mathsf{P}}_y = \hat{\mathsf{P}}e^{-i\pi J_y}$ has the effect of rotating a state about the $\hat{y}$-axis in the Gottfried Jackson frame followed by the parity operation. The new eigenstates in the rest frame of a particle can be written as:[2]

$$|\varepsilon JM\rangle = [|PJM\rangle + \varepsilon P(-1)^{J-M}\,|PJ-M\rangle]\Theta(M) \tag{7.13}$$

$$\text{where } \Theta(M) = \begin{cases} \frac{1}{\sqrt{2}} & for\, M > 0 \\ \frac{1}{2} & for\, M = 0 \\ 0 & for\, M < 0 \end{cases}$$

where we now have a new quantum number, ε, called the reflectivity. Since $\hat{\mathsf{P}}_y^2 = (-1)^{2J}$, we get $\varepsilon^2 = (-1)^{2J}$. This means that for bosons, $\varepsilon = \pm 1$, and hence $\hat{P}_y$ is given by Eq. 7.14.

$$\hat{\mathsf{P}}_y \left|\varepsilon JM\right\rangle = \varepsilon \left|\varepsilon JM\right\rangle \tag{7.14}$$

Since the $M < 0$ states are incorporated into the equation together with the $M > 0$ states, the reflectivity representation has the added effect of reducing the density matrix operator into block diagonal form [2] where there is no interference between states of differing reflectivities.

The angular dependance of $\mathscr{M}$, depicted by the Wigner D-functions, when expressed in terms of the reflectivity states, enforces the value of ε to be $P(-1)^J$ when $M = 0$. An explicit calculation of this can be found in Ref. [5]. In the case considered here, with the resonance X decaying into two neutral kaons, we only have even J and positive parity, the $M = 0$ state has $\varepsilon = +1$.

7.3 Likelihood Function

We can calculate the Wigner D-functions using the relations given in Eqs. (7.9) and (7.10) . It now remains to fit our observed data to some parametrized model. Suppose we have a set of observations or events $i = 1, 2, ...N$ which can be defined by the set of variables $\vec{x}_i$. These events can be described by means of a model with parameters $\vec{a}$. We make use of the maximum likelihood method in which the quantity of interest is the likelihood which is a product of the probabilities, each of finding the system in a state described by $\vec{x}_i$, and

according to the parameters $\vec{a}$ (Eq. 7.15).

$$\mathscr{L} = \prod_{i=1}^{N_{data}} P(\vec{x}_i, \vec{a}) \tag{7.15}$$

The aim of this method is to completely describe the observed events with the help of this parametrized model. In our case, the observed quantity is the intensity, I, which, being the sum of squares of quantum mechanical states, is the probability in the likelihood function. Eq. 7.16 is used to calculate this for each mass bin:

$$\mathscr{L} \propto \prod_{i=1}^{N_{data}} I_{pred}(\Omega_{K_S i}) \tag{7.16}$$

N_{data} is the observed number of events in the given mass bin and $I_{pred}(\Omega_{K_S i})$ is the the predicted or expected intensity in that bin for the i^{th} event. If the experiment were to be repeated under exactly the same conditions, we would likely obtain a different value for N_{obs}. To account for this, we include the Poisson distribution for N_{data} in the expression for the likelihood function as shown in Eq. 7.17.

$$\mathscr{L} \propto \frac{\mathscr{N}^{N_{data}}}{N_{data}!} e^{-\mathscr{N}} \prod_{i=1}^{N_{data}} I_{pred}(\Omega_{K_S i}) \tag{7.17}$$

Here, $\mathscr{N}$ is the expectation value of N_{data} . This moves our procedure from calculating the likelihood function to calculating the extended likelihood function, because, in addition to the statistical variations in the measurements, the number of measurements themselves are statistical in nature.

We normalize this function with the observed intensity. The observed intensity is dependent on the acceptance, or the ability of the detector to measure the events at Ω_{K_S}, and hence the likelihood function is now expressed by Eq. 7.18.

$$\mathscr{L} \propto \frac{\mathscr{N}^{N_{data}}}{N_{data}!} e^{-\mathscr{N}} \prod_{i=1}^{N_{data}} \frac{I_{pred}(\Omega_{K_S i})}{\int \eta(\Omega_{K_S}) I_{pred}(\Omega_{K_S}) d\Omega_{K_S}} \tag{7.18}$$

Since $\mathscr{N}$ is the expectation value of the observed number of events, it can be denoted by Eq. 7.19.

$$\mathscr{N} = \int \eta(\Omega_{K_S}) I_{pred}(\Omega_{K_S}) d\Omega_{K_S} \tag{7.19}$$

Thus, the likelihood function is expressed by Eq. 7.20.

$$\mathscr{L} \propto \frac{1}{N_{data}!}\, exp(-\int \eta(\Omega_{K_S}) I_{pred}(\Omega_{K_S}) d\Omega_{K_S}) \prod_{i=1}^{N} I_{pred}(\Omega_{K_S i}) \tag{7.20}$$

This is then the function to be maximized in order to get the best correspondence between the observed data and our parametrized model. The computational accuracy of calculating a small number is greater than that of a large number, as is calculating the sum rather than the product. Hence, we take the log of the likelihood function (Eq. 7.21).

$$\ln \mathscr{L} \propto \sum_{i=1}^{N} \ln I_{pred}(\Omega_{K_S i}) - \mathscr{N} \tag{7.21}$$

Minimizing the negative log likelihood is then the same as maximizing the likelihood function, and this is what is done in our analysis. In the above expression, we have not included the constant terms because they only shift the value of the likelihood by a particular amount and do not contribute to the minimization process.

7.4 Intensity as a Function of Moments

We are now left with parametrizing the intensity in order to calculate the log likelihood. A multipole expansion of the intensity in terms of the spherical harmonics gives:

$$I_{pred}(\Omega_{K_S}) = \sum_{L=0}^{L_{mas}} \sum_{m=0}^{L} H_{LM} ReY_{LM}(\Omega_{K_S}) \tag{7.22}$$

where the coefficients of expansion, H_{LM} , are called the moments of the intensity distribution, and are denoted by Eq. 7.23 (refer to [5] for a detailed derivation).

$$H_{LM} = \int d\Omega I_{pred}(\Omega_{K_S}) ReY_{LM}(\Omega_{K_S}) \tag{7.23}$$

Thus, the moments are the intensity averaged spherical harmonics.

Due to the limitations of our detector, the observed intensity differs from that predicted for a perfect detector. We therefore need to account for the acceptance $\eta(\Omega_{K_S})$ of the detector using the relation given by Eq. 7.24.

$$I_{obs} = I_{pred}\eta(\Omega_{K_S}) \tag{7.24}$$

In the same way as the intensity, the acceptance function can also be expanded in terms of the spherical harmonics (Eq. 7.25).

$$\eta(\Omega_{K_S}) = \sum_{L=0}^{L_{mac}} \sum_{m=0}^{L} \eta_{LM} ReY_{LM}(\Omega_{K_S}) \tag{7.25}$$

As in the case of moments, the acceptance coefficients η_{LM} can be expressed in terms of speherical harmonics, as given by Eq. 7.26.

$$\eta_{LM} = \int \eta(\Omega_{K_S}) ReY_{LM}(\Omega_{K_S}) d\Omega_{K_S} \tag{7.26}$$

For the normalization condition, we use the relation expressed by Eq. 7.27.

$$N_{data} = \int I_{obs}(\Omega_{K_S}) d\Omega_{K_S} \tag{7.27}$$

Using Eq.(7.24), N_{data} is now denoted by Eq. 7.28.

$$N_{data} = \int I_{pred}\eta(\Omega_{K_S}) d\Omega_{K_S} \tag{7.28}$$

Substituting the value of $\eta(\Omega_{K_S})$ from Eq. (7.25), the expression for N_{data} can be simplified using Eqs. 7.29 - 7.31.

$$N_{data} = \int I_{pred} \sum_{L,M} \eta_{LM} ReY_{LM}(\Omega_{K_S}) d\Omega_{K_S} \tag{7.29}$$

$$= \sum_{L,M} \eta_{LM} \int I_{pred} ReY_{LM}(\Omega_{K_S}) d\Omega \tag{7.30}$$

$$\therefore N_{data} = \sum_{L,M} \eta_{LM} H_{LM} \tag{7.31}$$

We can then use the above equation to eliminate H_{00} (Eq. 7.32).

$$H_{00} = \frac{N_{data}}{\eta_{00}} - \sum_{L>0,m>0} \frac{\eta_{LM}}{\eta_{00}} H_{LM} \tag{7.32}$$

Using Eqs. (7.22) and (7.32), I_{pred} can now be expressed by Eq. 7.33.

$$I_{pred} = \frac{N_{data}}{\eta_{00}} Y_{00} + \sum_{L>0,M>0} [ReY_{LM}(\Omega_{K_S}) - \frac{\eta_{LM}}{\eta_{00}} Y_{00}] H_{LM} \tag{7.33}$$

To find the coefficients η_{LM}, we look at Eq. (7.26). For the acceptance, consider the fact that we generate N_{gen} events out of which N_{acc} are accepted after passing through the CLAS detector. The integral can therefore be approximated by Eq. 7.34.

$$\int \eta(\Omega_{K_S}) ReY_{LM}(\Omega_{K_S}) d\Omega_{K_S} = \frac{1}{N_{gen}} \sum_{i=1}^{N_{acc}} ReY_{LM}(\Omega_{K_S i}) \tag{7.34}$$

Substituting this in Eq.(7.26), the acceptance coefficients are now given by Eq. 7.35.

$$\eta_{LM} = \frac{1}{N_{gen}} \sum_{i-1}^{N_{acc}} ReY_{LM}(\Omega_{KSi}) \tag{7.35}$$

7.5 Moments Analysis

The unnormalized moments are given by Eq.7.23:

$$\tilde{H}_{LM} = \int I_{pred}(\Omega_{K_S}) ReY_{LM} d\Omega_{K_S}$$

In particular, the moment for $L = M = 0$ is given by Eq. 7.36:

$$\tilde{H}_{00} = \int I_{pred}(\Omega_{K_S}) d\Omega_{K_S} = accepted\ corrected\ number\ of\ events\ in\ that\ bin \tag{7.36}$$

where the constant term has been ignored.

The normalized moments can be calculated using the width of the bins and accounting for the beam luminosity. For each mass bin, the normalized moments are given by Eq. 7.37.

$$H_{LM} = \frac{\tilde{H}_{LM}}{\Delta m} I^{-1}(E) \tag{7.37}$$

Since we have not binned in energy, we then use the average of the luminosities for the entire energy range 2.7 GeV to 5.45 GeV. The mass is binned in 50MeV bins.

The cross-section in a given mass bin is just the accepted corrected number of events in that bin. And hence, the normalized cross-section is given by 7.38:

$$\frac{\Delta\sigma}{\Delta m} = \frac{N_{pred}}{\Delta m} I^{-1}(E) = \frac{\tilde{H}_{00}}{\Delta m} I^{-1}(E) \tag{7.38}$$

The moments are given by 7.39.

$$\tilde{H}_{LM} = \int I_{pred}(\Omega_{K_S}) ReY_{LM} d\Omega_{K_S}$$

$$\tilde{H}_{LM} = \int \frac{d\sigma}{dm d\Omega_{K_S}} ReY_{LM} d\Omega_{K_S} \tag{7.39}$$

When expanded using the reflectivity basis, the following set of equations gives the moments in terms of the partial waves. (Ref. [8]). The letters S, P, D stand for $L = 0, L = 1, L = 2$ respectively and the subscript stands for the reflectivity ε. When $L = 0$, M can only have one value, *i.e.,* 0. In this case, as seen in Section 7.2, there is only value of ε for which the state is non-vanishing. In our case, this is $+1$, but we take that to be understood and wherever P_0, D_0 are encountered, it is to be thought of as $L = 0$, M=0,ε=+1. For $L \neq 0$, we only go up to $M = 1$ and P_- stands for $L = 1,\ M = 1,\ \varepsilon = -1$.

The moments can be represented using this notation in Eqs. (7.5) through (7.51). In the expansion of the intensity in terms of multipole moments, there can be infinite number of contributing waves. However, we need to terminate the series at some point and we only include waves with $J \leq 2$. The contribution of P waves have been included even though we do not expect it to be present in the data unless as part of some unknown background. Resonances with $J \geq 3$ have mass that is too high for consideration in our data.

$$H_{00} = |S|^2 + |P_-|^2 + |P_0|^2 + |P_+|^2 + |D-|^2 + |D_0|^2 + |D_+|^2 \tag{7.40}$$

$$H_{10} = SP_0^* + P_0 S^* + \sqrt{\frac{3}{5}}(P_- D_-^* + P_- S^* + P_+ D_+^* + D_+ P_+^*) + \sqrt{\frac{4}{5}}(P_0 D_0^* + D_0 P_0^*) \tag{7.41}$$

$$H_{11} = \sqrt{\frac{1}{2}}(-P_-S^* - SP_-^* + P_+S^* + SP_+^*) + \sqrt{\frac{1}{20}}(P_-D_0^* + D_0P_-^* - P_+D_0^* - D_0P_+^*) + \sqrt{\frac{3}{20}}(P_0D_-^* - D_-P_0^* + P_0D_+^* + D_+P_+^*) \quad (7.42)$$

$$H_{20} = SD_0^* + D_0S^* + \sqrt{\frac{1}{5}}(2|P_0|^2 - |P_-|^2 - |P_+|^2) + \sqrt{\frac{5}{49}}(|D_-|^2 + |D_+|^2) + \sqrt{\frac{20}{49}}|D_0|^2 \quad (7.43)$$

$$H_{21} = \frac{1}{2}(SD_+^* + D_+S^* - SD_-^* - D_-S^*) + \sqrt{\frac{3}{20}}(P_0P_+^* + P_+P_0^* - P_-P_0^* - P_0P_-^*) + \sqrt{\frac{5}{196}}(D_0D_+^* + D_+D_0^* - D_0D_-^* - D_-D_0^*) \quad (7.44)$$

$$H_{22} = \sqrt{\frac{3}{10}}(P_-P_+^* + P_+P_-^*) + \sqrt{\frac{3}{196}}(-D_-D_+^* - D_+D_-^*) \quad (7.45)$$

$$H_{30} = \sqrt{\frac{18}{70}}(-P_-D_-^* - D_-P_-^* - P_+D_+^* - D_+P_+^*) + \sqrt{\frac{108}{140}}(P_0D_0^* + D_0P_0^*) \quad (7.46)$$

$$H_{31} = \sqrt{\frac{18}{140}}(P_+D_0^* + D_0P_+^* - P_-D_0^* - D_0P_-^*) + \sqrt{\frac{6}{35}}(P_0D_+^* + D_+P_0^* - P_0D_-^* - D_-P_0^*) \quad (7.47)$$

$$H_{32} = \sqrt{\frac{3}{14}}(-P_+D_-^* - D_-P_+^* - P_-D_+^* - D_+P_-^*) \tag{7.48}$$

$$H_{40} = \sqrt{\frac{16}{49}}(-|D_+|^2 - |D_-|^2) + \sqrt{\frac{36}{49}}|D_0|^2 \tag{7.49}$$

$$H_{41} = \sqrt{\frac{30}{196}}(D_0D_+^* + D_+D_0^* - D_-D_0^* - D_0D_-^*) \tag{7.50}$$

$$H_{42} = \sqrt{\frac{10}{49}}(-D_-D_+^* - D_+D_-^*) \tag{7.51}$$

Physically, the moments are a measure of the presence of different partial waves. H_{00} contains the amplitudes of all the waves and hence represents the total cross-section of the reaction. H_{10} and H_{11} contain the S and the D waves only as interference with the P wave. We do not expect the P wave to contribute to our reaction; if this is indeed the case, then the moments H_{10} and H_{11} should not show any structure. We will see in the next chapter that we do not in fact observe any specific shape for these two moments. If we were to generate moments of a pure D-wave, they would have non-zero values for H_{00}, H_{2x}, and H_{4x}, whereas the rest of the moments would be zero since the D waves only appear in them in conjunction with S/P waves.

The next chapter showcases the results obtained using this formalism.

8 RESULTS

The data and Monte Carlo is binned in 50 MeV mass bins. The low statistics do not allow for further binning in t or E_γ. The ϕ and $\cos\theta$ angles of K_S in the helicity frame for the generated simulations is shown in Fig. 8.1. The generated angles are, as expected, flat in phi and theta. After passing through the detector, the acceptance of CLAS produces a shape shown in Fig. 8.2. This is the acceptance for bin 1500-1550 MeV. Figs. 8.3 and 8.4 show the angular distributions of the data for the signal + background region and the sideband region respectively for the same bin.

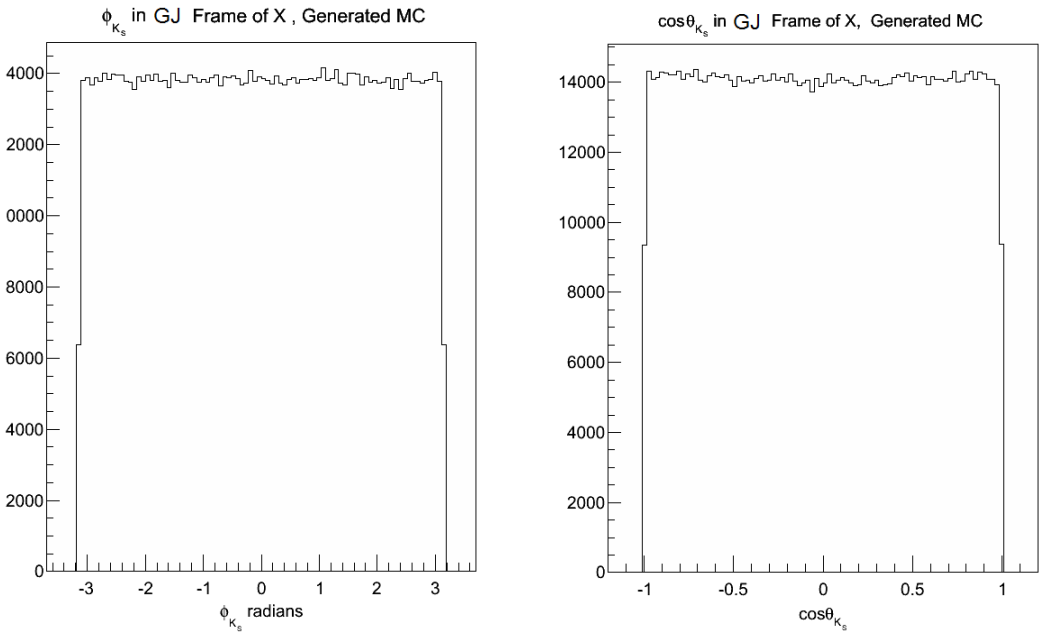

Figure 8.1: ϕ and $\cos\theta$ of K_S in the Gottfried Jackson frame of the resonance X for generated Monte Carlo.

Since we use the sideband subtraction method, we are unable to do the analysis on subtracted data. To get around this, we compare the regions which have signal + background (SB) with the sideband region. If the SB region follows the same pattern as the background region, then we can assume that the shape of the spectrum is formed by the background. Any deviations from the shape of background region will then give an idea

about the presence of particular waves in the signal. The fits were done in the helicity frame of the resonance as well as the Gottfried Jackson frame. A comparison between the two frames is shown in Fig. 8.5.

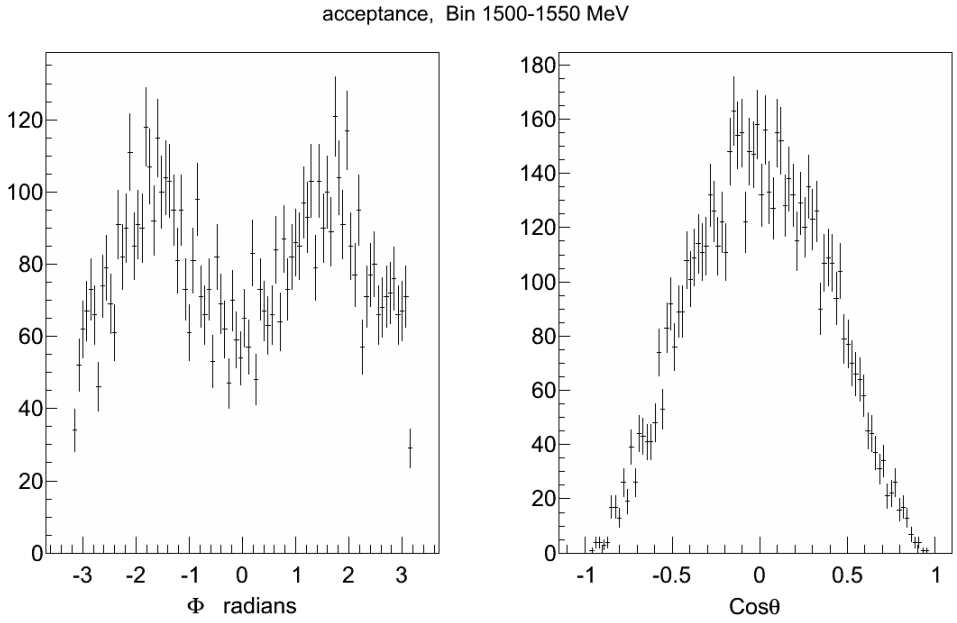

Figure 8.2: Angular distributions for a pure S wave, after having passed through the detector.

It is seen from these plots that the L = 2 moments vary greatly depending on the reference frame of the resonance that is used to calculate the angular distributions of the K_S. The choice of the frame used for the calculation of moments would depend on the dominant mechanism involved in the production of the resonance. Pomeron exchange is easily interpreted in s-channel helicity frame, while pion exchange is more sensitive to the GJ frame [143]. In photoproduction, the exchange of a Pomeron would result in the produced resonance having the same quantum numbers as the photon. Since the f_0/f_2 has opposite parity and different spin as compared to the photon, we expect that the dominant production mechanism in this case would be pion exchange.

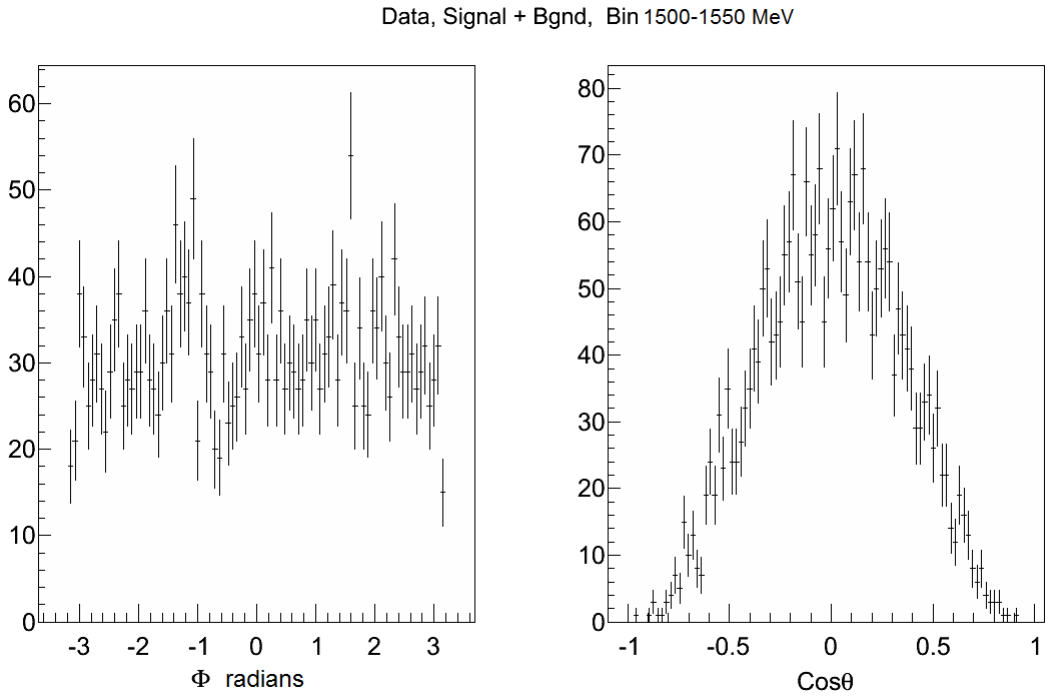

Figure 8.3: Angular distributions for the signal + background region of the data.

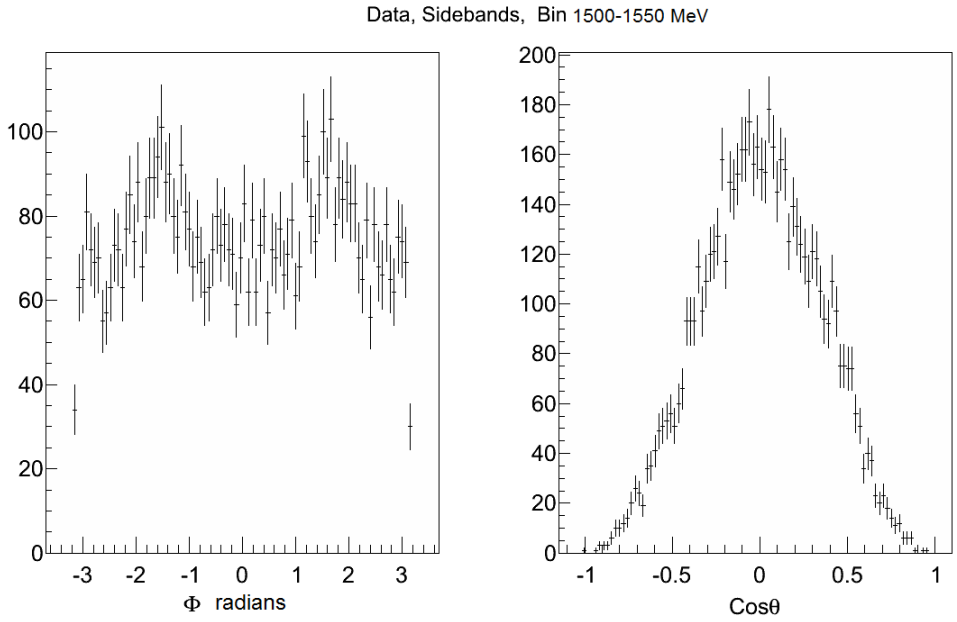

Figure 8.4: Angular distributions for the sideband region of the data.

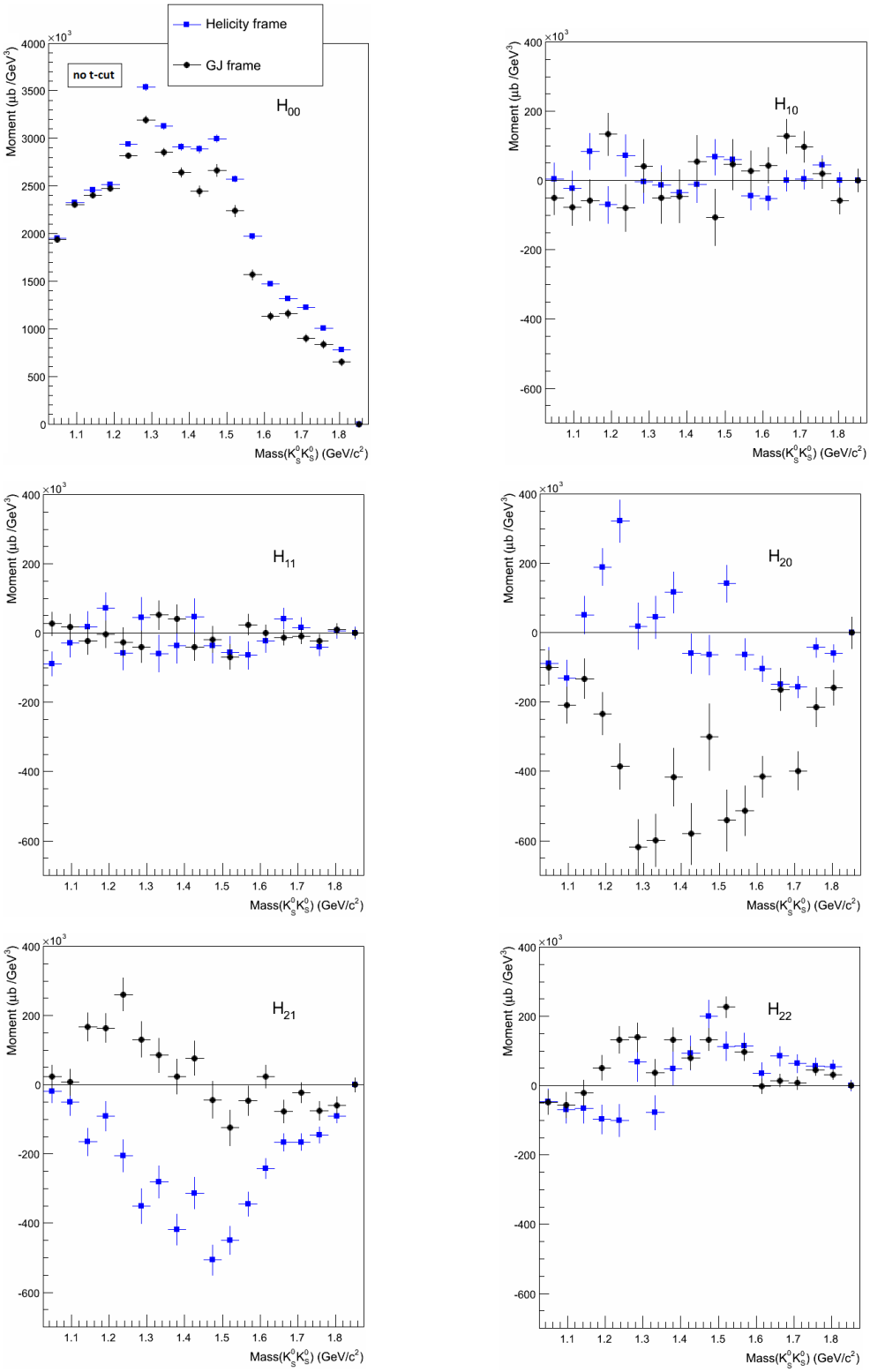

Figure 8.5: Comparison between fits in the helicity frame (blue squares) of the resonance, and the Gottfried Jackson frame (black circles) with no cut on t.

To have a test for the results from the data, a pure D0 wave was generated in the Gottfried Jackson frame. The $\cos\theta$ distributions for the generated and accepted pure D wave for various m and reflectivity values are shown in Figs. 8.8 and 8.7,but only D0 was made use of in the following test. The moments were calculated treating this pure D0 wave as pseudo-data. According to the Eqs. (chapter 7), for a pure D0 wave, the only non-zero moments should be H_{00} and H_{20}, and indeed, as seen from Fig. 8.8, this is the case. The pure D0 wave was then passed through the software routines GSIM, GPP and a1c (as explained in Chapter 6) to simulate the acceptance of the CLAS detector. The moments calculated using the accepted pure D0 wave as pseudo-data are plotted in Fig. 8.9. What is expected is that the accepted wave moments should show a similar trend as the generated wave, albeit with a difference in magnitude. What is seen is that the CLAS acceptance distorts the moments in an unexpected way. The H_{20} moment changes sign midway, and the H_{21} moment, which should only contain interference terms, also acquires a non-zero amplitude. This being the case, it will be difficult to interpret the moments results. What will be attempted is to only look at the bins 1450-1550 MeV, and compare with the corresponding bins for the pure D0 generated and accepted wave moments, to hazard a guess about the presence of a D wave in the resonance at 1500 MeV. A more definitive result might be obtained using the higher energies available at CLAS 12.

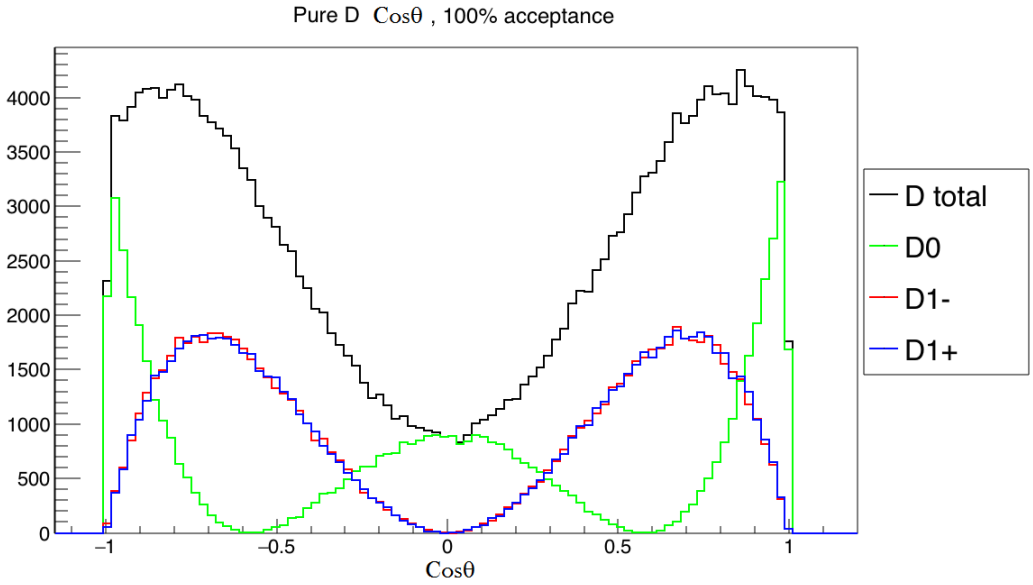

Figure 8.6: $\cos\theta$ for a pure D wave before passing through the detector with differing m and reflectivity values.

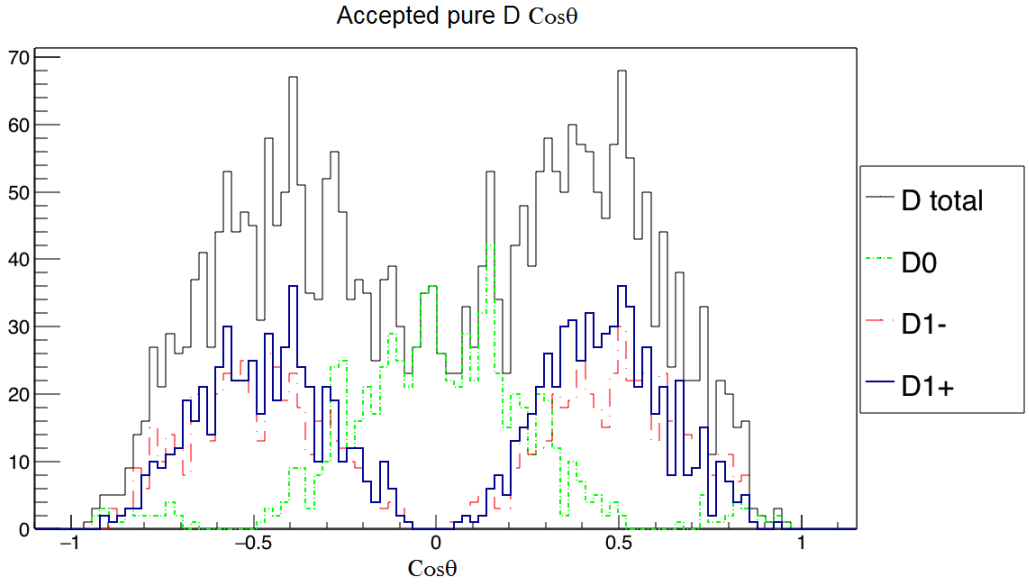

Figure 8.7: $\cos\theta$ for a pure D wave after passing through the detector with differing m and reflectivity values.

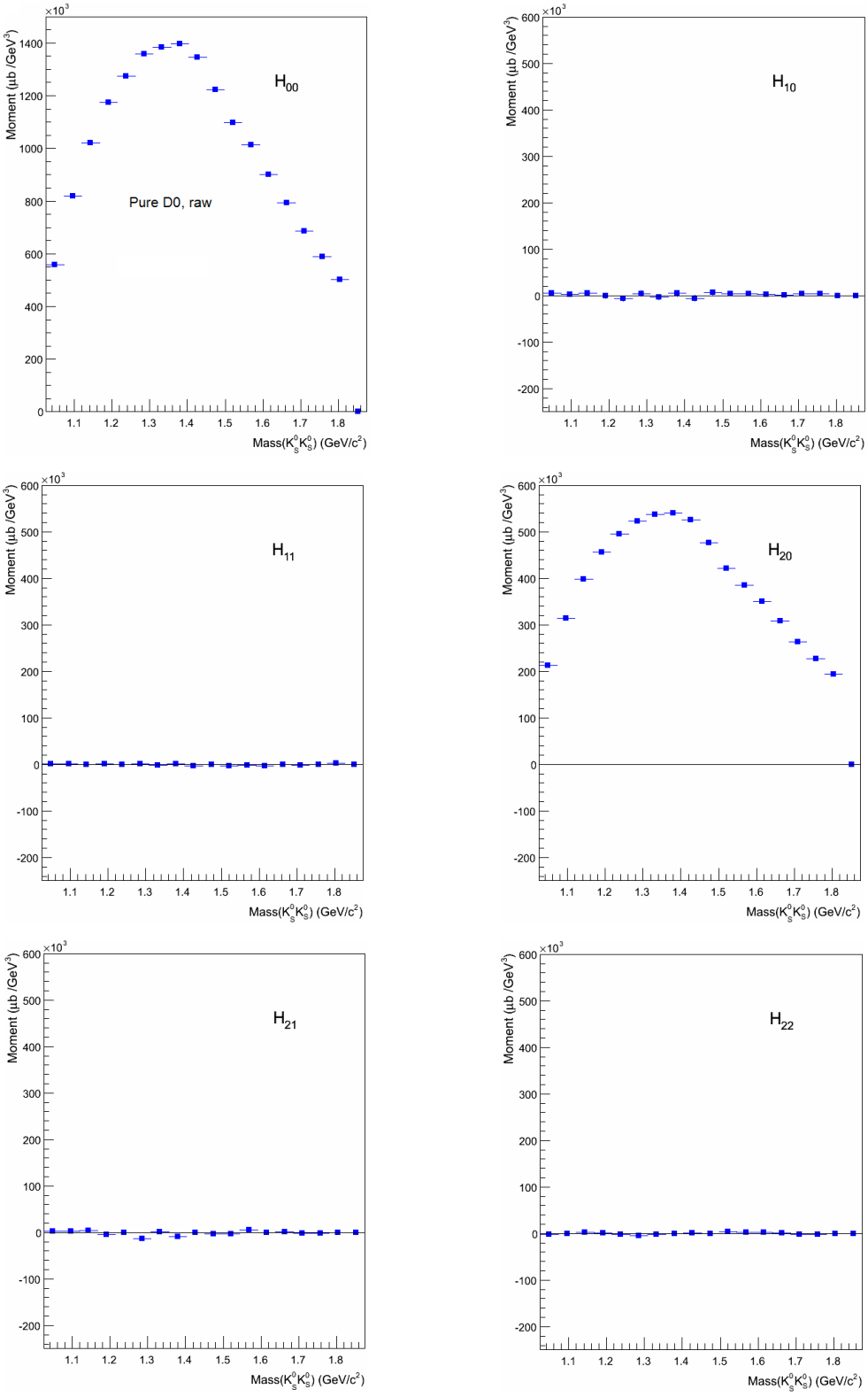

Figure 8.8: Moments for pure D0 wave generated in the Gottfried Jackson frame before passing through the CLAS detector.

Figs. 8.10, 8.11, 8.12, and 8.13 depict the fitted moments which have been calculated using the angular distribution of the K_S in the GJ frame.

The H_{00} moment represents the acceptance corrected invariant mass spectrum with peaks at ~1.2 GeV and 1.5 GeV. In Fig. 8.10, with no cut on the momentum transfer, almost all the moments for the signal + background (SB) region follow the same pattern as the sideband moments. The H_{20} displays a downward trend, with the SB moments having a larger magnitude than those of the sideband. For moments with$-t$ restricted to less than 1 GeV^2, portrayed in Fig. 8.11, there is a significant difference between the SB and sideband H_{20} moments-curves between 1500-1600 MeV. In the case of $-t > 1$ GeV^2, the moments for the SB and sidebands regions are mostly consistent with each other. These trends seem to suggest some presence of the D wave in the resonance at 1500 MeV. The amount of S and D waves present in this bin can only be determined by a full partial wave analysis. However, the current low acceptance at forward and backward angles (Fig. 8.2) causes an ambiguity between the S and D waves which does not allow for a proper interpretation via PWA. Possibly a similar experiment at CLAS 12 energies would yield more conclusive results.

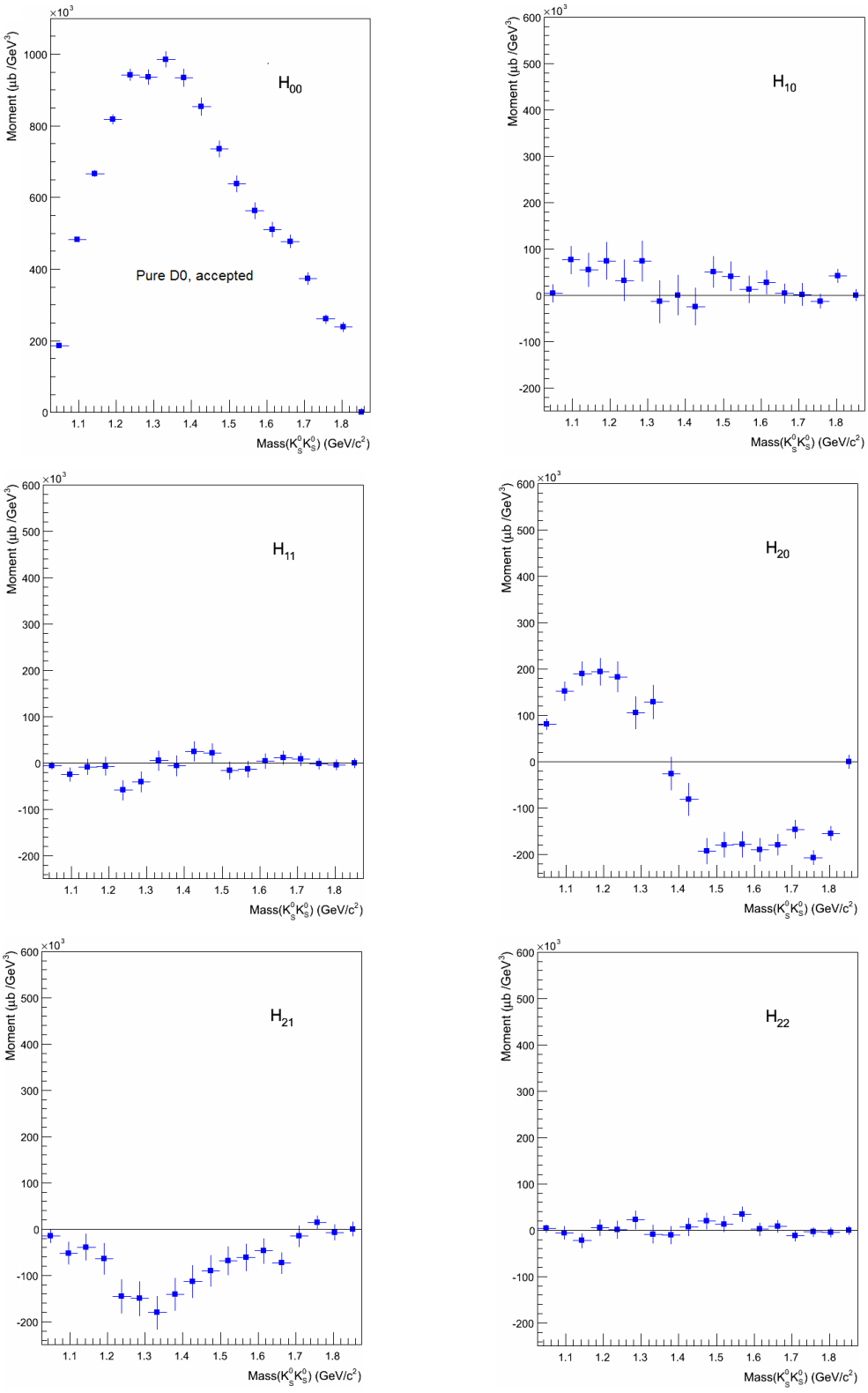

Figure 8.9: Moments for pure D0 wave generated in the Gottfried Jackson frame after passing through the CLAS detector.

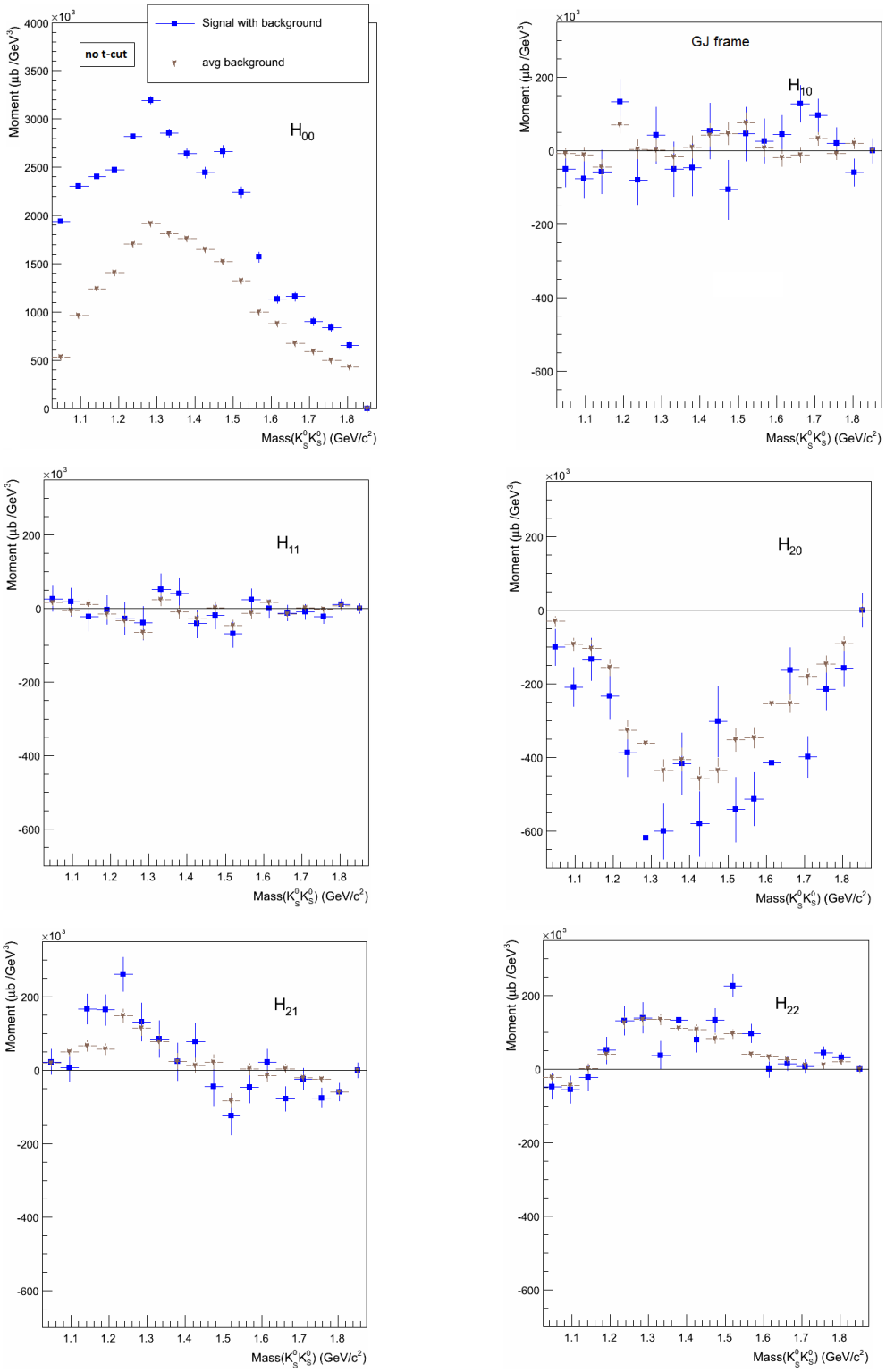

Figure 8.10: Moments generated by fitting the intensity in the Gottfried Jackson frame, no cut on t. The blue squares represent the signal + background region, whereas the brown stars represent the average of the four sidebands.

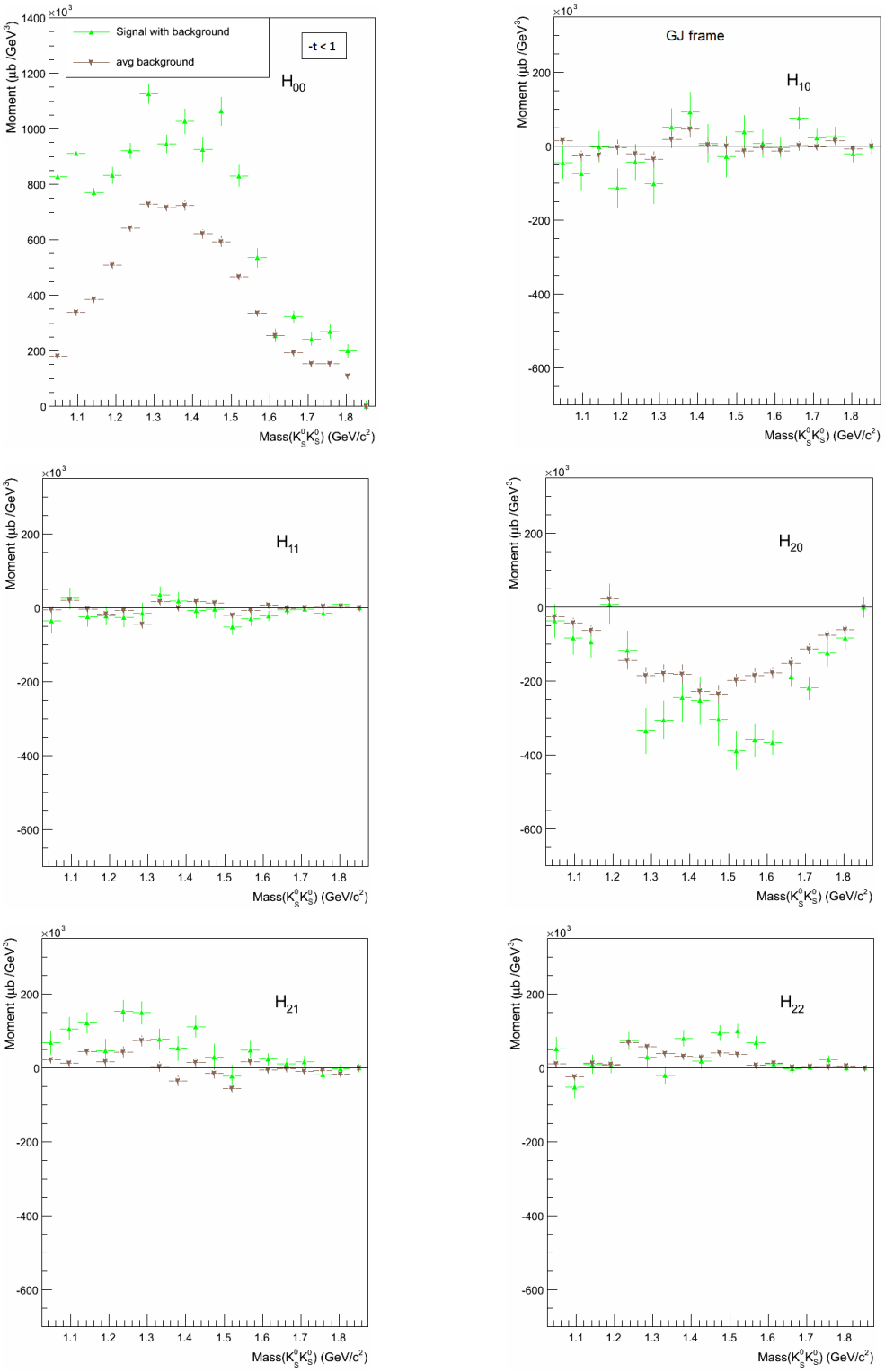

Figure 8.11: Moments generated by fitting the intensity in the Gottfried Jackson frame, -t < 1 GeV^2. The green triangles represent the signal + background region, whereas the brown stars represent the average of the four sidebands.

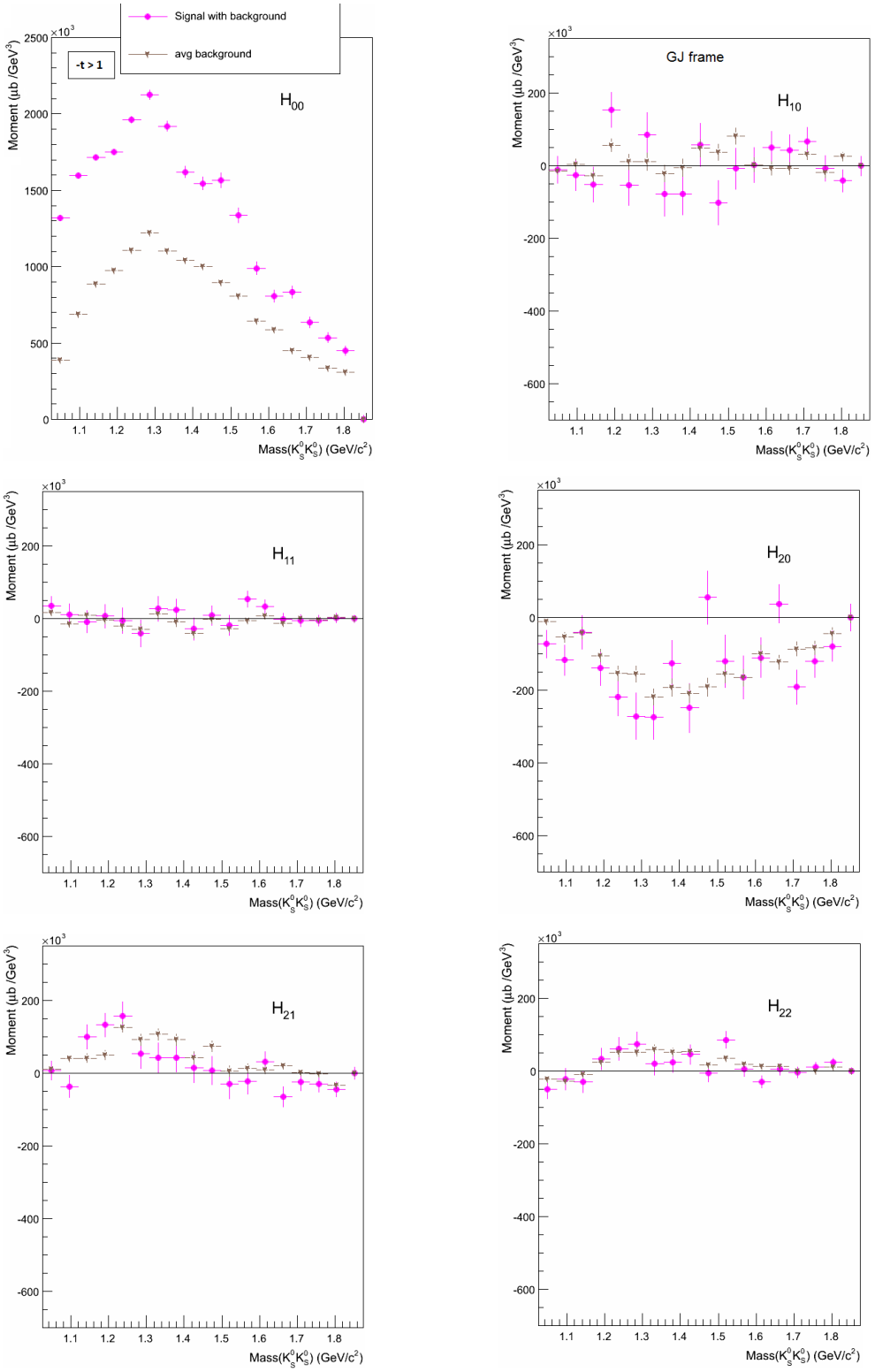

Figure 8.12: Moments generated by fitting the intensity in the Gottfried Jackson frame, -t > 1 GeV^2. The magenta circles represent the signal + background region, whereas the brown stars represent the average of the four sidebands.

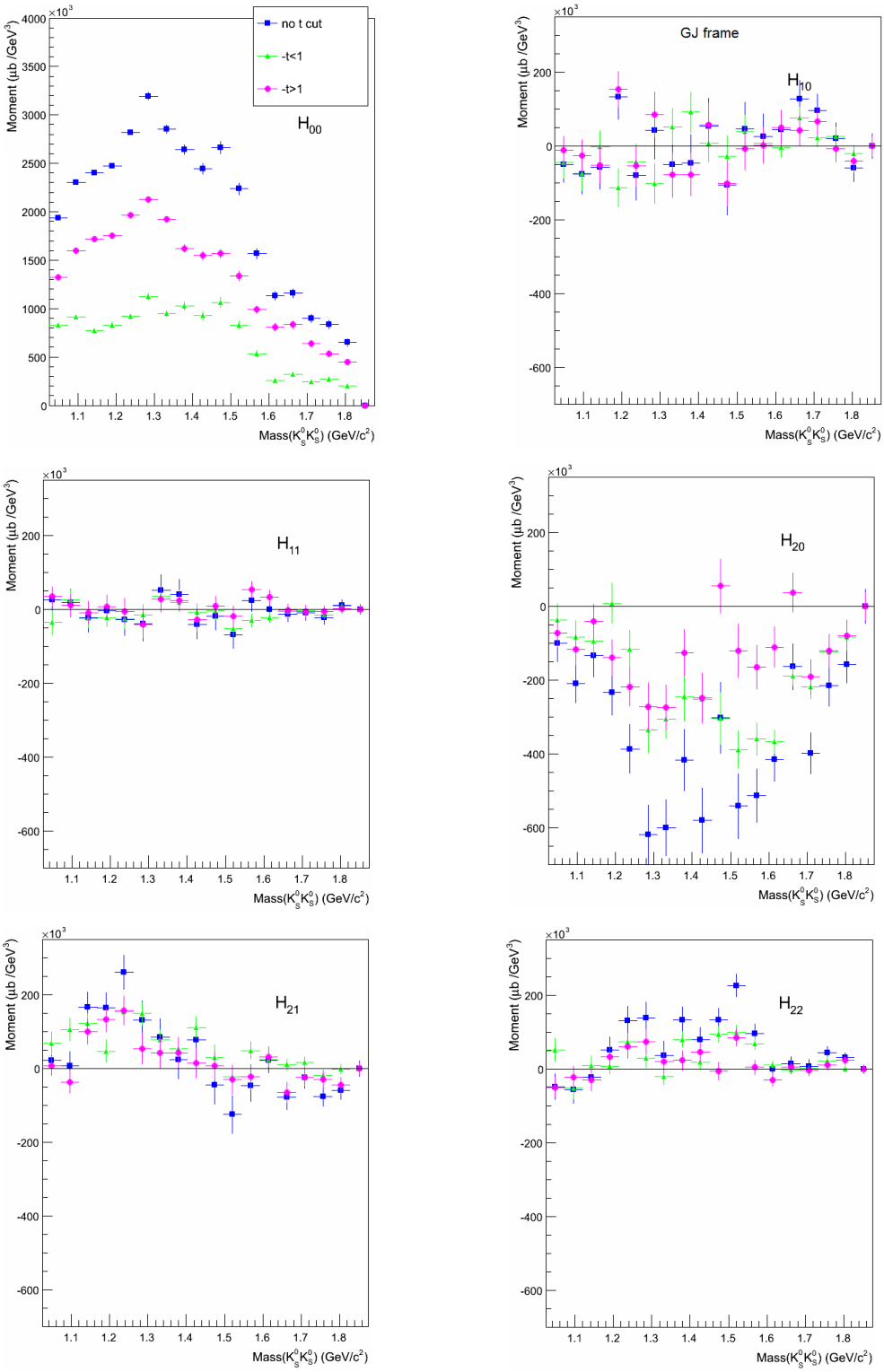

Figure 8.13: Comparison between moments in the GJ frame with various cutson t on the signal + background region. The blue squares represent no cut on t, the green triangles stand for $-t < 1$ GeV^2, and the magenta circles denote $-t > 1$ GeV^2.

9 SUMMARY AND DISCUSSION

Theoretically, glueballs have been well studied using lattice methods applied to the SU(3) colour Yang-Mills theory assuming no interaction with quarks [34, 149]. Determining how glueballs enter into the spectrum in full QCD with dynamical quark fields demands a complete calculation[144]. It is very difficult to reliably compute the couplings of glueballs to ordinary glueballs in QCD.

There have been some advances in theoretical computations over the years. Calculations using unquenched approximations are still in their very early stages and conservatively conclude that their results are broadly consistent with results from quenched QCD [147].

Though lattice QCD predicts the mass range of the lightest glueball, it does not back that up with decay widths and coupling information. This makes it difficult to identify the glueball from the spectrum of scalar mesons. G. t'Hooft *et. al* have made use of the instanton-induced effective six-fermion Lagrangian to characterize the decay of the scalar mesons, the states below 1 GeV can be described as largely tetraquark states, and the ones above 1 GeV as mostly $q\bar{q}$ states. QCD instantons produce mixing between the two types of states which gives rise to the ambiguity in the interpretation of the spectrum of of the heavier scalars [67]. Holographic QCD has been used to calculate the decay widths and branching ratios of the scalar mesons leading to the prediction that there would be small mixing between the scalar glueball and the $q\bar{q}$ states, and that the likelihood of the decay of a glueball into $4\pi_0$ is suppressed [148].

Attempts have been made to analyze the spectrum using Anti-DeSitter (*AdS*) supergravity duality. This is the perturbative expansion of string theory which is difficult to formulate, let alone solve, and is limited due a leading order strong coupling approximation. Ref. [145] reports that the pattern of spins, parities and mass inequalities obtained using this formulation bares a strong resemblance to the known QCD glueball spectrum.

A review of the various experiments that have been performed to hunt for the lightest glueball shows that the scalar meson spectrum is very difficult to decipher, as discussed in Chapter 2. In this dissertation, the reaction $\gamma p \to pX \to pK_SK_S$ was investigated using data from the g12 experiment performed at Jefferson Lab using the CLAS detector. This presents the first high statistics data for photoproduction of scalar mesons above 1 GeV. The final state detected particles were four charged pions; the choice of the final detected particles was made based on parity quantum number considerations. The sideband-subtraction method was employed to obtain the K_SK_S (or 4π) invariant mass spectrum after the necessary 'cuts'. This invariant mass spectrum showed clear peaks at around 1.28 GeV and 1.5 GeV, with some background still present. The physics associated with this background is unknown. The K_SK_Sp Dalitz plots do not indicate the presence of a baryon background.

At first glance, the resonance at 1.28 GeV could easily be mistaken for the $f_2(1270)$. However, the width of the observed peak is much smaller than the average PDG listed width of the $f_2(1270)$, so it is not clear which particle this resonance represents.

The resonance at 1.5 GeV is distinctly seen at low momentum transfer, but disappears for $-t > 1$ GeV^2; this is consistent with t-channel meson production. We hypothesize that since we are investigating resonances with $J = 0, 2$ and $PC = ++$, the dominant exchange mechanism involved in the production of the resonance is pion exchange. This leads us to perform a moments analysis of the data in the Gottfried Jackson frame of the resonance, since we expect that it will be simpler to interpret the results in this frame. Since we are unable to perform an analysis on sideband subtracted data, we fit moments to both the signal and sideband regions and then compare between the two. Differences between the two curves would then be indicative of some structure. In order to be able to compare to a known distribution, we first generated pure D waves before and after passing through a simulated version of the CLAS detector. It is seen that the acceptance of CLAS distorts the distribution in a way that does not match expected values. Due to this, we look at only

the mass bins around 1.5 GeV to make a guesstimate about the presence of an $L = 2$ wave in the data. The H_{00} moment shows the acceptance corrected 4π invariant mass spectrum. Besides this, for most other moments, the sidebands follow the same pattern as the (signal + background), except for the H_{20} moment which shows a definite difference between the two regions. This suggests some presence of the D wave in the resonance at 1500 MeV. A definitive determination of the amount of S and D waves present in this bin can be done by performing a full partial wave analysis. The current low acceptance at forward and backward angles for this decay channel prevents us from doing so in this analysis.

This is the first time that this final state has been analyzed in photoproduction and hence contributes new information to the world data on scalar mesons. Future experiments with energies at CLAS 12 might afford better statistics and better acceptance for more conclusive results.

REFERENCES

[1] S.U. Chung, *Spin Formalisms*, Unpublished BNL preprint BNL-QGS-02-0900, 2007.

[2] S.U.Chung and T.L. Trueman, P*ositivity Conditions on the spin density matrix: A simple parametrization*, Phys Rev. D11, 663, 1975.

[3] J.D. Richman, *An Experimenter's Guide to the Helicity Formalism*, CALT-68-1148, 1984.

[4] S.U.Chung, *Formulas for Partial Wave Analysis, Version II*. Unpublished BNL preprint BNL-QGS-93-05, 1999.

[5] C.W. Salgado and D.P.Weygand, *On the Partial-Wave Analysis of Mesonic Resonances Decaying to Multiparticle Final States Produced by Polarized Photons*, arXiv:1310.7498v2, 2013.

[6] K. Peters, *A Primer on Partial Wave Analysis*, arXiv:hep-ph/0412069v1, 2004.

[7] S. Lombardo, *Analysis of K^+K^- Production from the g11 Data Set*.

[8] M. Battaglieri, R. De Vita, L.Bibrzycki, L.Lesniak, A.Szczepaniak, A*nalysis of $\pi^+\pi^-$ production from the g11 data set*, CLAS Analysis Note, 2008.

[9] J.J. Sakurai*, Modern Quantum Mechanics,* Pearson Education, 2007.

[10] J. Beringer et al. (Particle Data Group), *Passage of particles through matte*r, Phys. Rev. D86, 010001, 2012.

[11] E. Pasyuk, *Energy loss corrections for charged particles in CLAS*, CLAS-NOTE, (2007-016), 2007.

[12] P. Eugenio et al., *Search for new forms of hadronic matter in photoproduction*, Technical report, CLAS Analysis Proposal PR04-005, 2003.

[13] D. Weygand et al., *Study of pentaquark states in photoproduction off protons*, Technical report, CLAS Analysis Proposal PR04-017, 2004.

[14] W. Chen et al., *The $\gamma p \to \pi^+ n$ single charged pion photoproduction*, Technical report, CLAS Analysis Proposal PR08-003, 2008.

[15] C. W. Leemann, D. R. Douglas and G. A. Krat, T*he Continuous Electron Beam Accelerator Facility: CEBAF at the Jefferson Laboratory,* Ann. Rev. Nucl. Part. Sci., 51:413-450, 2001.

[16] B. A. Mecking et al, *The CEBAF large acceptance spectrometer (CLAS),* Nucl. Instr. and Meth. A, 503:513, 2003

[17] Jefferson Lab Flickr website, https://www.flickr.com/photos/jeffersonlab/

[18] D. I. Sober et al., *The bremsstrahlung tagged photon beam in Hall B at JLab*, Nucl. Instrum. Meth., A440:263-284, 2000.

[19] Y. G. Sharabian et al., *A new highly segmented start counter for the CLAS detector*, Nucl. Instrum. Meth., A556:246-258, 2006.

[20] G. Adams et al., *The CLAS Cherenkov detector.* Nucl. Instrum. Meth., A465:414-427, 2001.

[21] M. Amarian et al., *The CLAS forward electromagnetic calorimeter*, Nucl. Instrum. Meth., A460:239-265, 2001.

[22] M. Mestayer, *The clas drift chamber system,* Nucl. Instr. and Meth. A, 449:81– 111, 2000.

[23] E. S. Smith, *The time-of-flight system for CLAS*, Nucl. Instr. and Meth. A, 432:265–298, 1999.

[24] Steven B. Christo, “g11a, eg3a, g8b and g13b Target Cell ”, https://userweb.jlab.org/~christo/g11a target.html

[25] http://education.jlab.org/sitetour/guidedtour05.l.alt.html

[26] Alan J. Street et al., *Final Site Assembly and Testing of the Superconduction Toroidal Magnet for the CEBAF Large Acceptance Spectrometer (CLAS)*, IEEE Trans. Mag. 32, No. 4, 2074, 1996.

[27] g12 procedures, CLAS analysis note, https://jlabsvn.jlab.org/svnroot/clas/docs/g12analysisprocedure/

[28] V. Crede, C. A. Meyer, *The Experimental Status of Glueballs*, Prog.Part.Nucl.Phys.63:74-116,2009, arXiv:0812.0600v3, 2009.

[29] V. Mathieu, N. Kochelev and V. Vento, *The Physics of Glueballs*, arXiv:0810.4453,2008.

[30] E. Klempt and A. Zaitsev, *Glueballs, Hybrids, Multiquarks. Experimental facts versus QCD inspired concepts*, Phys. Rept. 454, 2007 , arXiv:0708.4016 [hep-ph].

[31] N. Isgur and J.E. Paton, *A Flux Tube Model for Hadrons in QCD*, Phys. Rev. D, 31 (1985) 2910.

[32] M.S. Chanowitz, *Resonances in Photon-Photon Scattering*, Presented at 6th Int. Workshop on Photon-Photon Collisions, Lake Tahoe, CA, Sep 10-13, 1984.

[33] M. Chanowitz, *Chiral suppression of scalar glueball decay,* Phys. Rev. Lett. 95, 172001,2005, hep-ph/0506125.

[34] Y. Chen et al., *Glueball spectrum and matrix elements on anisotropic lattices*, Phys. Rev. D, 73 (2006) 014516, hep-lat/0510074.

[35] ZEUS Collaboration: S. Chekanov *et al*., *Inclusive $K_S^0 K_S^0$ resonance production in ep collisions at HERA*, Phys.Rev.Lett.101:112003,2008, arXiv:0806.0807v2 .

[36] Curtis A. Meyer, *An Experimental Overview of Gluonic Mesons*, arXiv:hep-ex/0308010v1.

[37] A. Chodos, R. L. Jaffe, K. Johnson, C. B. Thorn and V. F. Weisskopf, *New extended model of hadrons*, 10.1103/PhysRev D, 9,3471, 1974.

[38] F.E.Close, *Introduction to Quarks and Partons*, London ; New York : Academic Press, 1979.

[39] David Griffiths, *Introduction to Elementary Particles*, 2nd, Revised Edition, Weinheim : Wiley-VCH, c2008.

[40] W.J. Lee and D. Weingarten, *Scalar quarkonium masses and mixing with the lightest scalar glueball*, Phys. Rev. *D*, 61 (2000) 014015, hep-lat/9910008//crede 21.

[41] M. Ablikim et al., [BES Collaboration], *Partial Wave Analysis of $J/\Psi \to \gamma\pi + \pi^-$ and $\gamma\pi^0\pi^0$*, Phys. Lett. B*,* 642 (2006) 441.

[42] D. Barberis et al., [WA102 Collaboration], *A coupled channel analysis of the centrally produced K^+K^- and $\pi^+\pi^-$ final states in pp interactions at 450 GeV/c*, Phys. Lett. B*,* 462 (1999) 462, hep-ex/9907055.

[43] M. Acciarri et al., [L3 Collaboration], *$K_S^0 K_S^0$ final state in two-photon collisions and implications for glueballs*, Phys. Lett. *B*, 501 (2001) 173, hep-ex/0011037.

[44] http://www.scied.science.doe.gov/scied/JUR_v7/pdfs/Physics.pdf

[45] M. Gell-Mann and Y. Ne'eman, *The Eightfold Way* , New York: Benjamin, 1964.

[46] C. Amsler et al., [Particle Data Group Collaboration], *Quark Model, Review of Particle Physics*, Phys. Lett.B, 667, 2008.

[47] Image source: http://www.nano.org.uk/news/221/

[48] http://hyperphysics.phy-astr.gsu.edu/hbase/particles/expar.html

[49] www.quantumdiaries.org/2010/10/03/world-of-glue/

[50] J.Beringer et al., (Particle Data Group), Phys. Rev. D88, 0100001 (2012) & 2013 partial update for the 2014 edition.

[51] J.Beringer et al., (Particle Data Group), *Note on scalar mesons below 2 GeV*, Phys. Rev. D88, 0100001 (2012) & 2013 partial update for the 2014 edition.

[52] C. Amsler and F.E. Close, *Evidence for a scalar glueball*, Phys. Lett. B353 (1995) 385, hep- ph/9505219.

[53] C. Amsler and F.E. Close, *Is $f_0(1500)$ a scalar glueball?*, Phys. Rev. D53 (1996) 295, hep- ph/9507326.

[54] F.E. Close, G.R. Farrar and Z.p. Li, *Determining the gluonic content of isoscalar mesons*, Phys. Rev. D55 (1997) 5749, hep-ph/9610280.

[55] F. Giacosa et al., *Scalar nonet quarkonia and the scalar glueball: Mixing and decays in an effective chiral approach*, Phys. Rev. D72 (2005) 094006, hep-ph/0509247.

[56] H.Y. Cheng, C.K. Chua and K.F. Liu, *Scalar glueball, scalar quarkonia, and their mixing*, Phys. Rev. D74 (2006) 094005, hep-ph/0607206.

[57] C. Amsler, *Proton antiproton annihilation and meson spectroscopy with the Crystal Barrel*, Rev. Mod. Phys. 70 (1998) 1293, hep-ex/9708025.

[58] S. Devons et al., Observations of $p\bar{p} \to 3\pi^0, 2\pi^0\eta$ at Rest, Phys. Lett. B47 (1973) 271. N.N. Achasov et al., The $\phi \to \eta\pi^0\gamma$decay, Phys. Lett. B479, 53 (2000).

[59] N.N. Achasov et al., *The*$\phi(1020) \to \pi^0\pi^0\gamma$ *decay*, Phys. Lett. B485, 349 (2000).

[60] R.R. Akhmetshin et al., *First observation of the* $\phi \to \pi^+\pi^-\gamma$ *decay*, Phys. Lett. B462, 371 (1999).

[61] A. Aloisio et al., *Study of the Decay* $\phi \to \eta\pi^0\gamma$ *with the KLOE detector*, Phys. Lett. B536, 209 (2002).

[62] F. Ambrosino et al., *Dalitz plot analysis of* $e^+e^- \to \pi^0\pi^0\gamma$ *events at* $\sqrt{s} \backsimeq M_\phi$ *with the KLOE detector*, Eur. Phys. J. C49, 473 (2007).

[63] M. Ablikim et al. [BES Collaboration], *The* σ *pole in* $J/\psi \to \omega\pi^+\pi^-$, Phys. Lett. B 598 (2004) 149, hep-ex/0406038.

[64] M. Ablikim et al. [BES Collaboration], *Resonances in* $J/\psi \to \phi\pi^+\pi^-$ *and*ϕK^+K^-, Phys. Lett. B 607 (2005) 243, hep-ex/0411001.

[65] A. Deandrea et al., *The* $s\bar{s}$ *and* $K\bar{K}$ *nature of* $f_0(980)$ *in* D_s *decays,* Phys. Lett. B502, 79 (2001).

[66] F. Giacosa and G. Pagliara, *On the spectral functions of scalar mesons*, Phys. Rev. C76, 065204 (2007).

[67] G. 'tHooft et al., *A theory of scalar mesons*, Phys. Lett. B662, 424 (2008).

[68] M. Boglione and M.R. Pennington, *Dynamical generation of scalar mesons*, Phys. Rev. D65, 114010 (2002).

[69] C.Z. Yuan, *Hadron Spectroscopy from BES and CLEO-c*, AIP Conf. Proc. 814 (2006) 65, hep- ex/0510062.

[70] D. Black et al., *Mechanism for a next-to-lowest lying scalar meson nonet*, Phys. Rev. D61, 074001 (2000).

[71] BES Collaboration, *M. Ablikim et al.,Study of* $J/\psi \to \omega K^+K^-$, Phys. Lett. B 603, 138 (2004).

[72] BES Collaboration, J. Z. Bai et al., *Partial wave analyses of* $J/\Psi \to \gamma K^+K^-$ *and* $\gamma K^0_S K^0_S$, Phys. Rev. D 68, 052003 (2003).

[73] J.Z. Bai et al. [BES Collaboration], *Experimental study of* J/ψ *radiative decay to* $\pi^0\pi^0$, Phys. Rev. Lett. 81 (1998) 1179.

[74] J.Z. Bai et al. [BES Collaboration], *Partial Wave Analysis of* $J/\psi \to \gamma K^+K^-$ *and* $\gamma K^0_S K^0_S$, Phys. Rev. D 68 (2003) 052003, hep-ex/0307058.

[75] M. Ablikim et al. [BES Collaboration], *Partial Wave Analysis of* $J/\psi \to \gamma\pi^+\pi^-$ *and* $\gamma\pi^0\pi^0$, Phys. Lett. B 642 (2006) 441.

[76] J.Z. Bai et al. [BES Collaboration], *Partial Wave Analysis of* $J/\psi \to \gamma\pi^+\pi^-\pi^+\pi^-$, Phys. Lett. B 472 (2000) 207.

[77] A. Abele et al., $p\bar{p}$ *annihilation at rest into* $K_L K^\pm\pi^\mp$, Phys. Rev. D57, 3860 (1998).

[78] C. Amsler et al., *Coupled channel analysis of antiproton proton annihilation into* $\pi^0\pi^0\pi^0$, $\pi^0\eta\eta$, *and* $\pi^0\pi^0\eta$, Phys. Lett. B355, 425 (1995).

[79] A. Abele et al., *A Study of* $f_0(1500)$ *decays into 4* π^0*'s in proton antiproton annihilation into five* π^0*'s at rest,* Phys. Lett. B380, 453 (1996).

[80] D. Barberis et al., *A Coupled channel analysis of the centrally produced* K^+K^- *and* $\pi^+\pi^-$ *final states in* $p\bar{p}$ *interactions at 450-GeV/c*, Phys. Lett. B462, 462 (1999).

[81] D. Barberis et al., *A Study of the $\eta\eta$ channel produced in central $p\bar{p}$ interactions at 450-GeV/c*, Phys. Lett. B479, 59 (2000).

[82] A. Adamo et al., *.New Results on Meson Spectroscopy from OBELIX*, Nucl. Phys. A558, 13C (1993).

[83] M. Bargiotti et al. [OBELIX Collaboration], *Coupled channel analysis of $\pi^+\pi^-\pi^0$, $K^+K^-\pi^0$ and $K^\pm K_0^S\pi^\mp$from $p\bar{p}$ annihilation at rest in hydrogen targets at three densities*, Eur. Phys. J. C26 (2003) 371.

[84] C. Amsler et al., *Observation of a Scalar Resonance decaying to $\pi^+\pi^-\pi^0\pi^0$ in Antiproton Proton Annihilation at Rest*, Phys. Lett. B322, 431 (1994).

[85] D. Barberis et al. [WA102 Collaboration], *A study of the centrally produced $\pi^+\pi^-\pi^+\pi^-$ channel in pp interactions at 450 GeV/c*, Phys. Lett. B413 (1997) 217, hep-ex/9707021.

[86] D. Barberis et al. [WA102 Collaboration], *A study of the $K\bar{K}\pi$ channel produced centrally in pp interactions at 450 GeV/c,* Phys. Lett. B413 (1997) 225, hep-ex/9707022.

[87] D. Barberis et al. [WA102 Collaboration], *A spin analysis of the 4π channels produced in central pp interactions at 450 GeV/c*, Phys. Lett. B471 (2000) 440, hep-ex/9912005.

[88] D. Barberis et al. [WA102 Collaboration], *A partial wave analysis of the centrally produced $\pi^0\pi^0$system in pp interactions at 450 GeV/c*, Phys. Lett. B453 (1999) 325, hep-ex/9903044.

[89] D. Barberis et al. [WA102 Collaboration], *A partial wave analysis of the centrally produced $\pi^+\pi^-$ system in pp interactions at 450 GeV/c*, Phys. Lett. B453 (1999) 316, hep-ex/9903043.

[90] D. Barberis et al. [WA102 Collaboration], *A partial wave analysis of the centrally produced K^+K^- and $K^0_SK^0_S$ systems in pp interactions at 450 GeV/c and new information on the spin of the $f_J(1710)$*, Phys. Lett. B453 (1999) 305, hep-ex/9903042.

[91] D. Barberis et al. [WA102 Collaboration], *A study of the $\eta\eta'$ and $\eta'\eta'$ channels produced in central pp interactions at 450 GeV/c*, Phys. Lett. B471 (2000) 429, hep-ex/9911041.

[92] D. Barberis et al. [WA102 Collaboration], *A study of the $f_0(1370)$, $f_0(1500)$, $f_0(2000)$ and $f_2(1950)$ observed in the centrally produced 4π final states,* Phys. Lett. B474 (2000) 423, hep- ex/0001017.

[93] R. Barate et al. [ALEPH Collaboration], *Search for the glueball candidates $f_0(1500)$ and $f_J(1710)$ in $\gamma\gamma$ collisions*, Phys. Lett . B472 (2000) 189, hep-ex/9911022.

[94] S. Ahmad et al. [ASTERIX Collaboration], *The ASTERIX Spectrometer at LEAR*, Nucl. Instrum. Meth. A286 (1990) 76.

[95] E. Aker et al. [Crystal Barrel Collaboration], *The Crystal Barrel spectrometer at LEAR*, Nucl. Instrum. Meth. A321 (1992) 69.

[96] A. Adamo et al. [OBELIX Collaboration], *First physics results from OBELIX*, Sov. J. Nucl. Phys. 55 (1992) 1732.

[97] J.Z. Bai et al. [BES Collaboration], *The BES upgrade*, Nucl. Instrum. Meth. A458 (2001) 627.

[98] S.E. Kopp, [CLEO Collaboration], *The CLEO III Detector*, Nucl. Instrum. Meth. A384 (1996) 61.

[99] D. Decamp et al. [ALEPH Collaboration], *ALEPH: A Detector for Electron-Positron Annihilations at LEP*, Nucl. Instrum. Meth. A294 (1990) 121.

[100] [L3 Collaboration], *The Construction of the L3 Experiment*, Nucl. Instrum. Meth. A289 (1990) 35.

[101] F. Binon et al. [GAMS-2000 Collaboration], *Hodoscope Multi-Photon Spectrometer Gams-2000*, Nucl. Instrum. Meth. A248 (1986) 86.

[102] T.A. Armstrong et al. [WA76 Collaboration], *Study of the centrally produced $\pi\pi$ and $\bar{K}K$ systems at 85 GeV/c and 300 GeV/c*, Z. Phys. C51 (1991) 351.

[103] F. Antinori et al. [WA91 Collaboration], *A Further study of the centrally produced $\pi^+\pi^-$ and $\pi^+\pi^-\pi^+\pi^-$ channels in pp interactions at 300 and 450 GeV/c*, Phys. Lett. B353 (1995) 589.

[104] F. Ambrosino et al. [KLOE Collaboration], *Study of the decay$\varphi \to f0(980)\gamma \to \pi^+\pi^-\gamma$ with the KLOE detector*, Phys. Lett. B634 (2006) 148, hep-ex/0511031.

[105] V. Crede, C. A. Meyer, *The Experimental Status of Glueballs*, Prog.Part.Nucl.Phys.63:74-116,2009, *arXiv*:0812.0600v3, 2009.

[106] V. Mathieu, N. Kochelev and V. Vento, *The Physics of Glueballs*, arXiv:0810.4453,2008.

[107] E. Klempt and A. Zaitsev, *Glueballs, Hybrids, Multiquarks. Experimental facts versus QCD inspired concepts*, Phys. Rept. 454 (2007) 1, arXiv:0708.4016 [hep-ph]

[108] N. Isgur and J.E. Paton, *A Flux Tube Model for Hadrons in QCD*, Phys. Rev. *D*, 31 (1985) 2910.

[109] M.S. Chanowitz, *Resonances in Photon-Photon Scattering*, Presented at 6th Int. Workshop on Photon-Photon Collisions, Lake Tahoe, CA, Sep 10-13, 1984.

[110] M. Chanowitz, *Chiral suppression of scalar glueball decay*, Phys. Rev. Lett. 95 (2005) 172001, hep-ph/0506125.

[111] Y. Chen et al., *Glueball spectrum and matrix elements on anisotropic lattices,* Phys. Rev. D, 73 (2006) 014516, hep-lat/0510074.

[112] ZEUS Collaboration: S. Chekanov et al., *Inclusive $K_S^0 K_S^0$ resonance production in ep collisions at HERA*, Phys.Rev.Lett.101:112003,2008, arXiv:0806.0807v2.

[113] Curtis A. Meyer, *An Experimental Overview of Gluonic Mesons*, arXiv:hep-ex/0308010v1.

[114] A. Chodos, R. L. Jaffe, K. Johnson, C. B. Thorn and V. F. Weisskopf, *New extended model of hadrons*, 10.1103/PhysRev D, 9,3471, 1974.

[115] F.E.Close, *Introduction to Quarks and Partons*, London ; New York : Academic Press, 1979.

[116] David Griffiths, *Introduction to Elementary Particles*, 2nd, Revised Edition, Weinheim : Wiley-VCH, c2008.

[117] www.jlab.org/~devita/tesi/chapter2.ps.gz

[118] W.J. Lee and D. Weingarten, *Scalar quarkonium masses and mixing with the lightest scalar glueball*, Phys. Rev. D, 61 (2000) 014015, hep-lat/9910008.

[119] M. Ablikim et al. [BES Collaboration], *Partial Wave Analysis of $J/\Psi \to \gamma\pi + \pi^-$ and $\gamma\pi^0\pi^0$*, Phys. Lett. B, 642 (2006) 441.

[120] D. Barberis et al. [WA102 Collaboration], *A coupled channel analysis of the centrally produced K^+K^- and $\pi^+\pi^-$ final states in pp interactions at 450 GeV/c,* Phys. Lett. B, 462 (1999) 462, hep-ex/9907055.

[121] M. Acciarri et al. [L3 Collaboration], *$K_S^0 K_S^0$ final state in two-photon collisions and implications for glueballs*, Phys. Lett. B, 501 (2001) 173, hep-ex/0011037.

[122] http://www.scied.science.doe.gov/scied/JUR_v7/pdfs/Physics.pdf

[123] M. Gell-Mann and Y. Ne'eman, *The Eightfold Way* , New York: Benjamin, 1964.

[124] C. Amsler et al. [Particle Data Group Collaboration], *Quark Model*, Review of Particle Physics, Phys. Lett.B, 667, 2008.

[125] http://library.thinkquest.org/05aug/01087/quarks

[126] http://www.bnl.gov/rhic/RHIC2.asp

[127] www.kvi.nl/~loehner/saf_seminar/2008/TheQuarkAndBagModels.ppt

[128] http://hyperphysics.phy-astr.gsu.edu/hbase/particles/expar.html

[129] www.quantumdiaries.org/2010/10/03/world-of-glue/

[130] J.Beringer et al. (Particle Data Group), Phys. Rev. D88, 0100001 (2012) & 2013 partial update for the 2014 edition.

[131] http://physicsworld.com/cws/article/news/2010/apr/27/evidence-grows-for-tetraquarks

[132] F. E. Close, Rep. Prog. Phys. 51 833, 1988.

[133] F.Halzen and A. Martin, *Quarks and Leptons: An Introductory Course in Modern Particle Physics,* John Wiley and Sons, 1984.

[134] A. Daniel et al., *Procedures of CLAS12 PCAL module construction*, https://clasweb.jlab.org/wiki/images/6/64/PCAL_procedures.pdf

[135] G.Asryan, N.Dashyan, H.Voskanyan et.al, *Pre-shower calorimeter for the CLAS 12 detector*, https://userweb.jlab.org/~cshloka/master_pcal.pdf

[136] https://clasweb.jlab.org/wiki/index.php/CLAS12_Pre-shower_calorimeter

[137] A. Daniel, J. Riso, S. Stepanyan, W. Tang, H. Voskanyan, *Light transmission characteristics of scintillators for the pre-shower calorimeter*, CLAS-NOTE 2010-012.

[138] D.Keller et al., *Scintillator Testing for Use in the Pre-Shower Calorimeter*, CLAS NOTE 2009-018.

[139] Alexander Piaseczny, Jerod Sikorskyj and Michael Wood, *The Preshower Calorimeter in GEMC*, CLAS-NOTE 2010-014.

[140] G.P. Gilfoyle and K. Sherman, *Geometry Update for the Electromagnetic Calorimeter in CLAS12*, CLAS12 Note 2014-008.

[141] Natalia Dashyan and Stepan Stepanyan, *GEANT simulations of the CLAS12 pre–shower calorimeter*, CLAS-Note 2007-001.

[142] S.Stepanyan, *CLAS12 Pre-shower Calorimeter (PCAL) project*, https://userweb.jlab.org/~stepanya/clas12/preshower/PCAL_Summary.pdf

[143] Private correspondence with Adam Szczepaniak.

[144] J.J. Dudek, R.G. Edwards, P. Guo, C.E. Thomas, *Toward the excited isoscalar meson spectrum from lattice QCD*, Phys. Rev. D 88, 094505*,* 2013.

[145] R.C.Bower, S.D. Mathur, C. Tan, *Glueball Spectrum for QCD from AdS Supergravity Duality*, arXiv:hep-th/0003115v1.

[146] E. van Beveren, G. Rupp, *Scalar and axial-vector mesons,* Eur.Phys.J.A31:468-473*,*2007.

[147] B. Lucini, A. Rago, E. Rinaldi, *Towards the glueball spectrum from unquenched lattice QCD*, *J*HEP10 (2012) 170, arXiv:1208.1858v2 .

[148] K. Hashimoto, C. Tan, S. Terashima, *Glueball Decay in Holographic QCD*, Phys.Rev.D77:086001, 2008.

[149] C. J. Morningstar, M. Peardon, *Efficient glueball simulations on anisotropic lattices,* Phys.Rev.D56:4043-4061, 1997.

APPENDIX A: FITTING THE INVARIANT MASS SPECTRUM

A rough fit was performed on the K_SK_S invariant mass spectrum, with the cut $-t < 1$, using a sum of four gaussians and a third order polynomial. This fit gives the mass and width of the 1.5 GeV resonance as 1.504 GeV and 109.58 MeV respectively.

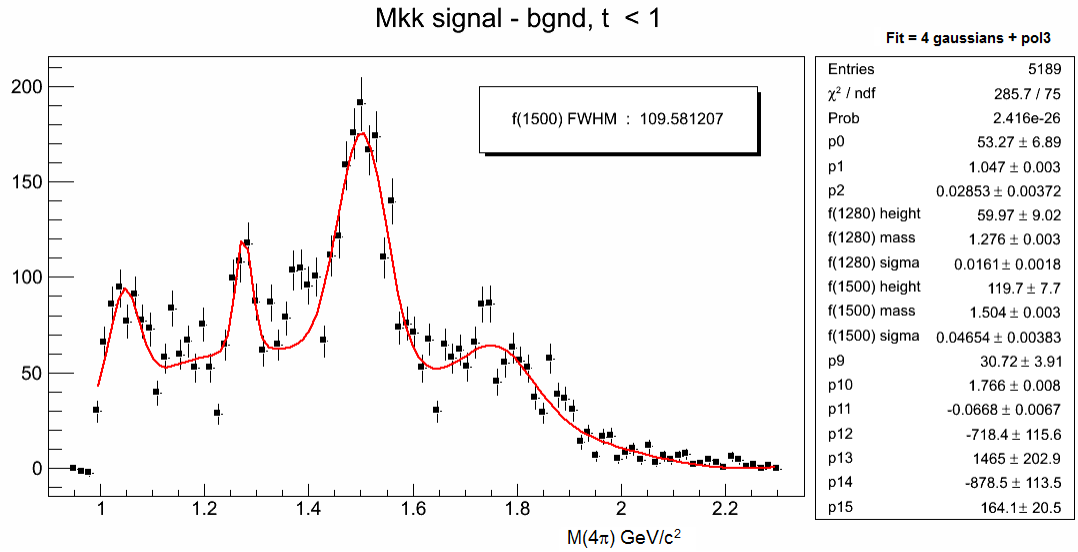

Figure A.1: The K_SK_S invariant mass spectrum fitted with the sum of 4 gaussians and a third order polynomial.

APPENDIX B: SYSTEMATIC STUDIES

B.1 Varying the Cut on the Signal

The standard cut applied on the signal in the thesis is a 3σ cut. Here, the size of this cut is varied, as seen in Fig. B.1, and its effect is seen in Fig. B.2. It is seen that increasing the size of the cut increased the size of the peaks in the lower energy range, however it did not cause much difference to the peak in the region of interest, thus reiterating our confidence in the background subtraction method.

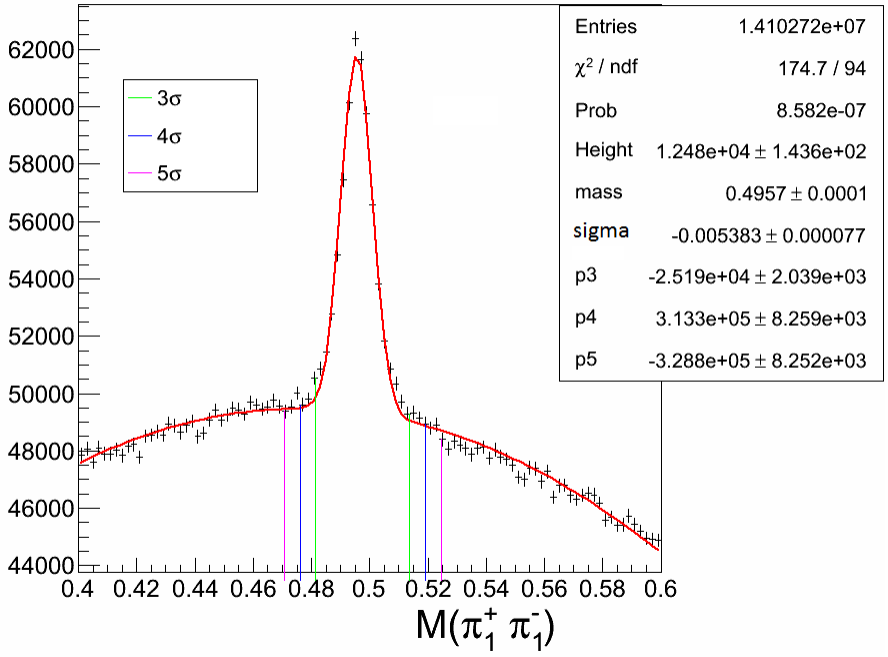

Figure B.1: Various cuts on the K_S signal.

B.2 Effect of DOCA cuts

The Distance of Closest Approach (DOCA) method is used to discriminate against uncorrelated pairs of particles. As shown in Fig. B.3, the red line connects the trajectories (depicted by black lines) of a pair of pions at the points where the pions would be closest to each other. The length of the red line is the DOCA. Smaller the DOCA, greater will

be the correlation between the two particles. Events with a large DOCA between a pair of expectedly correlated particles are discarded. This is a means of getting rid of background events.

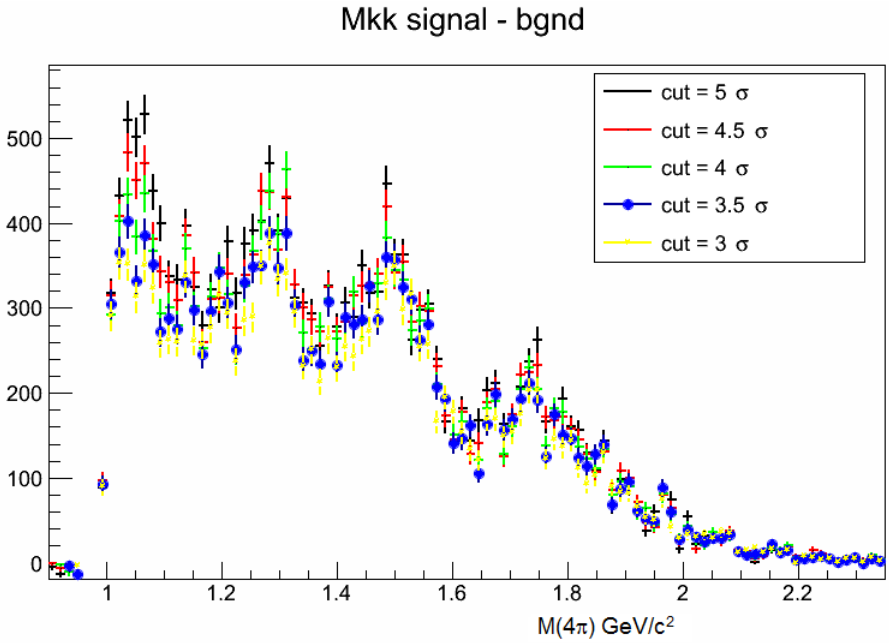

Figure B.2: Effect of varying the size of the cut on the K_S signal.

Fig. B.4 shows the plot of the DOCA between a pair of K_S. Cuts are made at different distances and their effect on the K_SK_S invariant mass spectrum is plotted in Fig. B.5. It is seen, both with cut on t, and with $-t < 1$, that the DOCA cut does not cause a significant increase in the signal to background ratio but it does result in a loss of statistics. Hence this cut is not used in the main analysis.

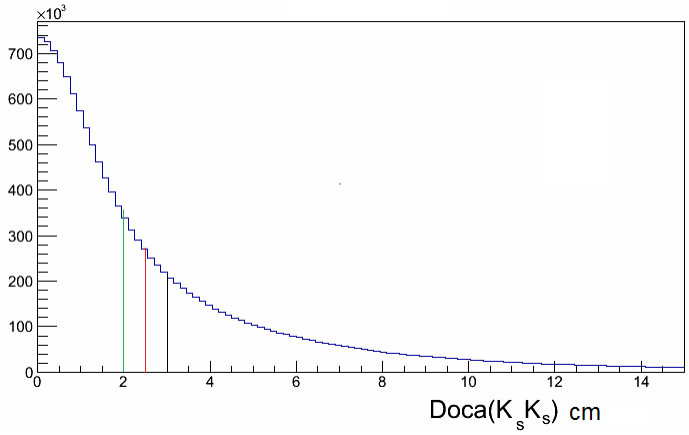

Figure B.4: The DOCA plot for a K_SK_S pair. The cuts to be tested are 2cm, 2.5 cm and 3 cm.

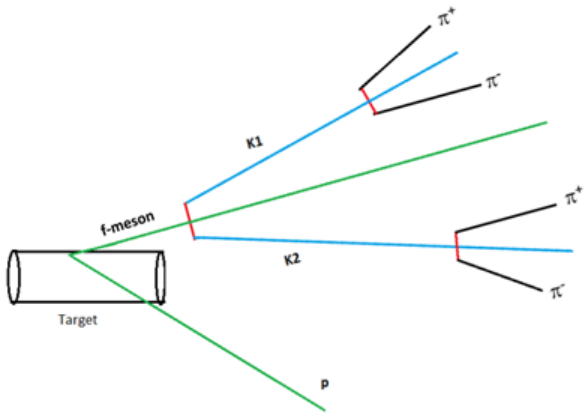

Figure B.3: Depiction of the distance of closest approach(DOCA). For a pair of particles, the red line joining their trajectories is the DOCA between them. Events in which a pair of particles which are expected to be correlated have a large DOCA can be discarded as a means of getting rid of unwanted events.

B.3 Effect of Cut on Photon Energy

Not limiting the photon energy to be greater than the threshold value of the production of the $f_0(1500)$ leads to the K_SK_S invariant mass spectrum being dominated by lower energy events, as shown in Fig. B.6.

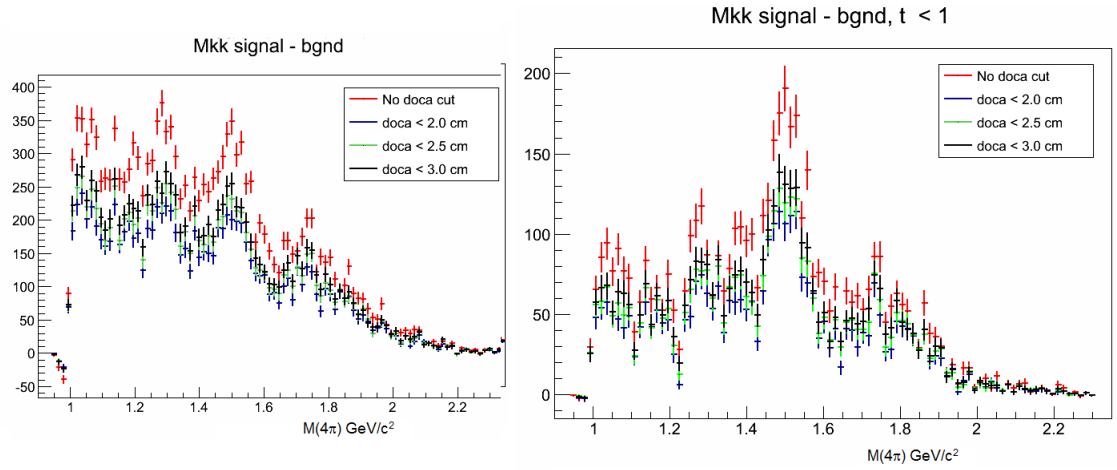

Figure B.5: Effect of DOCA cuts on the 4π invariant mass spectrum **Left:** Without any $t$cut. **Right:** With $-t < 1$ GeV^2.

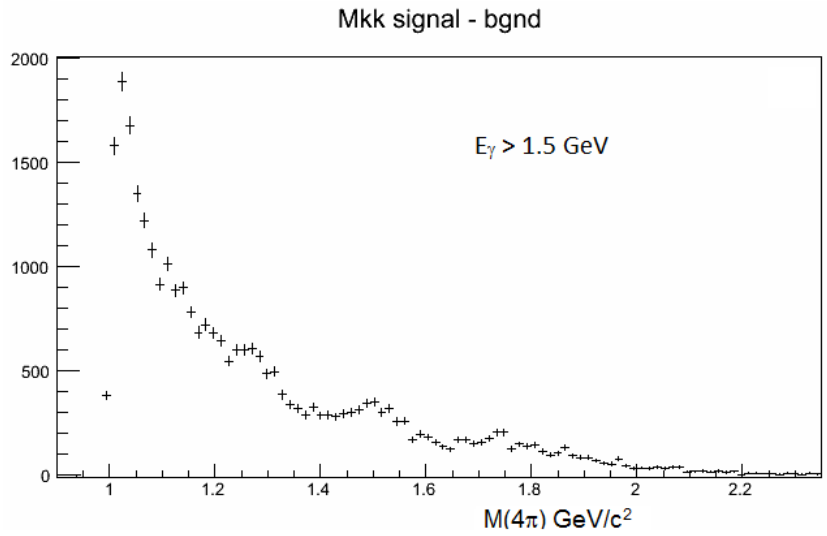

Figure B.6: K_SK_S invariant mass spectrum with all allowed photon energies above 1.5 GeV. This spectrum is dominated by lower energy events.

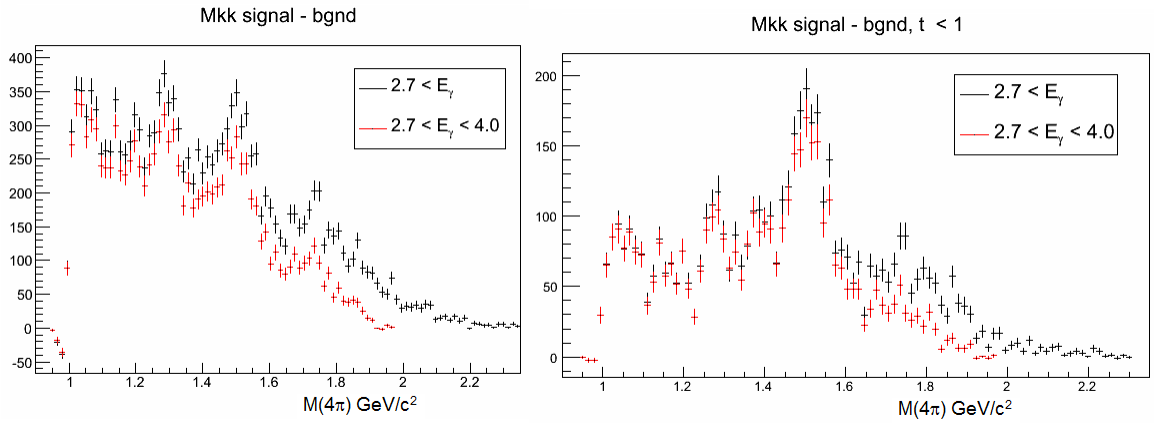

Figure B.7: Effect of cuts on photon energy on the K_SK_S invariant mass spectrum. The black histogram includes all photon energies above 2.7 GeV, whereas the red histogram has $2.7 < E_\gamma < 4.0$. **Left:** No cut on t **Right:** $t < 1$ GeV^2.

From Fig. 5.5 we see that the maximum events for the 1.5 GeV resonance fall within $E_\gamma \leq 4$ GeV , and indeed we see from Fig. B.7 that this is the case. This is made clear in the $t < 1$ GeV^2 plot which shows almost no difference in the histograms with the two energy cuts until ~1.6 GeV. However, we use all photon energies above 2.7 GeV in the main analysis so as to keep the shoulder at 1.7 GeV.

B.4 Alternate Method of Higher Level Event Selection

The method used in the main analysis was of sideband subtraction where all combinations of pion pairs were retained. Another method was looked into where the pion pairs were chosen depending upon which combination produced a K_S with the best match to the PDG value for its mass (see Fig. B.8). Kinematic fitting is done to get rid of the background and those events with a confidence level greater than 0.1% are chosen. Refer to Fig. B.9 for the confidence level and pulls from the fitting.

Fig. B.10 shows the 4π invariant mass spectrum using this method. However, this selection introduced the possibility of an imposed bias in the selection of the pion pairs and hence it was eventually abandoned.

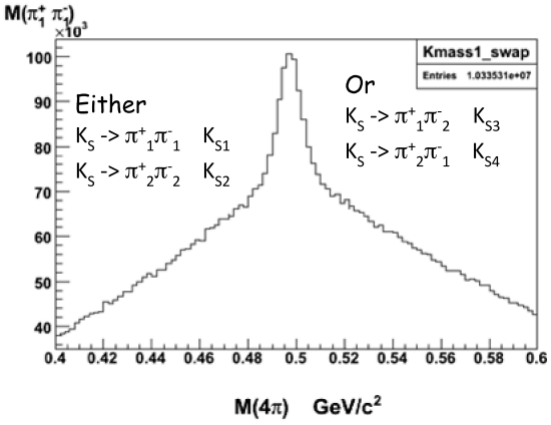

Figure B.8: The π_1^+ can either combine with π_1^- or π_2^-. That combination is chosen such that the mass of the kaon formed from the pair is a closer match to the PDG value than the other combination.

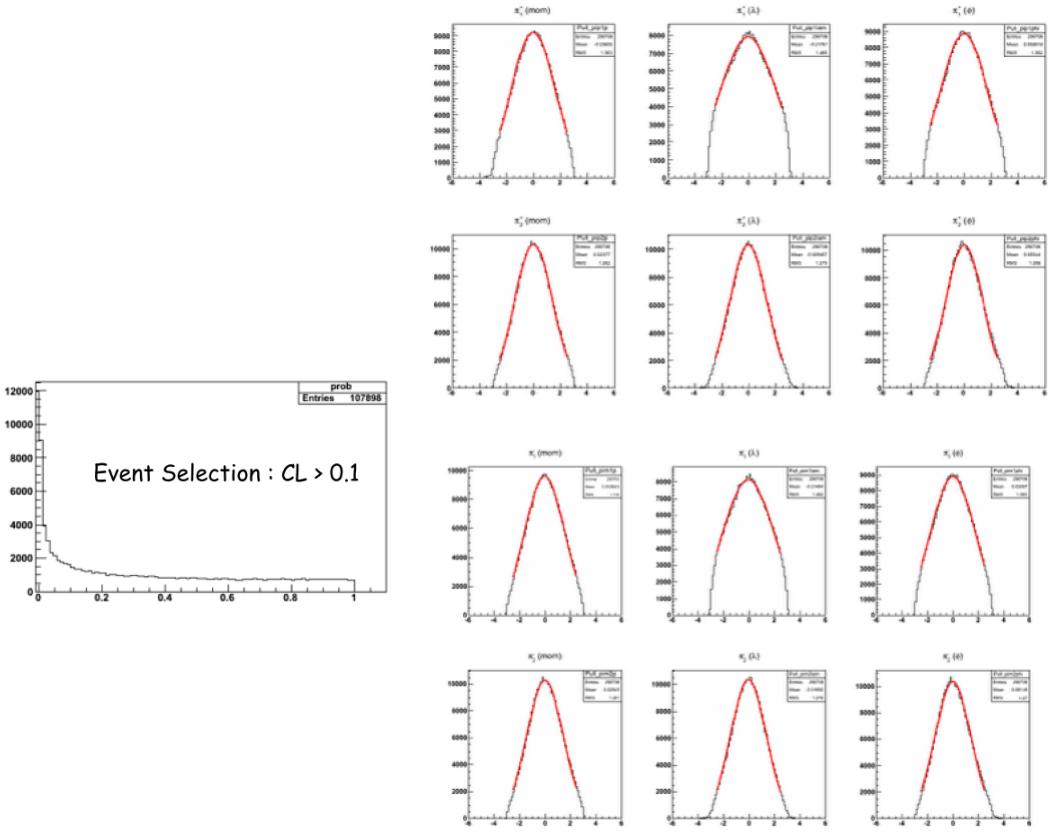

Figure B.9: Confidence Level (Left) and pulls (Right) from the kinematic fitting.

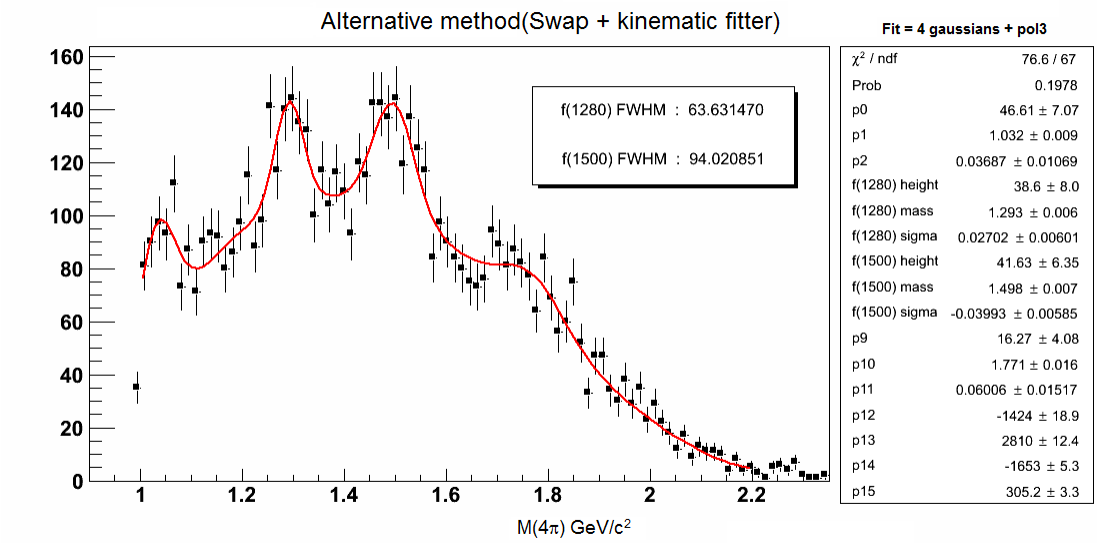

Figure B.10: $K_S K_S$ invariant mass spectrum using the alternate method of event selection

APPENDIX C: MOMENTS IN THE HELICITY FRAME OF THE RESONANCE

Moments analysis was also done in the helicity frame of the resonance X for the purposes of comparison between the two frames. These results are plotted in the Figs. C.1, C.2, C.3, and C.4.

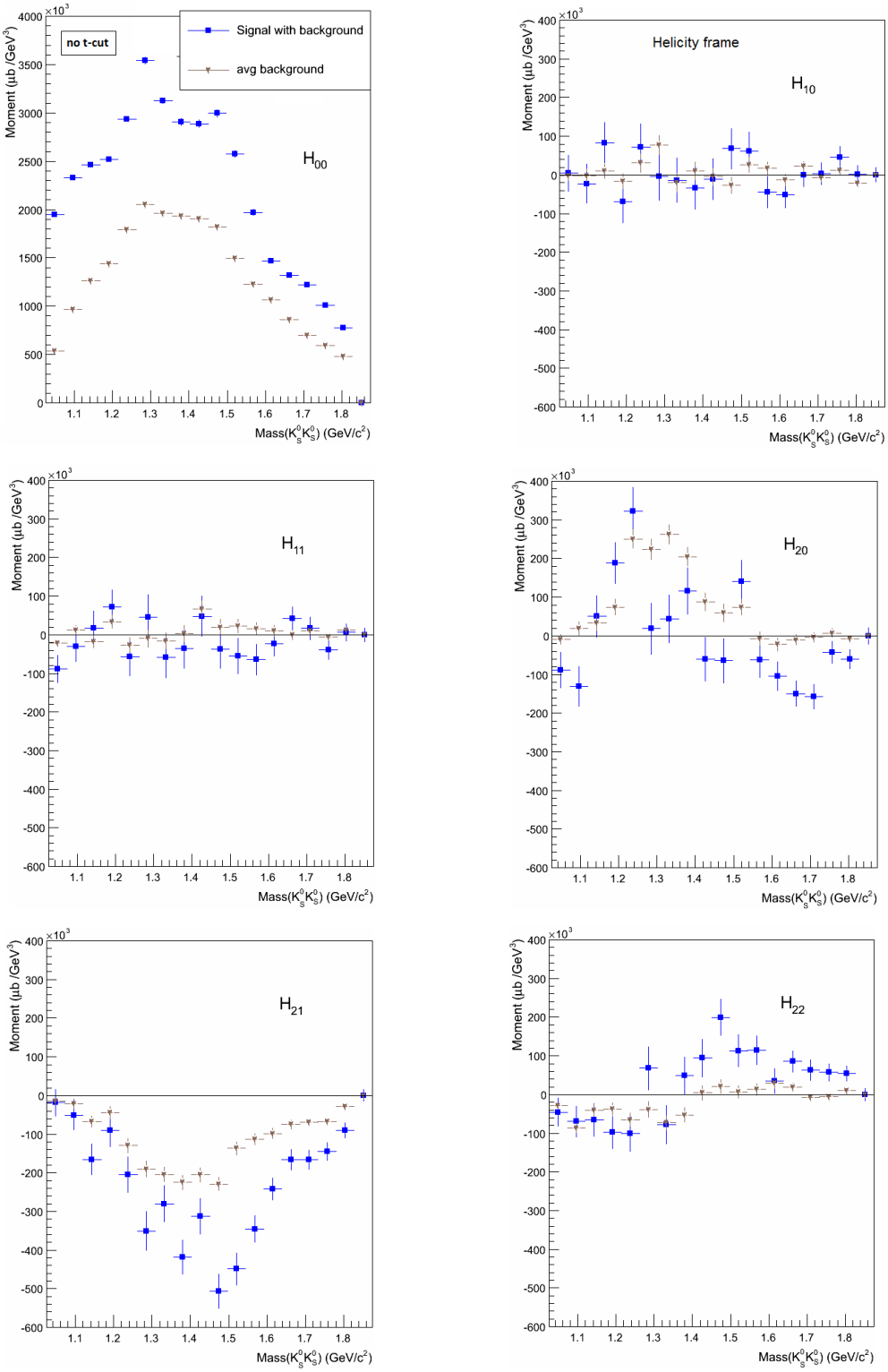

Figure C.1: Moments generated by fitting the intensity in the helicity frame, no cut on t. The blue squares represent the (signal+background) region, whereas the brown stars represent the average of the four sidebands.

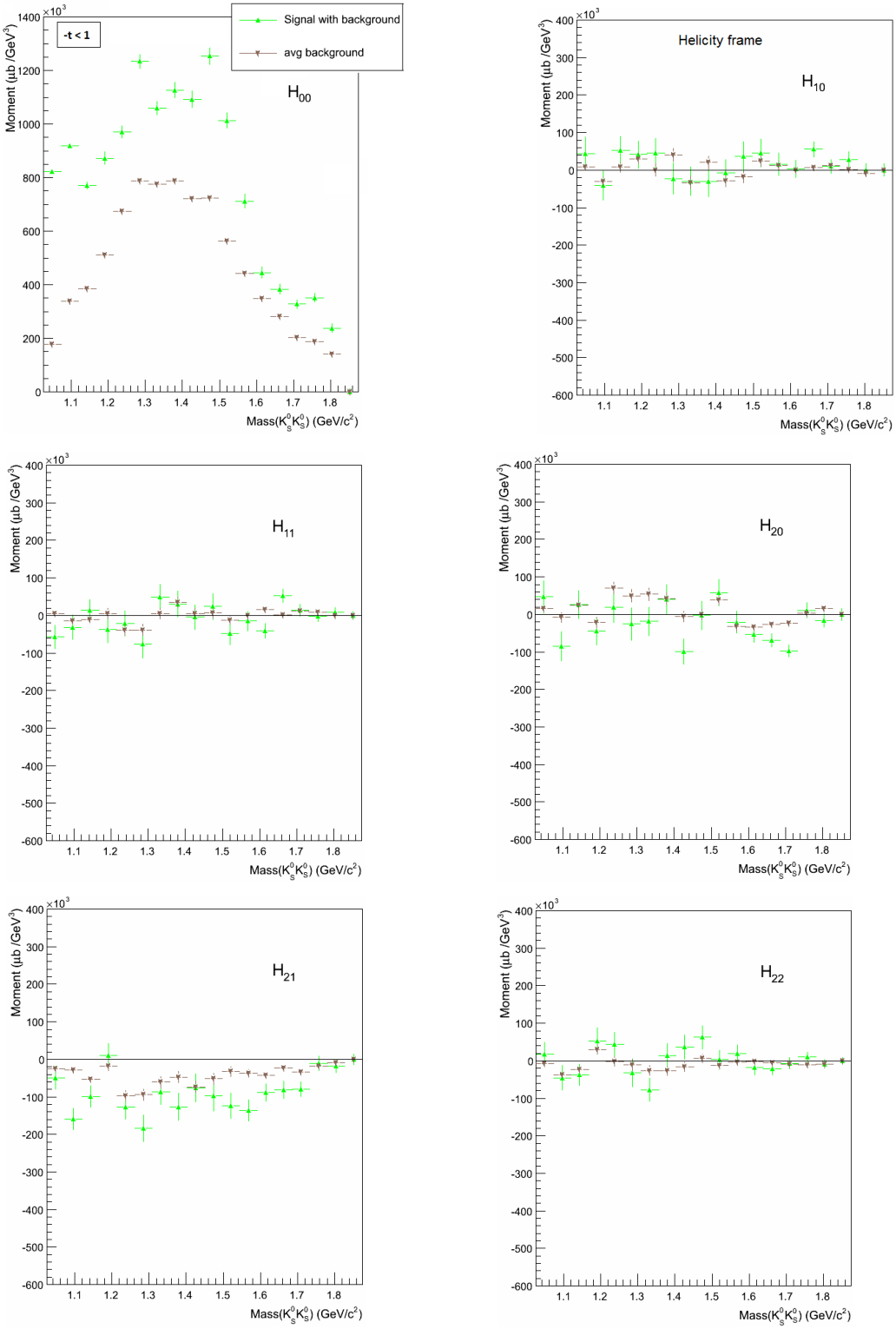

Figure C.2: Moments generated by fitting the intensity in the helicity frame, -t < 1 GeV^2. The green triangles represent the signal + background region, whereas the brown stars represent the average of the four sidebands.

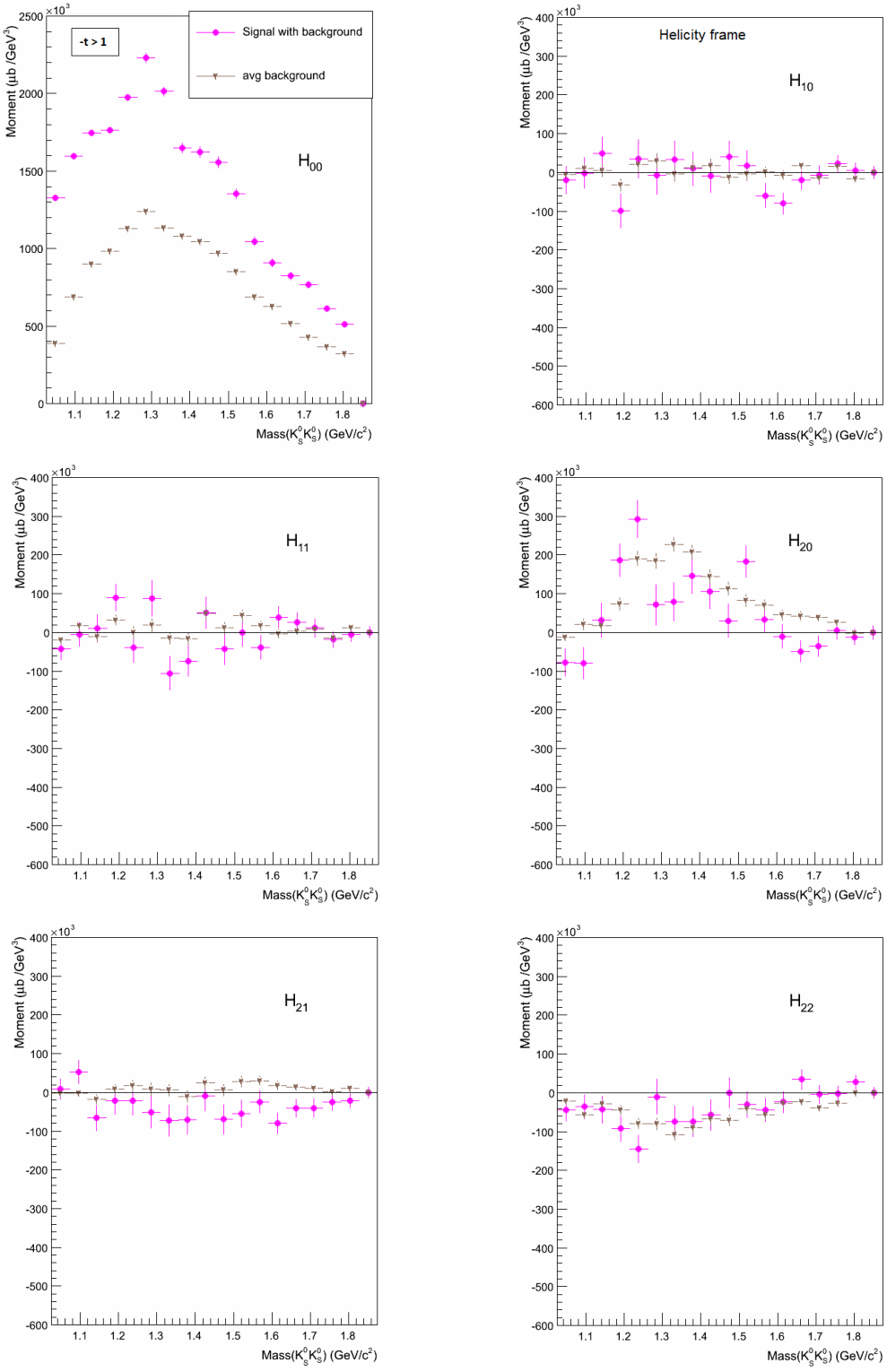

Figure C.3: Moments generated by fitting the intensity in the helicity frame, -t > 1 GeV^2. The magenta circles represent the signal + background region, whereas the brown stars represent the average of the four sidebands.

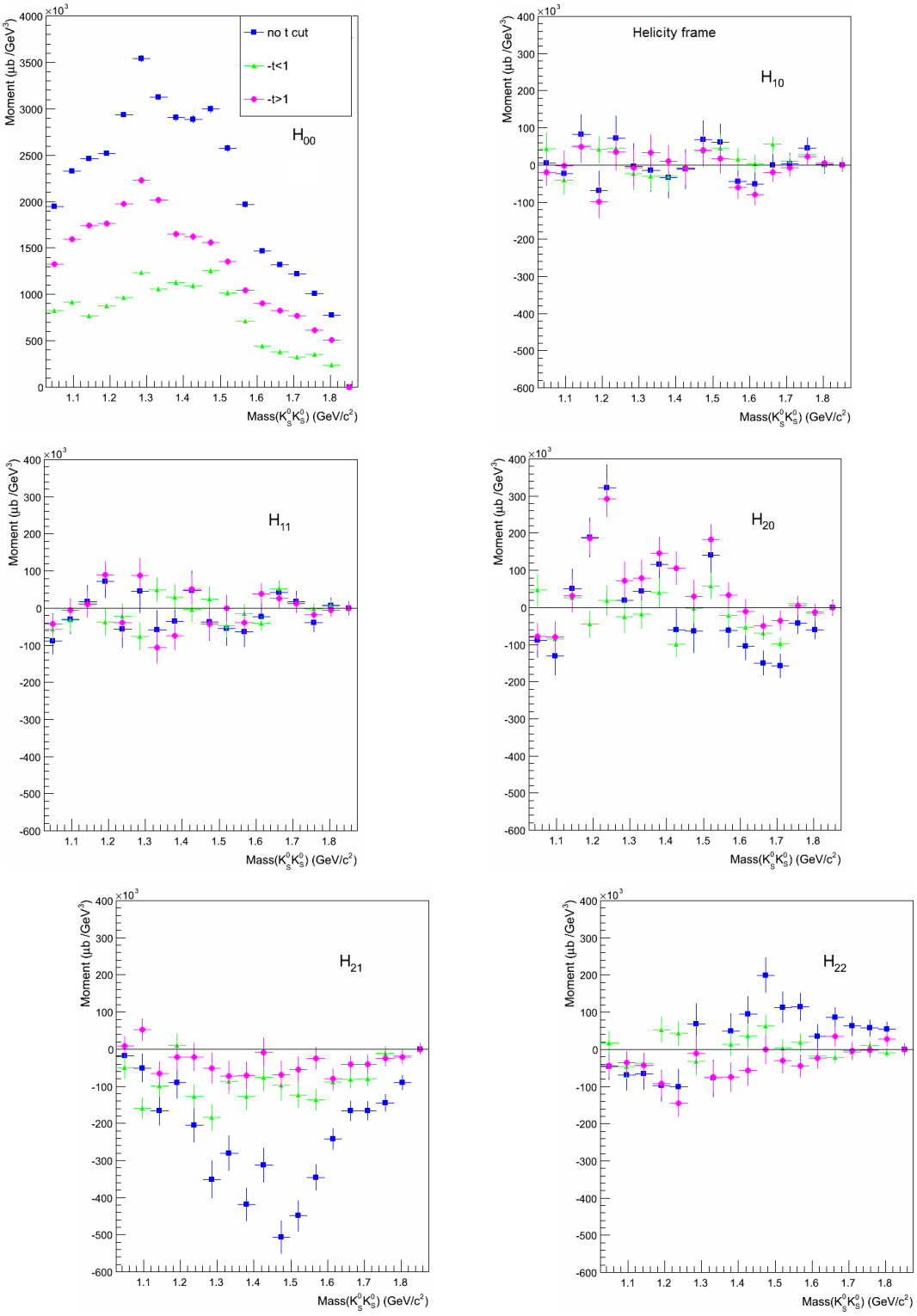

Figure C.4: Comparison between moments in the helicity frame with various cuts on t on the Signal+Background region.The blue squares signify no cut on t,the green triangles stand for $-t < 1$ GeV^2,the magenta circles denote $-t > 1$ GeV^2.

Thesis and Dissertation Services